Title
Nano-Scale Characterization of Biomolecules using Atomic Force Microscopy

Author
Woo, Jung reem

Publication Date
2015

Peer reviewed|Thesis/dissertation

UNIVERSITY OF CALIFORNIA

Los Angeles

Nano-Scale Characterization of Biomolecules using Atomic Force Microscopy

A dissertation submitted in partial satisfaction of the requirements for the degree Doctor of Philosophy in Biochemistry & Molecular Biology

by

Jung Reem Woo

2015

`

ABSTRACT OF THE DISSERTATION

Nano-Scale Characterization of Biomolecules using Atomic Force Microscopy

by

Jung Reem Woo

Doctor of Philosophy in Biochemistry & Molecular Biology

University of California, Los Angeles, 2015

Professor James K. Gimzewski, Chair

Atomic force microscopy (AFM) is a class of high-resolution scanning probe microscopy (SPM) for non-conducting materials. Of these non-conducting materials, biomolecules such as cells, organelles, proteins, and nucleic acids are of interest as we seek to describe laws of nature and life. However, it is not trivial to resolve structures or mechanics of biomolecules due to their small sizes and soft constructions. AFM enables one to obtain high-resolution images of biological structures in their native state both in air and in fluids as AFM is considered as a non-destructive technique. In addition to these advantages, AFM is providing the mechanical information of the sample surface. For these reasons, since the development of AFM, an expansion and re-assessment has led to significant discoveries and scientific enlightenmentin biology. In this dissertation, I focus on the application of AFM to biological systems, which will add new scores in the field of both microscopy as well as a higher understanding of specific biological systems. I have explored the mechanical properties of mammalian cells and bacterial cells. I have examined mammalian cell stiffness in relation to cancer metastasis and the changes

in extracellular biofilm adhesions from bacterial cells. I have resolved the high-resolution structure of exosomes which are 50-120 nm sized vesicles secreted from mammalian cells. With an accurate adjustment of the force applied to the sample, I have been able to observe and verify nanofilaments attached to exosomes. I also have discovered that the surface and the size distributions of exosomes are different depending on their purification methods. Lastly, I have obtained high-resolution images of an actin binding protein, INF2, which showed nanostructured self-assemblies with or without f-actin.

The dissertation of Jung Reem Woo is approved.

Steven G. Clarke

Jian Yu Rao

James K. Gimzewski, Committee Chair

University of California, Los Angeles

2015

Dedicated to my loving family in Korea

Table of Contents

List of Tables

List of Figures

Acknowledgements

Chapter 3 is a version of Alia Ghoneum, Huanqi Zhu, **JungReem Woo**, Nikita Zabinyakov, Shivani Sharma, and James K. Gimzewski, 2014, "Biophysical and Morphological Effects of Nanodiamond/Nanoplatinum Solution (DPV576) on Metastatic Murine Breast Cancer Cells in Vitro", Nanotechnology 25, 46510. The published manuscript carries the following acknowledgement: Authors would like to acknowledge support from International Center for Materials Nanoarchitectonics Satellite (MANA), National Institute for Materials Science (NIMS), Tsukuba, Japan. We acknowledge the use of the Scanning Probe Microscope facility at the Nano and Pico Characterization Laboratory at the CNSI. SEM image courtesy Venex Co., Ltd. Kanagawa, Japan.

Chapter 5 is a version of Shivani Sharma, Stacey Lavender, **JungReem Woo**, LihongGuo, Wenyuan Shi, LaTonya Kilpatrick-Liverman, and James K. Gimzewski, 2014, "Nanoscale Characterization of Effect of L-arginine on S. Mutans Biofilm Adhesion by Atomic Force Microscopy", Microbiology 160 (Pt 7), 1466-73. The published manuscript carries the following acknowledgement: Authors would like to acknowledge financial support from Colgate-Palmolive Company, Piscataway, NJ and International Center for Materials Nanoarchitectonics Satellite (MANA), National Institute for Materials Science (NIMS), Tsukuba, Japan. We acknowledge the use of the Scanning Probe Microscope facility at the Nano and Pico Characterization Laboratory at the CNSI at UCLA.

Chapter 6 is a version of Shivani Sharma, Kingshuk Das, **JungReem Woo**, James K.

Gimzewski, 2014, “Nanofilaments on Glioblastoma Exosomes Revealed by Peak Force Microscopy”, Journal of the Royal Society Interface 11 (92), 20131150. The published manuscript carries the following acknowledgement: Support from MEXT WPI Program: International Center for Materials Nanoarchitectonics (MANA), Japan and CNSI is acknowledged. We acknowledge the use of AFMs at the Nano and Pico Characterization Laboratory at CNSI.

Chapter 8 is a version of Shivani Sharma, Elena E. Grintsevich, **JungReem Woo**, Pinar S. Gurel, Henry N. Higgs, Emil Reisler, and James K. Gimzewski, 2014, “Nanostructured Self-Assembly of Inverted Formin 2 (INF2) and F-Actin–INF2 Complexes Revealed by Atomic Force Microscopy”, Langmuir 30 (25), 7533-7539. The published manuscript carries the following acknowledgement: Support for this work from MEXT WPI Program: International Center for Materials Nanoarchitectonics (MANA), Japan is acknowledged. PSG and HNH were supported by NIH R01 GM069818, and EG and ER were supported by NIH R01 GM077190. We acknowledge the use of the NPC core facility supported by CNSI at UCLA.

Vita

2003-2008	B.S. in Chemistry
	B.S. in Mathematics
	Seoul National University
	Seoul, South Korea
2003-2007	National Science and Technology Scholarship for Undergraduate Students
	Ministry of Education and Human Resources Development
	Seoul, South Korea
2008	Best Senior Paper Award
	Department of Chemistry, Seoul National University
	Seoul, South Korea
2008-2010	M.S. in Chemistry
	Seoul National University
	Seoul, South Korea
2010-2012	Korean Government Scholarship Program for Study Overseas
	Seoul, South Korea
2013	Samson Cheng Biochemistry Teaching Award
	Department of Chemistry and Biochemistry
	University of California, Los Angeles
	Los Angeles, CA

Publications: Peer-reviewed Journals

- Alia Ghoneum, Huanqi Zhu, **JungReem Woo**, Nikita Zabinyakov, Shivani Sharma, and James K.Gimzewski, **2014**, "Biophysical and Morphological Effects of Nanodiamond/Nanoplatinum Solution (DPV576) on Metastatic Murine Breast Cancer Cells *in Vitro*", *Nanotechnology* **25** 46510.
- Shivani Sharma, Elena E. Grintsevich, **JungReem Woo**, Pinar S. Gurel, Henry N. Higgs, Emil Reisler, and James K. Gimzewski, **2014**, "Nanostructured Self-Assembly of Inverted Formin 2 (INF2) and F-Actin–INF2 Complexes Revealed by Atomic Force Microscopy", *Langmuir* **30** (25), 7533-7539.

- Shivani Sharma, Stacey Lavender, **JungReem Woo**, LihongGuo, Wenyuan Shi, LaTonya Kilpatrick-Liverman, and James K. Gimzewski, **2014**, "Nanoscale Characterization of Effect of L-arginine on *S. Mutans* Biofilm Adhesion by Atomic Force Microscopy", *Microbiology***160** (Pt 7), 1466-73.
- Shivani Sharma, Kingshuk Das, **JungReem Woo**, and James K. Gimzewski, **2014**, "Nanofilaments on Glioblastoma Exosomes Revealed by Peak Force Microscopy", *Journal of the Royal Society Interface* **11** (92), 20131150.
- **Jung-Reem Woo**, Dong-Kwon Lim, and Jwa-Min Nam, **2011**, "Minimally Stable Nanoparticle-Based Colorimetric Assay for Simple, Rapid, and Sensitive Antibody Structure and Activity Evaluation", *Small* **7**, 648-55.
- So-Youn Shim, **Jung-Reem Woo**, Eun-Ju Nam, Hyun-Joo Hong, InheeMook-Jung, Young-Ho Kim, and Jwa-Min Nam, **2008**, "Stepwise Silver-Staining-Based Immunosorbent Assay for Amyloid-β Autoantibody Detection", *Nanomedicine***3**, 485-493.

Selected Presentations

- "Exploring the Structure of Exosomes with Nanofilaments using Atomic Force Microscopy", Dec **2014**, *6th AFM BioMED Conference San Diego 2014,* La Jolla, CA **(poster presentation)**.
- "Atomic Force Microscopy Reveals Nanofilament Structures of Exosomes", Feb **2014**, *Southern California Society for Microscopy & Microanalysis 2014 Full-Day Symposium,* Irvine, CA **(oral presentation)**.
- "Nanofilaments Found on Exosomes by Atomic Force Microscopy", Feb **2014**, *2014 David S. Sigman Memorial Symposium,* Los Angeles, CA **(poster presentation)**.
- "Does Cancer Start with Protein Aggregation? The Aggregated Structure of a p53 Segment", Oct **2011**, *2011 MBI Lake Arrowhead Retreat,* Lake Arrowhead, CA **(poster presentation)**.
- "Nanoparticle Aggregation Assay for Rapid and Accurate Protein Structure Analysis", Nov **2009**, *the 12th Seoul National University and Hokkaido University Joint Symposium on Nano Green Chemistry for Sustainable Society,* Seoul, South Korea **(poster presentation)**.
- "Alzheimer's Disease (AD) Biomarker-Based High-Throughput AD Diagnostic System using Multifunctional Gold Nanoparticle Probes", Mar **2008**, *Materials Research Society Spring Meeting,* San Francisco, CA **(poster presentation)**.

Chapter 1.

Introduction

1.1 Atomic Force Microscopy (AFM)

It has been almost three decades since the development of atomic force microscope (AFM) by Binnig and colleagues in 1986 [1]. AFM has played a key role in deciphering the structure and mechanical properties of various biological specimen.AFM is capable of resolving the structure of a sample in sub-nanometer resolution both in air and fluid medium while while being a non-descructive method. Along with high-resolution structure information, AFM is also providing local mechanical information of the sample and the sample does not need to be labeled, fixed, or stained to be imaged. Each individually resolved objects of the sample are building up un-averaged single molecule data. Thus since the development of AFM, it led to significant findings in many fields and the applications of AFM are expanding in new areas of science including biology. In this dissertation, I focus on the application of AFM to biological systems. The topographical, structural, and mechanical properties of biomolecules are explored through close collaboration with Department of Chemistry and Biochemistry, Medical Schools, and Dental Schools at UCLA.

1.2 The needs for Nano-Scale Characterization of Biomolecules

Observations have been the most important yet basic step of science. From limited human eye resolutions to atomic resolutions, there have been the fundamental needs for ‘better’ microscopes and many advances have beenachieved in microscopy. Specifically in biology, research has been focused on dissembling life to organs, tissues, cells, organelles, proteins and nucleic acids, then to atoms. This effort would discover how biological systems are composed and how biological component plays an integral part in function. With advances in microscopy, we have characterized micro-scale biomolecules including tissues and cells, and now we are at a stage where we seek to resolve nano-scale biomolecules, i.e., organelles, protein, and nucleic acids. Using optical microscopy, we can obtain high-resolution fluorescent images of subcellular structures, which the protein of interest is labeled with appropriate fluorescent dyes or green fluorescent proteins [2]. We are still limited to the Abbe diffraction limit that gives us 200 nm in spatial resolution and with the development of super-resolution microscopy now we can bypass the limit [3]. However, it usually requires the proper fixation of fluorescent dyes to the sample resulting in the loss of dynamic information. The other widely used microscopy for nano-scale imaging is electron microscope (EM), and it allows us to resolve the sample up to 50 pm performing true atomic resolutions [4]. However, it is also mandatory to stain and fix the sample that may affect the native state of the sample and have vacuumed imaging condition. Thus for achieving nano-scale imaging in the native state of a biological sample, AFM could be a viable candidate. The imaging condition of AFM can be both in air and fluid so the sample can be imaged as a native state without any staining or fixing [5]. Since the beginning of AFM, a lot of biomolecules including DNA were imaged [6-7] and as the resolution of AFM also improved the resolution of double helix of DNA was observed under fluid AFM [8]. Also, as the AFM tip is

physically interacting with the sample surface, it gives information on stiffness and adhesion the sample's surface in which other microscopes are not capable [9]. With these advantages, Gimzeswki group has conducted wide range characterization of biomolecules; from mammalian cancer cells to bacterial cells and subcellular structures including exosomes, proteins, and nucleic acids. In this dissertation, I will first discuss the basics of AFM briefly (Chapter 2), mechanical properties of cancer cells (Chapter 3 and 4), the structure and adhesive behavior of biofilms generated by bacterial cells (Chapter 5), the high resolution structure of isolated exosomes (Chapter 6 and 7), and the self-assembled structure of inverted formin 2 (INF2), an actin-binding protein (Chapter 8).

1.3 References

1. Binnig, G., C.F. Quate, and C. Gerber, *Atomic force microscope.* Phys Rev Lett, 1986. **56**(9): p. 930-933.
2. Lichtman, J.W. and J.A. Conchello, *Fluorescence microscopy.* Nat Methods, 2005. **2**(12): p. 910-9.
3. Leung, B.O. and K.C. Chou, *Review of super-resolution fluorescence microscopy for biology.* Appl Spectrosc, 2011. **65**(9): p. 967-80.
4. Kourkoutis, L.F., J.M. Plitzko, and W. Baumeister, *Electron Microscopy of Biological Materials at the Nanometer Scale.* Annual Review of Materials Research, Vol 42, 2012. **42**: p. 33-58.
5. Vahabi, S., B. Nazemi Salman, and A. Javanmard, *Atomic force microscopy application in biological research: a review study.* Iran J Med Sci, 2013. **38**(2): p. 76-83.
6. Bustamante, C., et al., *Circular DNA molecules imaged in air by scanning force microscopy.* Biochemistry, 1992. **31**(1): p. 22-6.
7. Hansma, H.G., et al., *Reproducible Imaging and Dissection of Plasmid DNA under Liquid with the Atomic Force Microscope.* Science, 1992. **256**(5060): p. 1180-1184.
8. Leung, C., et al., *Atomic force microscopy with nanoscale cantilevers resolves different structural conformations of the DNA double helix.* Nano Lett, 2012. **12**(7): p. 3846-50.
9. Carvalho, F.A. and N.C. Santos, *Atomic force microscopy-based force spectroscopy--biological and biomedical applications.* IUBMB Life, 2012. **64**(6): p. 465-72.

Chapter 2.

Background

2.1 AFM Imaging with Tapping Mode

The conventional AFM was operated in a contact mode. In the contact mode, the tip is located near the sample surface where the main working interatomic force is a repulsive force [1]. However, it is not useful for soft biological materials as the shear friction force originating from the lateral scanning is damaging to the surface [2]. A main advance in AFM is a development of tapping mode [3]. In this mode, the cantilever is oscillated near its natural resonant frequency by a piezoelectric actuator. The cantilever is ‘tapping’ during the scanning, and the tip-end is touching the surface lightly and lifting off immediately which reduces friction forces in a contact mode [1]. Thus, with tapping mode, we can image soft biological samples with minimal damage to the surface. I was able to obtain high-resolution images of an actin-binding protein, inverted formin 2 (INF2) with and without actin filaments using the tapping mode thatis described in detail in Chapter 7.

2.2 AFM Force Spectroscopy

It is one of the advantages of AFM that the tip is physically interacting with the surface. It depends on the operating mode on how the tip is interacting with the surface, but we can obtain the mechanical information of the surface during the 'touching'. AFM is utilized as a nano-indenter as we can observe how the tip is interacting with the surface while applying known nano-newton scale forces on the surface [4-5]. Thus, we can obtain the mechanical properties including stiffness and adhesion. Previously, Gimzewski group had studied cell stiffness as a marker for cancer, and here in this dissertation I have expanded the scope of this study; i) how the cancer cell stiffness is changing under the known cancer drug treatment (Chapter 3) and ii) how the mechanical properties of cells are changing by trypsin treatment (Chapter 4). Also, I have explored the adhesive characteristic of biofilm generated by *S. mutans* (Chapter 5).

2.3 AFM Imaging with Peak Force Mode

Peak Force Mode is a recently developed mode of AFM, which combines the tapping mode and force spectroscopy [6]. Instead of its natural resonant frequency, the cantilever is oscillating at a much lower frequency, typically 1 or 2 kHz. Each tapping is executed with a controlled force spectroscopy thus in each pixel we can obtain the topographical and mechanical information simultaneously. The ramping is driven by a sinusoidal curve that makes the tip velocity be near zero when the tip is approaching the sample surface. Also, we can accurately control the force that is applied to the tip, which allows us to further minimize the sample damage compared to tapping mode. With these benefits of peak force mode, we were able to characterize exosome nanofilaments (Chapter 6).

2.4 References

1. Kasas, S., et al., *Biological applications of the AFM: From single molecules to organs.* International Journal of Imaging Systems and Technology, 1997. **8**(2): p. 151-161.
2. Moreno-Herrero, F., et al., *Atomic force microscopy contact, tapping, and jumping modes for imaging biological samples in liquids.* Physical Review E, 2004. **69**(3).
3. Zhong, Q., et al., *Fractured Polymer Silica Fiber Surface Studied by Tapping Mode Atomic-Force Microscopy.* Surface Science, 1993. **290**(1-2): p. L688-L692.
4. Carvalho, F.A. and N.C. Santos, *Atomic force microscopy-based force spectroscopy--biological and biomedical applications.* IUBMB Life, 2012. **64**(6): p. 465-72.
5. Clausen-Schaumann, H., et al., *Force spectroscopy with single bio-molecules.* Current Opinion in Chemical Biology, 2000. **4**(5): p. 524-530.
6. Foster, B., *New Atomic Force Microscopy (AFM) Approaches Life Sciences Gently, Quantitatively, and Correlatively.* American Laboratory, 2012. **44**(4): p. 24-+.

Chapter 3.

Biophysical and Morphological Effects of Nanodiamond/Nanoplatinum Solution (DPV576) on Metastatic Murine Breast Cancer Cells *in Vitro*

3.1 Abstract

Nanoparticles have recently gained increased attention as drug delivery systems for the treatment of cancer due to their minute size and unique chemical properties. However, very few studies have tested the biophysical changes associated with nanoparticles on metastatic cancer cells at the cellular and sub-cellular scales. Here, we investigated the mechanical and morphological properties of cancer cells by measuring the changes in cell Young's Modulus using AFM, filopodial retraction (FR) by time lapse optical light microscopy imaging and filopodial disorganization by high resolution AFM imaging of cells upon treatment with nanoparticles. In the current study, nanomechanical changes in live murine metastatic breast cancer cells (4T1) post exposure to a nanodiamond/nanoplatinum mixture dispersed in aqueous solution (DPV576), were monitored. Results showed a decrease in Young's modulus at two hours post treatment with DPV576 in a dose dependent manner. Partial FR at 20 minutes and complete FR at 40 minutes were observed. Moreover, analysis of retraction distance (in microns) measured over time (minutes), showed that a DPV576 concentration of 15%v/v yielded the highest FR rate. In addition, DPV576 treated cells showed early signs of filopodial disorganization and disintegration. This study demonstrates the changes in cell stiffness and tracks early structural alterations of metastatic breast cancer cells post treatment with DPV576, which may have important implications in the role of nanodiamond/nanoplatinum based cancer cell therapy and sensitization to chemotherapy drugs.

3.2 Introduction

Several studies suggest that nanodiamonds (NDs) have several unique biomedical applications which are attributed to their characteristic features such as their large specific surface areas, stable photoluminescence, and ability to be functionalized with biomolecules [1, 2]. These qualities have made them useful agents in various medical applications such as biosensing, imaging probes [3], protein mimics [4], tissue scaffolds and surgical implants [5, 6]. In particular, due to their biocompatibility, capability to transport a wide range of therapies, dispersible qualities in water and scalability, they have gained increased attention as drug delivery systems for the treatment of cancer [7].

NDs hold several properties that make them attractive candidates for the treatment of cancer, including their low cytotoxicity. Studies by Schrand *et al.* reported that NDs are non-toxic in various different cell types and did not cause significant reactive oxygen species [8]. Moreover, NDs instilled intratracheally showed no significant adverse effects in the lungs of mice [9]. Although much work has been done with NDs, biophysical analysis and morphological changes at the single cell level, which are important in understanding the dynamics of metastasis, are lacking. Young's modulus, a quantitative indicator of material stiffness has been recognized as a phenotypic characteristic associated with cancer cells [10-12]. In addition, it is understood that metastasis also causes significant changes in the biological, structural and physical characteristics of cells [13]. Actin rearrangement within the cytoskeletal organization is common to cancer cells [12]. Understanding the role that the cytoskeletal network plays in metastasis requires a thorough analysis of actin dynamics [14]. The process of actin polymerization is integral in the metastatic steps of intravasation, migration, and extravasation [15]. Of particular

interest are filopodial, finger-like projections on the motile side of the cell comprised of an actin network. In order to understand the mechanical aspects of the ND- mediated changes in cancer cells at the single cell level, we studied the dose dependent effect of DPV576 on the stiffness and morphology of live murine metastatic breast cancer cells [16-19].

3.3 Materials and Methods

Chemicals: RPMI 1640, FBS, L-Glutamine, Penicillin G, Streptomycin Sulfate, Dulbecco's PBS, and trypsin-EDTA were purchased from Gemini-Bio Products, CA, USA. A mixture of ND and NP solution known as DPV576 was used with particle size, shape, and composition as previously described [20]. DPV576 was supplied by Venex Co, Ltd, Kanagawa, Japan.

SEM/AFM imaging of DPV576: DPV576 particle aqueous solution imaged by SEM at 100,000x magnification shows aggregation (Fig.1). AFM images of aqueous solution of DPV576 were obtained over mica substrates using Dimension Icon (Bruker, CA, USA) under tapping mode in air using TESPW tips (Bruker, CA, USA).

Murine Breast Cancer Cell Line: 4T1 cells, purchased from the American Tissue Culture Collection (ATCC) Manassas, VA, USA, were cultured in RPMI 1640 supplemented with 10% heat inactivated FBS, 2mmol L-Glutamine, 100units/mL Penicillin G, and 100 µg/mL Streptomycin Sulfate. Cells were incubated at 37°C and 5% carbon dioxide. At approximately 80% confluency, cells were washed with PBS and passaged using 0.25% trypsin-EDTA treatment for dissociation.

DPV576 Treatment: 4T1 cells were cultured in two flasks and divided into a total of eight petri dishes. Cells were exposed to 0, 5, 10, and 15% ND/NP solution (in duplicate) and were allowed to incubate for two hours. Subsequently, petri dishes were removed from incubator and used for AFM measurements.

AFM Measurements: All measurements were conducted on live cells under culture media using a Catalyst atomic force microscope (Bruker Instruments, CA, USA) with a combined inverted optical/confocal microscope (Zeiss, Corp, NY, USA). This combination permits lateral positioning of the AFM tip over the cell center with submicron precision. AFM mechanical measurements were collected in contact mode using sharpened silicon nitride cantilevers with experimentally determined spring constants of 0.02 N/m using thermal noise calibration method [21] and a tip radius of <20 nm. Mechanical measurements were obtained at 37°C with force measurements recorded at a pulling rate of 1Hz. AFM measurements were obtained in at least 30 cells live, unfixed cells for both treated and untreated samples with a maximum applied force of 1nN. The AFM tip was always precisely positioned (within micron range) on top of the cell nuclear regions using motorized stage and 200X inverted optical view of the combined confocal-AFM microscope [22].

AFM Imaging of Cellular Extensions: 4T1 cells were incubated with 15% DPV576 for one hour after which cells were fixed with 2% paraformaldehyde in PBS and imaged in PBS using Silicon-nitride probes with spring constants of 0.02 N/m.

Time Lapse Optical Light Microscopy: Images were acquired using a Catalyst atomic force microscope (Bruker Instruments, CA, USA) with a combined inverted optical/confocal microscope (Zeiss, Corp, NY, USA). A 4T1 cell suspension was dispensed into petri dishes and incubated overnight to allow for cell adherence. After washing with RPMI-1640 complete media, suspended ND/NP were added at 5%, 10%, and 15% (v/v) concentrations in duplicate. Following 2 hours of incubation, the cells were observed and recorded at 20X magnification.

Statistical Analysis: Statistical significance for cell stiffness in Figures 1 and 2 was determined by using Student's t-test. Differences were considered significant at the $p<0.05$ level.

3.4 Results

DPV576 Particle Size Determination: SEM image shows nanoparticle aggregates up to 200 nm and AFM image shows a size range from 20-40 nm for ND/NP isolated particles (Figure 1 A, B).

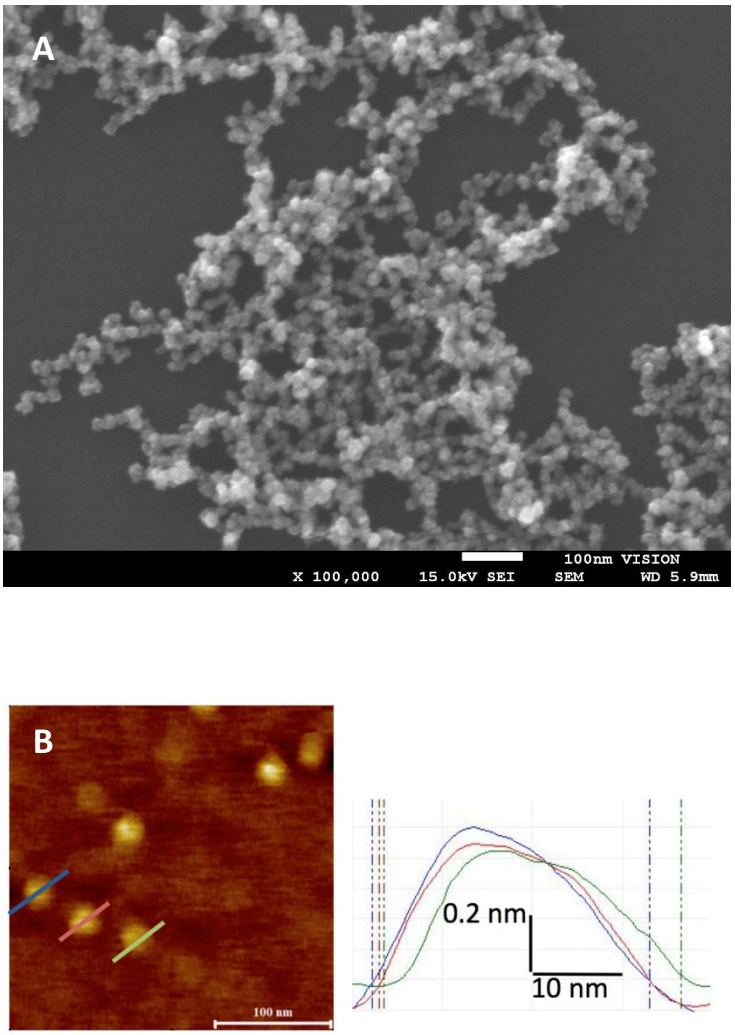

Figure 1. Particle size determined for DPV576 using SEM and AFM imaging. (A) Top image shows SEM image (100,000X magnification) displaying aggregation of particles and (B) bottom image shows AFM scan of isolated DPV576 particles. Line profiles of three individual particles are shown on the right with corresponding size of 20-40 nm.

DPV576-treated 4T1 cells show decreased Average Young's Modulus (*E*, KPa) measured by AFM

The average Young's modulus (*E*, kPa) was measured for cells and plotted against the relative frequency for all four groups: control (untreated) and DPV576-treated cells at concentrations (v/v): 5%, 10%, and 15% (Figure 2, A-D). Control cells demonstrated the highest average Young's modulus of 3.6 ± 0.2 kPa (A), while DPV576-treated cells showed a concentration dependent decrease in Young' modulus with average Young's modulus values of 2.8 ± 0.2 kPa at 5% (B), 2.2 ± 0.1 kPa at 10% (C), and 1.9 ± 0.3 kPa at 15% (D) DPV576 treatments respectively. All three DPV576-treated groups were significantly different from the control group values ($p<0.05$).

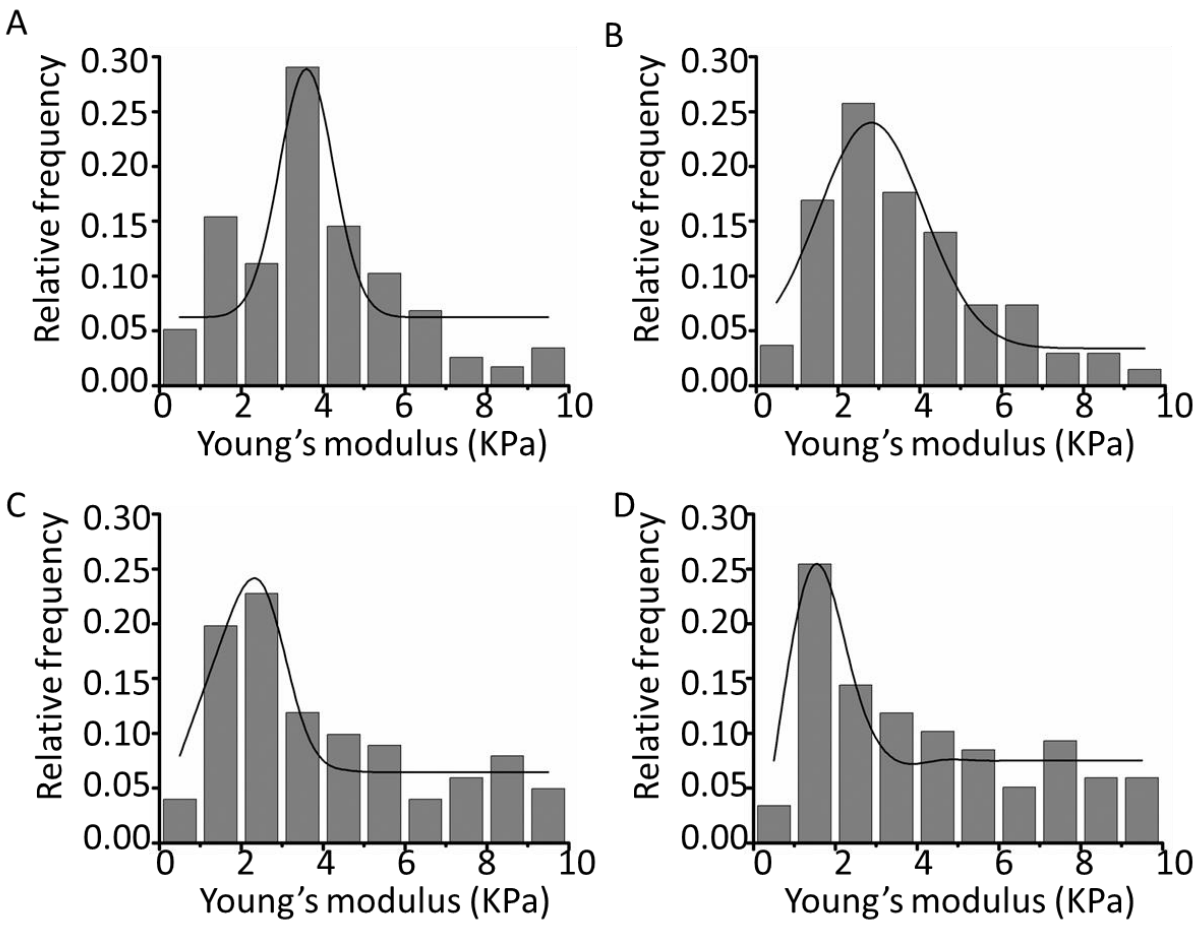

Figure 2. Average Young's modulus (kPa) DPV576-treated 4T1 cells shows significant reduction in cell stiffness after 2 hrs. Histograms showed relative frequency vs. Young's modulus with Gaussian fits for 4T1 cells. Data shows *E* values (Mean ± SD) for the control group (A), 5% DPV576 (B), 10% DPV576 (C), and 15% DPV576 (D) Cells were cultured in duplicate and 15 cells were measured from each set, giving a total of 30 cells per group. Results were compared using a Gaussian fitted histogram plot. All three DPV576-treated groups were significantly different from the control group values ($p<0.05$).

Localized Young's Modulus, (*E*, kPa) at Varying Indentation Depths

Cells treated with DPV576 displayed a distinct reduction in average stiffness of cells compared with those of untreated cells. However, the cell is not a homogeneous entity and the apparent stiffness of cells also relies on the complex array of sub-surface structures including the actin cytoskeleton, cytoplasm, and nucleus. Differentiating between the stiffness among these sub-structural regions allows for a better understanding of localized mechanical changes in cells upon treatment with DPV576. Therefore, we further explored the localized stiffness of 4T1 cells treated with different doses of DPV576 at various indentation depths [23, 24].

Figure 3(A) shows a schematic graph of the AFM indentation over the cell nuclear region. Figure 3(B) shows a sample of three subset ranges from the force-separation curve. Each subset data generated the localized stiffness of 4T1 cells at designated indentation depths. Stiffness measurements taken at varying indentation depths are plotted in Figure 3(C). *E* values for all of the 4T1 cells decreased with increasing indentation depths, which suggested that the cell surface regions were generally stiffer compared to those of the sub-surface regions. At each indentation depth (0.3, 0.6, and 0.9 μm cell indentation), cells treated with a higher dose of DPV576 displayed a lower stiffness, which was in agreement with previous results.

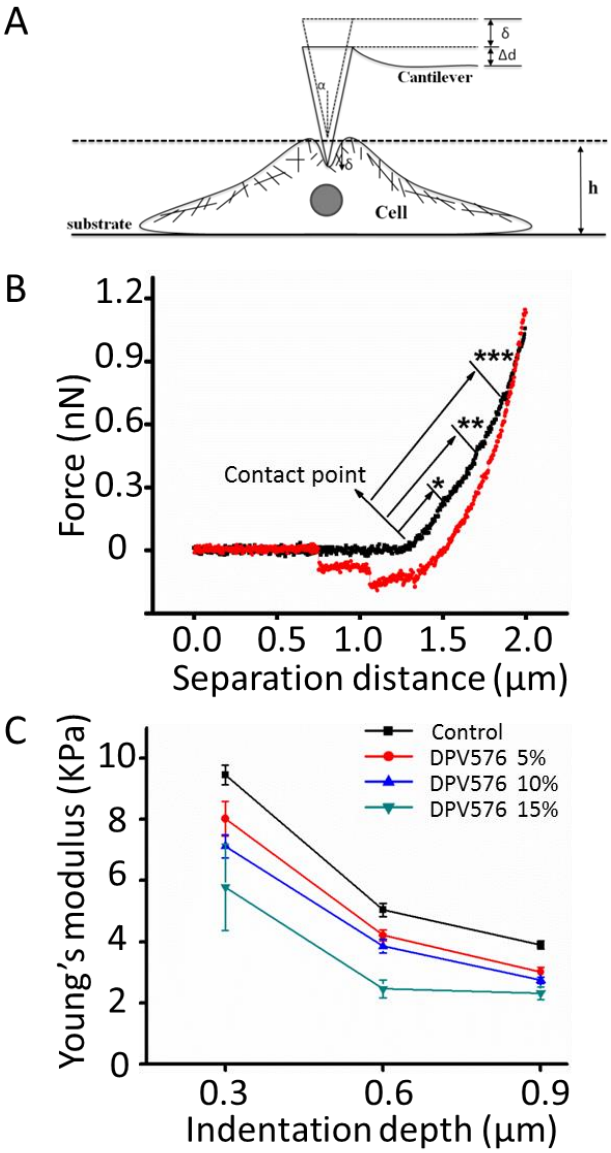

Figure 3. Cell modulus (E) of 4T1 cells were obtained at varying indentation depths with different concentrations of DPV576 treatment. (A) Schematic of the AFM indentation experiment above a cell with a conical tip. (B) A sample Force-separation curve is shown. The contact point was defined when the curve started to deviate from the baseline in the approach region (black curve) of the Force-separation curve. Approach region of typical Force-separation curve was divided into three distinct segments indicated by contact points. Each segment was fitted through the appropriate Sneddon model to acquire E (kPa) at the designated indentation depth. (C) Modulus of 4T1 cell nuclear regions at varying indentation depths. E values for all concentrations decreased at increased indentation depths. The stiffness of cells treated with a higher concentration of DPV576 became softer at all the indentation depths.

Filopodial Retraction (FR) and Retraction Rate

Filopodia are spike-like structures which play an integral role in cell migration and more particularly in metastasis. By studying the shape and retraction rate of filopodia, we can understand the changes in the cells' cytoskeletal network as it is undergoing metastasis [15]. Morphological changes in FR post treatment with DPV576 are shown in Figure 4. Control cells revealed little to no signs of FR (Figure 4, A-C). Cells treated with 5% DPV576 (D-F) showed microspike retraction. Cells treated with 10% DPV576 showed FR from single cells (G-I) as well as cell-cell separation events (J-L). Cells treated with 15% DPV576 showed FR from a single cell (M-O) as well as cell-cell separation events (P-R). All cells were monitored over the course of 40 minutes.

FR rates of cells were measured for each of the four groups and plotted as retraction distance in nanometers vs. time in minutes. It was noted that the control (diamond) and 5% DPV576 (square) groups demonstrated similar velocities of 0.30 μm/min and corresponded to the lowest velocity trends out of all four groups. 10% DPV576 (triangle) treated cells showed an intermediate rate of 0.5 μm/min of FR. 15% DPV576 (circle) treated cells showed the steepest velocity of 1.425 μm/min, indicating the highest rate of FR (Figure 5).

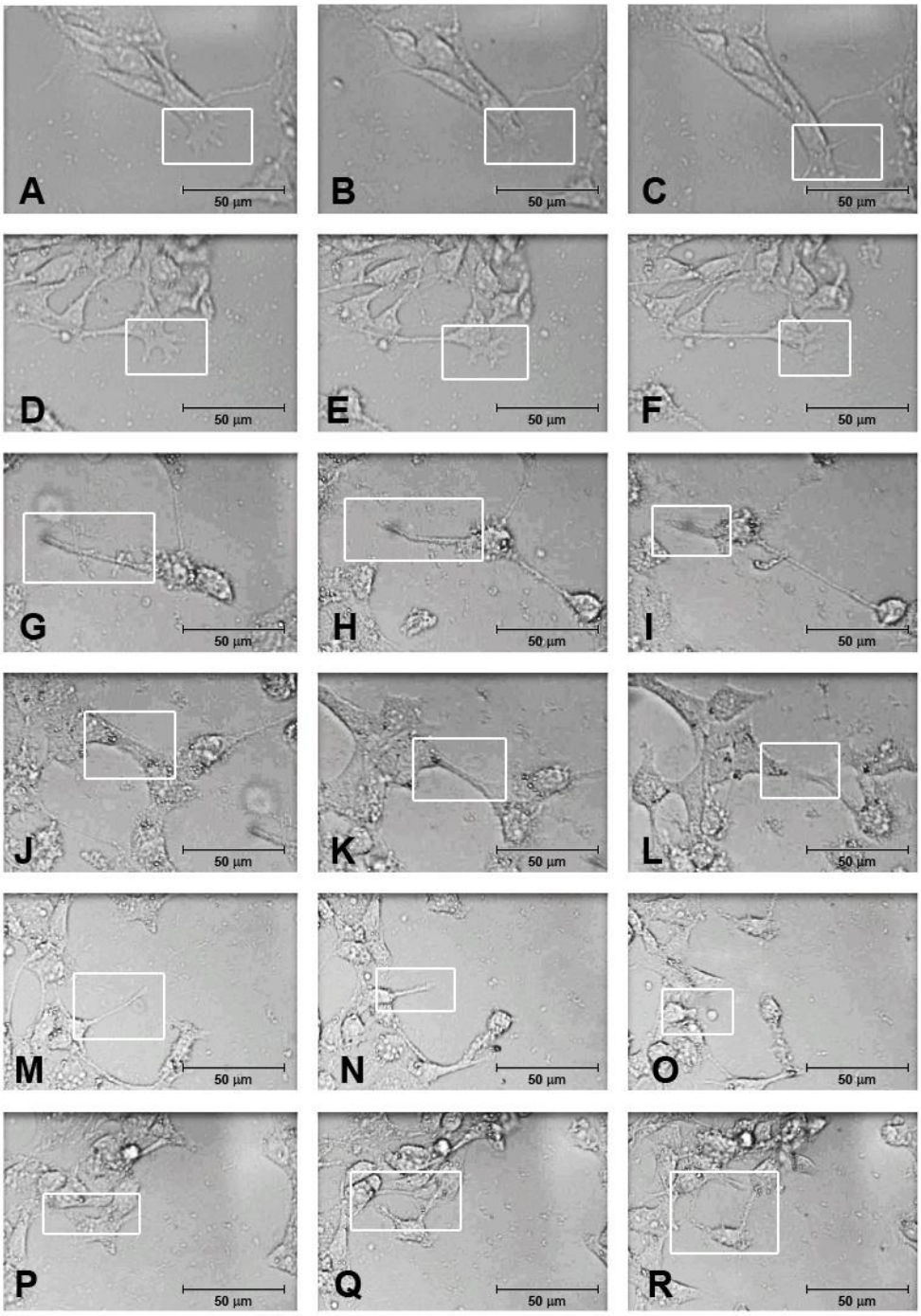

Figure 4. Changes in cell morphology post exposure to increasing concentrations of DPV576. Cell extensions imaged at 0 minutes (left column), 20 minutes (middle) and at 40 minutes (right). Control cells are shown in panels A-C, 5% DPV576 treated cells show partial FR in panels D-F, 10% DPV576 caused partial FR in panels G-I as well as cell-cell separation events causing by filopodial collapse in panels J-L, 15% DPV576 caused complete FR in panels M-O as well as cell-cell separation events caused by filopodial collapse in panels P-R.

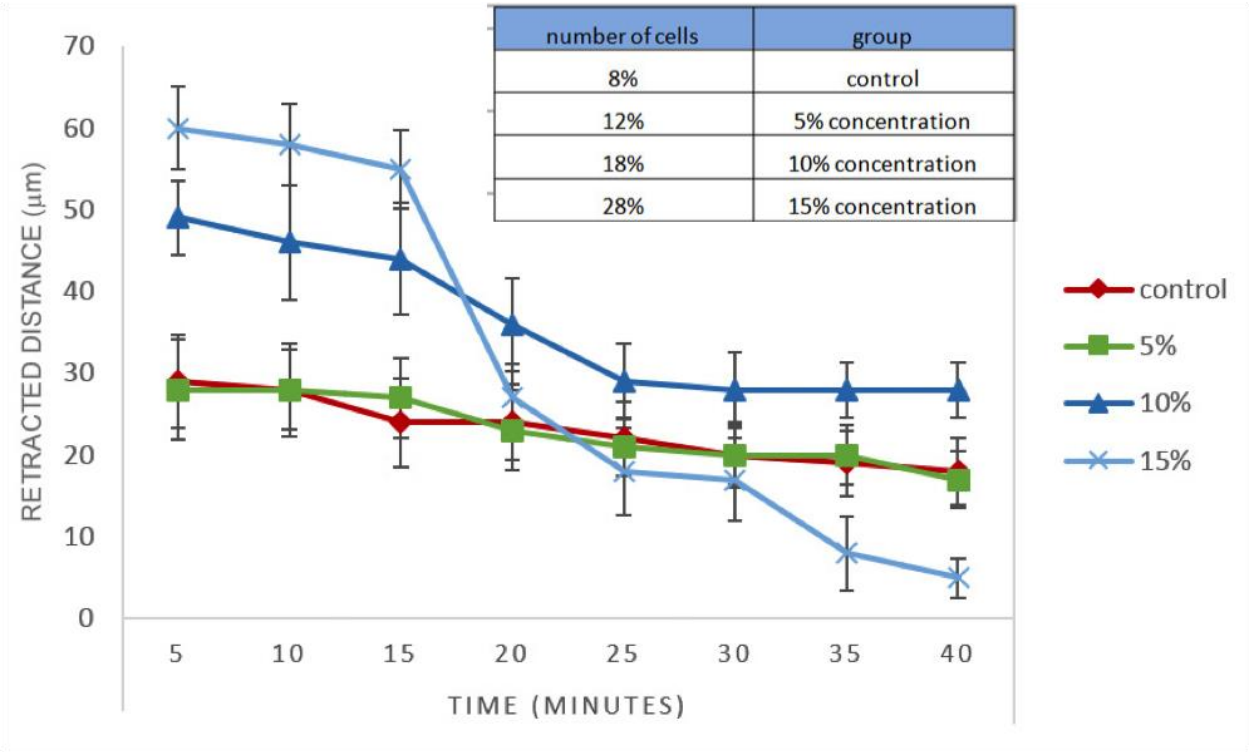

Figure 5. Measure of Concentration Dependent Changes in Rate of FR rates were measured using retraction distance (µm) over time (minutes). Table shows the number of cells (out of 100 cells) with retracted filopodia. The length of retracted filopodia was measured every five minutes over a 40-minute period. Diamond shaped line shows control (untreated cells) rate, square line shows 5% DPV576, triangle line shows 10% DPV576 and circle line shows 15% DPV576. A series of time-lapse images were compared over the course of 40 minutes and the total number of FRs and extensions were measured to acquire data points.

Changes in structural characteristics in cellular Filopodia upon treatment with DPV576, observed via AFM imaging

Atomic force microscopy (AFM) enables high-resolution three-dimensional (3D) imaging of cultured cells. Cells grown on culture dishes were immobilized by a quick fixation step to preserve their transient cellular morphologies followed by AFM characterization in buffer. This approach preserves the structural integrity of individual cells and allows visualization of membrane morphologies, such as microvilli and filopodia. Additional information including the 3D measurements of these characteristic features can be attained from AFM topographs. We examined the filopodial structure for both untreated and cells post treatment with DPV576 using high resolution AFM imaging. Figure 6A exhibits filopodia from an untreated cell and shows an organized network of straight and well-organized filaments within the filopodia region. However, treatment of 4T1 cells with DPV576 at a concentration of 15% for one hour caused significant changes in the filopodial architecture.

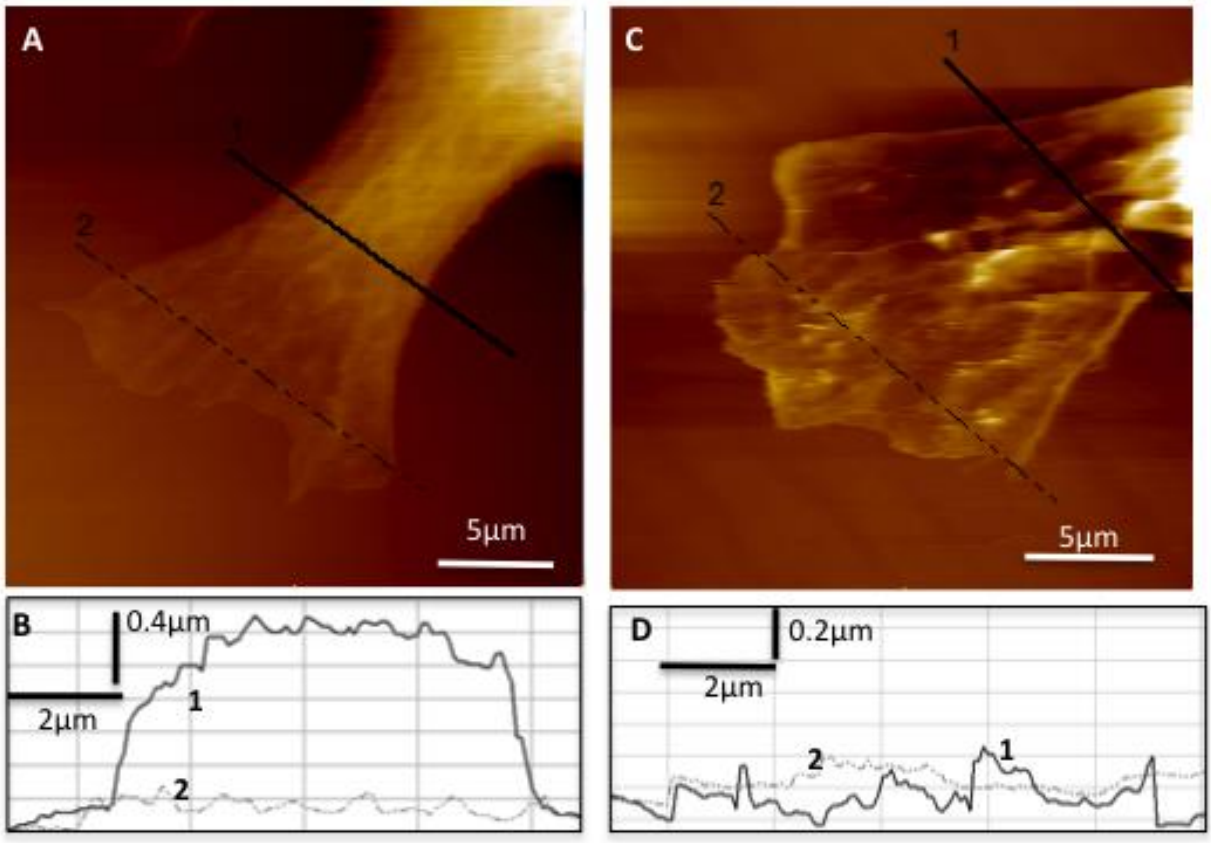

Figure 6. Representative AFM Images of untreated and DPV576 treated 4T1 cells showing structural changes in filopodia regions (A) Filopodia from an untreated cells shows several organized parallel filaments (B) Line profile across two different regions of the filopodia extensions (marked 1, solid black; 2, grey dotted line) show topographic heights of around 1-2µm. (C) A 4T1 cell treated with 15% DPV576 displaying lack of filament organization at the cell edge (D) Topographic height of the filopodia (marked 1, solid black; 2, grey dotted line) show flattened (<0.5µm) cellular edges, suggesting loss of cytoskeleton architecture upon DPV576 treatment as observed in C and D.

3.5 Discussion

Cellular bio-mechanics plays a very important role in cellular metabolism and cell functions, as cell growth, proliferation, migration, adhesion, and differentiation are all reported to be highly dependent on and regulated by cellular nanomechanical properties [25-28]. Our previous work has indicated that NDs could induce the morphological damage of multi-drug resistant, human leukemic cells (HL60/AR) cells based on AFM topographical imaging [29] but the effect of DPV576 NPs on the nanomechanical properties of single cells remained unexplored. As differences in cell morphology might also lead to difference in their nanomechanical characteristics, we further used AFM force spectroscopy to probe the nanomechanical changes at the single cell level by probing average and localized, depth dependent Young's modulus from control and DPV treated 4T1 cells. In the current study, we showed that 4T1 metastatic breast cancer cells, exposed to DPV576 resulted in decreased cell stiffness of 4T1 cells compared to control cells in a dose dependent manner. Furthermore, the localized cell modulus values for all doses of 4T1 cells decreased with increasing indentation depths, suggesting that the cell surface regions were generally stiffer compared to those of the sub-surface regions. At each indentation depth, cells treated with a higher dose of DPV576 displayed a lower stiffness. Our results showing that DPV576 NPs can decrease the Young's modulus of 4T1cells can be compared to similar findings from other studies that reported reduction in cell stiffness of fibroblasts by silica nanoparticles [30] or reduction in stiffness of tumor epithelial cells and reduced tumor size influenced by carbon nanorods [31]. Other nanoparticles [27] such as cobalt acetate also exhibited a decrease in the stiffness of *Brevibacteriumcasei* cells [32]. Titanium oxide nanoparticles were shown to increase stiffness of human neutrophils [33] while decreasing stiffness in human skin fibroblasts [34]. The significant reduction observed in 4T1 cell modulus

within 2 hours of exposure to DPV576 solution, may have implications in delivery of drug molecules through changes in local membrane fluidity and modification of drug-intracellular pathways.

The cytoskeleton serves as an intricate structural framework that predominately shapes a cell and provides mechanical rigidity [35]. In particular, F-actin is reported as a potential target of nanomaterials in cancer cells [36] and the integrity of actin network can be reflected by the Young's modulus measurement by AFM [37]. Constant alterations in actin organizational networks occur during cancer cell migration and extravasation. In particular, actin polymerization results in the formation of slender protrusive structures known as invadopodia and filopodia. These protrusions are used by the cell to move through the extracellular matrix, migrate through the vasculature and tunnel to a new tumor site [15]. To further study the role of F-actin in NPs induced Young's modulus changes of 4T1 cells, we measured the morphological changes in FR post treatment with DPV576. Our results indicate that the DPV576 treatment of cells showed an increased and rapid rate of FR compared to control cells.

Additionally, filopodia, associated with cell spreading, were captured and visualized in three dimensions and revealed high-density ridges and sub-cellular cytoskeleton organization of cellular extensions. The AFM imaging approach provided an effective means to characterize these cellular extensions and the changes associated with DPV576 treatment of cells at high resolution. The quantitative imaging and measurements allowed for systematic correlation of membrane structural extensions with the cellular changes in DPV treated cells. Based on the 3D topographic images obtained using AFM, it is evident that that the structural cytoskeletal

organization of the cells is altered. The filopodia retract upon DPV576 treatment, resulting in rapid loss of filamentous actin bundles within the cell extensions. The filopodia become significantly flattened compared to untreated controls, likely due to loss of architecture within the cellular cytoskeleton. It appears that the changes in cellular cytoskeleton propagate along the cell length, thereby influencing the reduction both the average and localized depth dependent Young's modulus of the treated cells.

3.6 Conclusions

DPV576 has the ability to decrease the stiffness of metastatic breast cancer cells and restructure their filopodia organization. Using AFM based average cell modulus and depth dependent analysis, we were able to detect a dose dependent decrease in cell stiffness (as measured using Young's modulus) for DPV576 treated cells. Moreover, time lapse light microscopy and AFM imaging revealed that DPV576 treatment caused FR and filopodial degeneration in cells. The AFM imaging approach provided an effective method to characterize the cellular extensions and the changes associated with DPV576 treatment of cells at high resolution. Our study reveals the important biophysical and morphological effects of DPV576 on metastatic cells and suggests that it maybe useful as an anti-metastatic agent by decreasing cell stiffness.

3.7 Supplementary information

AFM indentation theory:

The mechanical properties of linear, isotropic, and elastic materials can be described by two intrinsic parameters, the Young's modulus E and the Poisson's ratio v. The indentation experiments with AFM are performed to characterize the mechanical properties of biological samples, especially cells in physiological conditions. The collected data are in the form of $F = f(z)$ where F represents force executed by the cantilever, and z is the piezo-actuator translation.

The piezo-translation distance Δz equals the sum of the cantilever deflection Δd and the sample indentation δ,

$$\Delta z = \Delta d + \delta, \tag{1}$$

With a conical tip, the indentation depth and the applied force are connected through the Sneddon's model [38]:

$$F = \frac{2}{\pi} \times \tan\alpha \times \frac{E}{1-\nu^2} \times \delta^2, \tag{2}$$

where F is the applied force, δ is indentation, α is the half-opening angle of the cone, E is the Young's modulus of the sample, and v is the Poisson's ratio (v = 0.499, assuming the cell to be an incompressible solid [39]). To avoid the effects of the substrate over the stiffness measurements, only a small indentation which is less than 10% of the thickness of the sample was considered for the Sneddon's model.

Data analysis:

A statistically reliable force spectroscopy experiment consists typically of hundreds of force-distance curves. Thus a stable procedure to detect and process an extended data set is essential. We developed MATLAB (Mathworks) based routines for the analysis of force-distance curves. The customized program fulfills functions such as fitting the force-indentation data with appropriate Sneddon's model and acquiring stiffness at varying indentation depth.

The contact point is first determined over a 4 μm ramp in all force-distance curves. The apparent loading force deviated from the baseline and started to increase once the tip indented into the sample [40] (Figure 2b). Linear fitting was applied to the first 1um in the force-distance curve, and the R^2 regression was recorded. The same process of linear fitting was done at small increases of 40 nm. The contact point was chosen when the R^2 regression was twice as large as the value in the first 1μm. The acquired contact point was plotted in the same graph with the Force-separation curve, allowing one to adjust the threshold parameters based on performance.

Subsequently, force-indentation data was converted from the Force-separation data based on equation (1). Young's moduli were fitted over the force-indentation data through the least square method with R^2 regression of 0.9 using Sneddon's model (equation (2)). Stiffness at varying indentation depths was further determined by repeatedly increasing the fitting range by 300 nm starting from the contact point.

3.8 References

[1] Xing Y and Dai L 2009 Nanodiamonds for nanomedicine *Nanomedicine***4** 207-18

[2] Mochalin V N, Shenderova O, Ho D and Gogotsi Y 2012 The properties and applications of nanodiamonds *Nature nanotechnology***7** 11-23

[3] Chang Y R, Lee H Y, Chen K, Chang C C, Tsai D S, Fu C C, Lim T S, Tzeng Y K, Fang C Y, Han C C, Chang H C and Fann W 2008 Mass production and dynamic imaging of fluorescent nanodiamonds *Nature nanotechnology***3** 284-8

[4] Kotov N A 2010 Chemistry. Inorganic nanoparticles as protein mimics *Science***330** 188-9

[5] Thalhammer A, Edgington R J, Cingolani L A, Schoepfer R and Jackman R B 2010 The use of nanodiamond monolayer coatings to promote the formation of functional neuronal networks *Biomaterials***31** 2097-104

[6] Zhang Q, Mochalin V N, Neitzel I, Knoke I Y, Han J, Klug C A, Zhou J G, Lelkes P I and Gogotsi Y 2011 Fluorescent PLLA-nanodiamond composites for bone tissue engineering *Biomaterials***32** 87-94

[7] Chow E K, Zhang X Q, Chen M, Lam R, Robinson E, Huang H, Schaffer D, Osawa E, Goga A and Ho D 2011 Nanodiamond therapeutic delivery agents mediate enhanced chemoresistant tumor treatment *Science translational medicine***3** 73ra21

[8] Schrand A M, Huang H, Carlson C, Schlager J J, Omacr Sawa E, Hussain S M and Dai L 2007 Are diamond nanoparticles cytotoxic? *The journal of physical chemistry. B***111** 2-7

[9] Yuan Y, Wang X, Jia G, Liu J-H, Wang T, Gu Y, Yang S-T, Zhen S, Wang H and Liu Y 2010 Pulmonary toxicity and translocation of nanodiamonds in mice *Diamond and Related Materials***19** 291-9

[10] Sharma S, Santiskulvong C, Bentolila L A, Rao J, Dorigo O and Gimzewski J K 2012 Correlative nanomechanical profiling with super-resolution F-actin imaging reveals novel insights into mechanisms of cisplatin resistance in ovarian cancer cells *Nanomedicine : nanotechnology, biology, and medicine***8** 757-66

[11] Cross S E, Jin Y S, Rao J and Gimzewski J K 2007 Nanomechanical analysis of cells from cancer patients *Nat Nanotechnol***2** 780-3

[12] Suresh S 2007 Nanomedicine: elastic clues in cancer detection *Nature nanotechnology***2** 748-9

[13] Suresh S 2007 Biomechanics and biophysics of cancer cells *Acta Biomater***3** 413-38

[14] Yau W L, Lam C S, Ng L, Chow A K, Chan S T, Chan J Y, Wo J Y, Ng K T, Man K, Poon R T and Pang R W 2013 Over-expression of miR-106b promotes cell migration and metastasis in hepatocellular carcinoma by activating epithelial-mesenchymal transition process *PloS one***8** e57882

[15] Machesky L M 2008 Lamellipodia and filopodia in metastasis and invasion *FEBS letters***582** 2102-11

[16] Kim J, Takahashi M, Shimizu T, Shirasawa T, Kajita M, Kanayama A and Miyamoto Y 2008 Effects of a potent antioxidant, platinum nanoparticle, on the lifespan of Caenorhabditis elegans *Mechanisms of Ageing and Development***129** 322-31

[17] Porcel E, Liehn S, Remita H, Usami N, Kobayashi K, Furusawa Y, Le Sech C and Lacombe S Platinum nanoparticles: a promising material for future cancer therapy? *Nanotechnology***21**

[18] Mohammadi H, Abedi A, Akbarzadeh A, Mokhtari M, Shahmabadi H, Mehrabi M, Javadian S and Chiani M Evaluation of synthesized platinum nanoparticles on the MCF-7 and HepG-2 cancer cell lines *International Nano Letters C7 - 28***3** 1-5

[19] Manikandan M, Hasan N and Wu H-F Platinum nanoparticles for the photothermal treatment of Neuro 2A cancer cells *Biomaterials***34** 5833-42

[20] Ghoneum M, Ghoneum A and Gimzewski J 2010 Nanodiamond and nanoplatinum liquid, DPV576, activates human monocyte-derived dendritic cells in vitro *Anticancer research***30** 4075-9

[21] Hutter J L and Bechhoefer J 1993 CALIBRATION OF ATOMIC-FORCE MICROSCOPE TIPS (VOL 64, PG 1868, 1993) *Review of Scientific Instruments***64** 3342-

[22] Staunton J R, Fuhrmann A, Nandakumar V, Banyai N, Davies P C W and Ros R AFM Stiffness Nanotomography of Normal, Metaplastic and Dysplastic Human Esophageal Cells *Biophysical Journal***100** 190-

[23] Roduit C, Sekatski S, Dietler G, Catsicas S, Lafont F and Kasas S 2009 Stiffness Tomography by Atomic Force Microscopy *Biophysical Journal***97** 674-7

[24] Kasas S and Dietler G 2008 Probing nanomechanical properties from biomolecules to living cells *Pflugers Archiv-European Journal of Physiology***456** 13-27

[25] Cross S E, Jin Y S, Tondre J, Wong R, Rao J and Gimzewski J K 2008 AFM-based analysis of human metastatic cancer cells *Nanotechnology***19** 384003

[26] Silberberg Y R, Yakubov G E, Horton M A and Pelling A E 2009 Cell nanomechanics and focal adhesions are regulated by retinol and conjugated linoleic acid in a dose-dependent manner *Nanotechnology***20** 285103

[27] Lee S M, Nguyen T H, Na K, Cho I J, Woo D H, Oh J E, Lee C J and Yoon E S 2014 Nanomechanical measurement of astrocyte stiffness correlated with cytoskeletal maturation *Journal of biomedical materials research. Part A*

[28] Plodinec M, Loparic M, Monnier C A, Obermann E C, Zanetti-Dallenbach R, Oertle P, Hyotyla J T, Aebi U, Bentires-Alj M, Lim R Y and Schoenenberger C A 2012 The nanomechanical signature of breast cancer *Nature nanotechnology***7** 757-65

[29] Ghoneum A, Sharma S and Gimzewski J 2013 Nano-hole induction by nanodiamond and nanoplatinum liquid, DPV576, reverses multidrug resistance in human myeloid leukemia (HL60/AR) *International journal of nanomedicine***8** 2567-73

[30] Gaharwar A K, Kishore V, Rivera C, Bullock W, Wu C J, Akkus O and Schmidt G 2012 Physically crosslinked nanocomposites from silicate-crosslinked PEO: mechanical properties and osteogenic differentiation of human mesenchymal stem cells *Macromolecular bioscience***12** 779-93

[31] Lee J, Chu B H, Sen S, Gupte A, Chancellor T J, Chang C Y, Ren F, Kumar S and Lele T P 2011 Modulating malignant epithelial tumor cell adhesion, migration and mechanics with nanorod surfaces *Biomedical microdevices***13** 89-95

[32] Kumar U, Vivekanand K and Poddar P 2009 Real-time nanomechanical and topographical mapping on live bacterial cells-Brevibacterium casei under stress due to their exposure to Co2+ ions during microbial synthesis of Co3O4 nanoparticles *The journal of physical chemistry. B***113** 7927-33

[33] da Rosa E L 2013 Kinetic effects of TiO2 fine particles and nanoparticles aggregates on the nanomechanical properties of human neutrophils assessed by force spectroscopy *BMC biophysics***6** 11

[34] Vileno B, Lekka M, Sienkiewicz A, Jeney S, Stoessel G, Lekki J, Forro L and Stachura Z 2007 Stiffness alterations of single cells induced by UV in the presence of nanoTiO2 *Environmental science & technology***41** 5149-53

[35] Guck J, Schinkinger S, Lincoln B, Wottawah F, Ebert S, Romeyke M, Lenz D, Erickson H M, Ananthakrishnan R, Mitchell D, Kas J, Ulvick S and Bilby C 2005 Optical deformability as an inherent cell marker for testing malignant transformation and metastatic competence *Biophys J***88** 3689-98

[36] Wang L, Liu Y, Li W, Jiang X, Ji Y, Wu X, Xu L, Qiu Y, Zhao K, Wei T, Li Y, Zhao Y and Chen C 2011 Selective targeting of gold nanorods at the mitochondria of cancer cells: implications for cancer therapy *Nano letters***11** 772-80

[37] Solon J, Levental I, Sengupta K, Georges P C and Janmey P A 2007 Fibroblast adaptation and stiffness matching to soft elastic substrates *Biophysical journal***93** 4453-61

[38] Sneddon I N 1948 Boussinesq's problem for a rigid cone *Proceedings of the Cambridge Philosophical Society* **44** 492-507

[39] Charras G T, Lehenkari P P and Horton M A 2001 Atomic force microscopy can be used to mechanically stimulate osteoblasts and evaluate cellular strain distributions *Ultramicroscopy***86** 85-95.

[40] Rico F, Roca-Cusachs P, Gavara N, Farré R, Rotger M and NavajasF D 2005Probing mechanical properties of living cells by atomic force microscopy with blunted pyramidal cantilever tips *Physical ReviewE* **72** 021914.

Chapter 4.

The Effect of Trypsin-EDTA on the Mechanical Properties of Cells

4.1 Abstract

Nano-indentation has become a common technique to obtain mechanical information of biomaterials, including cells. The stiffness of cells has a potential to be a marker for cancer diagnosis and decipher the metastasis mechanism. Here we studied the stiffness of three cell lines possessing different metastatic potentials. We observed benign cell lines (HUC-BC and HUC-PC) to have a higher Young's modulus than the malignant cell line (MC-T11). We further investigated thechanges in stiffness and adhesions of benign cell lines varying trypsin-EDTA treatment time. Both cell lines showed smaller Young's modulus when treated with trypsin-EDTA. HUC-BC showed time-dependent changes in Young's modulus while HUC-PC did not. The adhesion force of cells wasreduced by trypsin-EDTA treatment; however, the bright field image showed no difference with or without the treatment. Our results demonstrate the changes in the mechanical information of cells occurring in basic cell experiment which may provide relevantand novel information in studying cell mechanics in general.

4.2 Introduction

In cell biology, cell culture and the manipulation of cells has become a common and valuable research tool. Traditionally, research has been focused on how acellis composed of each organelle and how the proteins and nucleic acids in cells facilitate and dictate with certain structures and function. In addition to the biochemical information of cells, the mechanical information of cells is available with advances in nano-indentation techniques [1-3]. Among various aspects regarding the mechanical information of cells, we are seeking to answer how the stiffness of cells is related to the cancer metastasis [4-5]. The Gimzewski group has previously reported that cancer cells are softer than healthy control cells indicating the stiffness of cells and thus may serve as a marker for cancer [6-7]. We observed the changes in the stiffness of metastatic cancer cells depending on an anti-cancer agent treatment [8]. Interestingly, in case of a cisplatin resistant cancer cells, there was no change in the stiffness of cells when treated with cisplatin [9-10]. Thus, the change in mechanical properties of the cells may reveal cancer cell mechanism regarding drug resistance and cancer metastasis.

Trypsin is one of the most studied and utilized protein. It is a serine protease and the structure, function, and mechanism of trypsin is well-known. Trypsin is also used in cell cultureas a mixture with ethylenediaminetetraacetic acid (EDTA) since the mixture enables the detachment of the adhesive cells from the surface. Trypsin loosens cell-cell adhesions via protease activity and EDTA deactivates cadherins which are a key transmembrane protein for cell adhesions. The activity of cadherins depends on ca^{2+} that EDTA can detain from them resulting in inactivation of cadherins [11]. Though trypsin-EDTA is commonly treated to cells, less is known how it affects the mechanics of cells. Oberleithner *et al.* studied how potassium softens vascular endothelium and showed a low dose of trypsin (10 ng/ml) stiffens the cell cortex [12]. However, the trypsin

concentration is very low compared to the typical concentration to detach cells, 0.25 % (equivalent to 2.5×10^6 ng/ml). To understand the effect of a high dose trypsin-EDTA to the mechanics of cells, we studied the mechanical changes of cells varying trypsin-EDTA treatment time using atomic force microscope (AFM).

Among the various cell lines, human urothelial cell (HUC) model was chosen. Normal HUCs are infected then immortalized by SV-40 virus and several interesting cell lines are established [13-15]. HUC-BC cell line is not transformed and not transformable by 4-aminobiphenyl (4-ABP), a known carcinogen for bladder cancer, or *ras* oncogene. HUC-PC cell line is not transformed but transformable by 4-ABP or *ras* oncogene. MC-T11 cell line is a transformed low-grade tumor and has a potential to be a malignant high-grade tumor when treated with 4-ABP [15]. All three cell lines are originated from the same progenitor cells but possessing different metastatic potentials. Thus, HUC model would give insight on how the mechanics of cells are changing with the progresses of cancer metastasis. In this study, we first confirmed the stiffness of three cell lines. Since HUC-BC and HUC-PC have similar biochemical properties before the induction by 4-ABP we tested the changes in mechanical properties of HUC-BC and HUC-PC upon a trypsin-EDTA treatment.

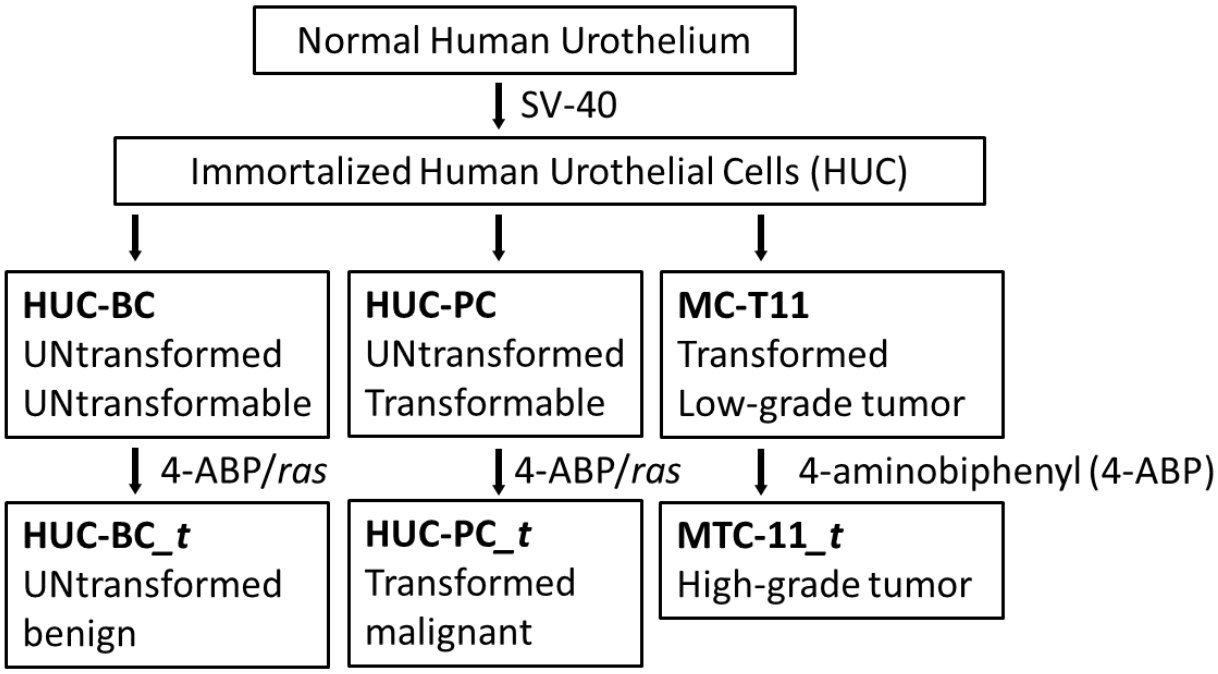

Figure 1. Human urothelial cell (HUC) model. Three cell lines, HUC-BC, HUC-PC, and MC-T11, have different metastatic potentials depending on 4-aminobiphenyl treatment.

3. Materials and Methods

Cell Culture: Bladder cancer cell lines, HUC-BC, HUC-PC, and MC-T11, were cultured in RPMI 1640 supplemented with 10% heat-inactivated FBS, 2 mM L-Glutamine, 100 units/mL Penicillin G, and 100 µg/mL Streptomycin Sulfate.

Trypsin Treatment and Cytospin: Cells were treated with 0.25% trypsin in 1 mM EDTA solution for 6 or 8 min and then the cell culture media is added to inactivate trypsin. Fluent cells are gently attached to glass slides by Cytospin3 (Thermo Fisher Scientific, MA, USA) with 30 g for 10 min. 100 µL of PBS was added before AFM measurement.

AFM: All measurements were conducted on live cells with PBS using a Catalyst atomic force microscope (Bruker Instruments, CA, USA) with a combined inverted optical/confocal microscope (Zeiss Corp, NY, USA). This combination permits lateral positioning of the AFM tip over the cell nucleus center with submicron precision. AFM mechanical measurements were collected in contact mode using MLCT-C cantilevers (Bruker Instruments, CA, USA). Mechanical measurements were obtained at 37°C with force measurements recorded at a pulling rate of 0.5 Hz. AFM measurements were obtained in at least 25 live cells without fixing for both trypsin-treated and untreated samples with a maximum applied force of 2 nN. The AFM tip was always precisely positioned (within micron range) on top of the cell nuclear regions using motorized stage and 200X inverted optical view of the combined confocal-AFM microscope.

4. Result and Discussions

Average Young's modulus in correlation to cancer metastatic potentials

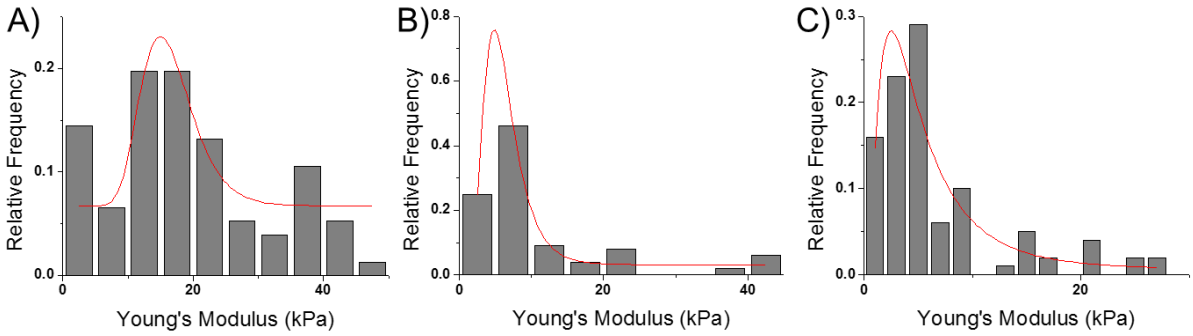

Figure 2. Average Young's modulus of HUC model cell lines; HUC-BC (A), HUC-PC (B), and MC-T11 (C). Histograms plotted relative frequency versus Young's modulus with Log-normal fits.For each condition, 25 cells were measured with ten force curves.

The average Young's modulus was measured for each cell line (Figure 2). HUC-BC showed the largest Young's modulus value (A) and followed by HUC-PC (B), and MC-T11 showed the smallest Young's modulus value (C). This result matches with the previous research that malignant cancer cells are softer than control healthy cells. The average Young's modulus value with a standard deviation of HUC-BC, HUC-PC, and MC-T11 is 19.5 ± 11.6 kPa, 11.2 ± 10.5 kPa, and 6.7 ± 6.2 kPa, respectively. The average Young's modulus values match with the metastatic potentials. HUC-BC cells that are benign and untransformable by 4-ABP were the stiffest while MC-T11 cells that are a malignant low-grade tumor are the softest. It is notable that all the cell lines are not treated by 4-ABP. Even before induction by 4-ABP HUC-BC showed higher Young's modulus value than HUC-PC.

Trypsin-EDTA treatment lowers Young's modulus of cells

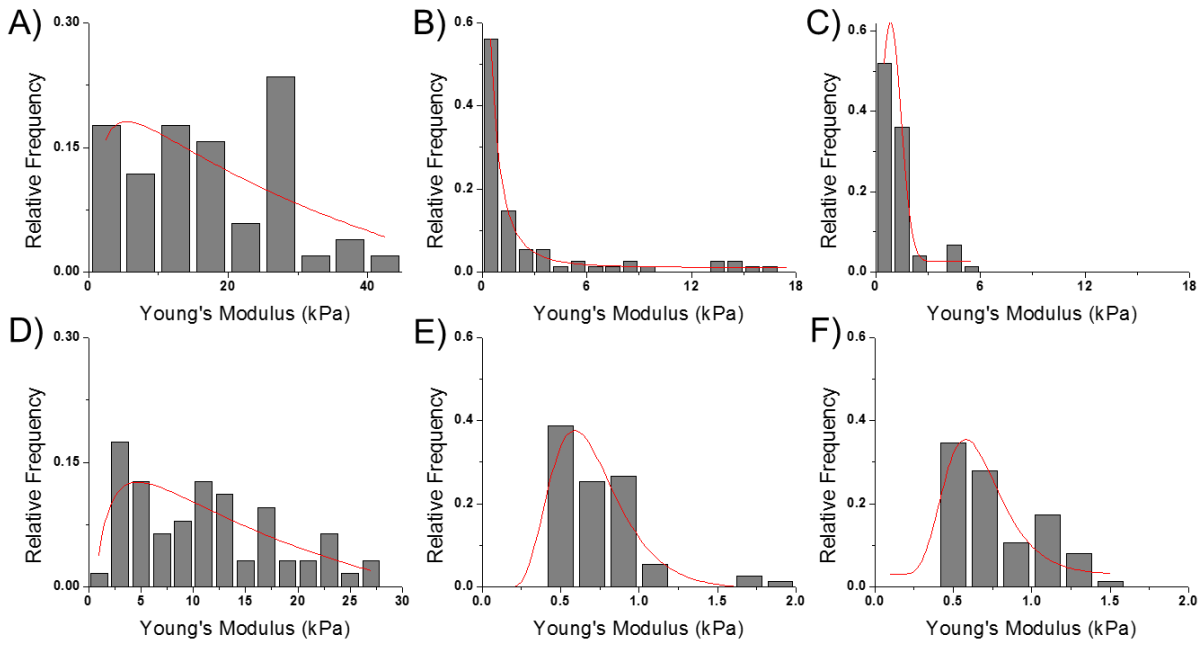

Figure 3. Average Young's modulus of trypsin-EDTA treated cells shows asignificant reduction in stiffness. Histograms plotted relative frequency versus Young's modulus with Log-normal fits ((A), (B), (D), (E), and (F)) or Gaussian fits (C). Upper panel shows HUC-BC cells with (A) no treatment, (B) 6 min treatment, and (C) 8 min treatment and lower panel shows HUC-PC cells with (D) no treatment, (E) 6 min treatment, and (F) 8 min treatment. For each condition, 25 cells were measured with ten force curves. The stiffness of all trypsin-EDTA treated cells were significantly different from the corresponding control group ($p<0.05$),and HUC-BC cells showed time-dependent stiffness difference ($p < 0.05$).

We were interested to observe the mechanical difference in HUC-BC and HUC-PC depending on trypsin-EDTA treatments since two cell lines showed different Young's modulus values before 4-ABP treatments. The average Young's modulus was measured and analyzed for two cell lines with three groups: HUC-BC cells with untreated control, 6 min trypsin-EDTA treatment, and 8 min trypsin-EDTA treatment and HUC-PC cells with untreated control, 6 min trypsin-EDTA treatment, and 8 min trypsin-EDTA treatment (Figure 3 (A)-(E)).In both cell lines, untreated control groups showed highest average Young's modulus values; HUC-BC control has an average with standard deviation of 17 ± 11 kPa (A) and HUC-PC control has 11 ± 7 kPa (D).The trypsin-EDTA treatedgroups showed smaller average Young's modulus values compared to the corresponding controls; HUC-BC with 6 min trypsin-EDTA treatment has an average with standard deviation of 2.8± 4.1 kPa (B), HUC-BC with 8 min trypsin-EDTA treatment has 1.3 ± 1.1 kPa (C), HUC-PC with 6 min trypsin-EDTA treatment has 0.74 ± 0.29 kPa (E), and HUC-PC with 8 min trypsin-EDTA treatment has 0.78 ± 0.28 kPa (F).The stiffness of all trypsin-EDTA treated cells were significantly higher than each corresponding control group ($p<0.05$). It isnotable that HUC-BC cells showed significantly lower Young's modulus value with two min additional trypsin-EDTA treatment time ($p < 0.05$) while HUC-PC cells did not. Since each cell line shows different trypsin-EDTA sensitivity, the stiffness changes by trypsin-EDTA treatment might also depend on cell lines.

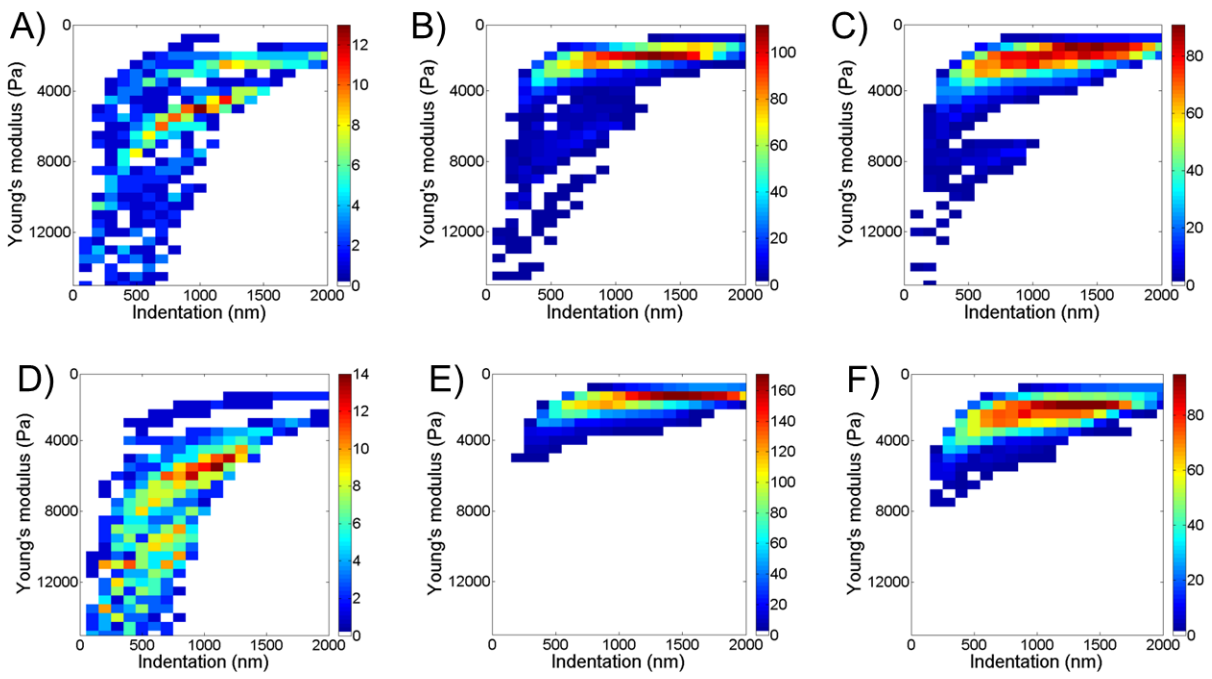

Figure 4.Localized cell stiffness of trypsin-EDTA treated cells shows asignificant reduction in stiffness plotted as 2D heat maps of stiffness versus indentation matrix. Upper panel shows HUC-BC cells with (A) no treatment, (B) 6 min treatment, and (C) 8 min treatment and lower panel shows HUC-PC cells with (D) no treatment, (E) 6 min treatment, and (F) 8 min treatment.

In the average Young's modulus analysis, we assumed that cells are a homogeneous material. However, cells are composed of various inner organelles such as nucleus, cytoplasm, and cytoskeleton which may affect the stiffness of cells. We have analyzed the indentation depth dependent stiffness as described in the previous studies [8-9]. Figure 4 shows the localized cell stiffness of cells with and without trypsin-EDTA treatment. We can observe a peak shift of Young's modulus in both cell lines. HUC-BC and HUC-PC cells shows a broader heat map before the treatment and the peak is shifting upsideto have smaller Young's modulus values which agrees with the average analysis.

Trypsin-EDTA treatment lowers adhesion forces of cells

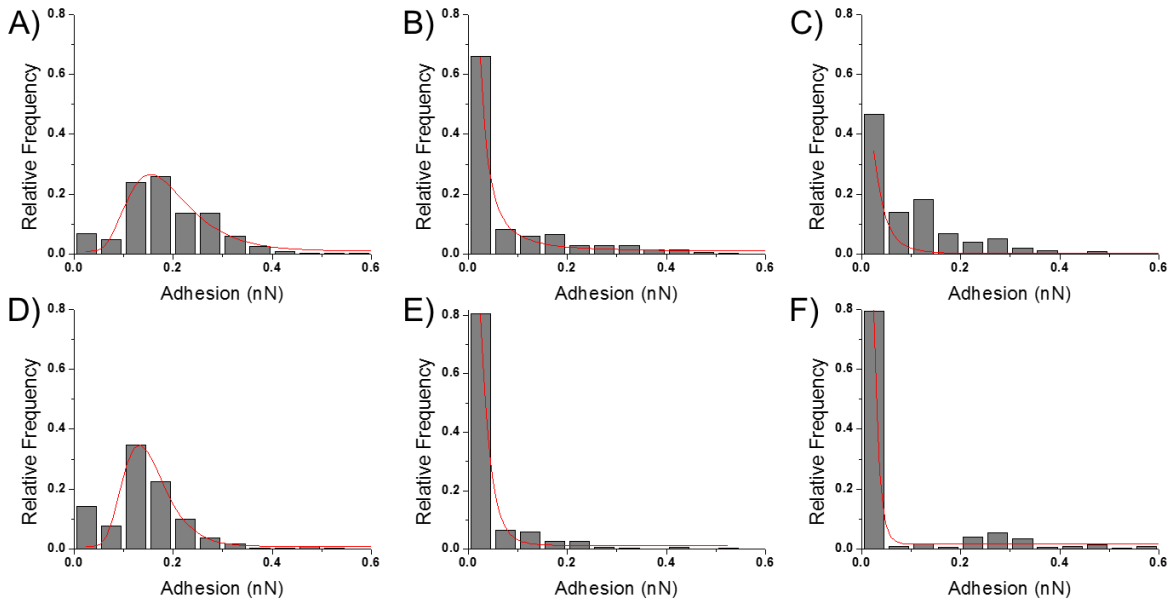

Figure 5.Adhesion forces of trypsin-EDTA treated cells were significant reduced. Histograms plotted relative frequency versus adhesion with Log-normal fits. Upper panel shows HUC-BC cells with (A) no treatment, (B) 6 min treatment, and (C) 8 min treatment and lower panel shows HUC-PC cells with (D) no treatment, (E) 6 min treatment, and (F) 8 min treatment. For each condition, 25 cells were measured with ten force curves. The adhesion forces of all trypsin-EDTA treated cells were significantly different from the corresponding control group ($p<0.05$).

The adhesion forces were measured and analyzed the same as stiffness: HUC-BC cells with untreated control, 6 min trypsin-EDTA treatment, and 8 min trypsin-EDTA treatment and HUC-PC cells with untreated control, 6 min trypsin-EDTA treatment, and 8 min trypsin-EDTA treatment (Figure 5 (A)-(E)). In both cell lines, untreated control groups showed highest adhesion forces; HUC-BC control has an average with standard deviation of 0.19 ± 0.10nN (A) and HUC-PC control has 0.17 ± 0.18 nN (D). The trypsin-EDTA treated groups showed smaller adhesion forces; HUC-BC with 6 min trypsin-EDTA treatment has an average with standard deviation of 0.068 ± 0.123nN (B), HUC-BC with 8 min trypsin-EDTA treatment has 0.09 ± 0.11nN (C), HUC-PC with 6 min trypsin-EDTA treatment has 0.03 ± 0.07nN (E), and HUC-PC with 8 min trypsin-EDTA treatment has 0.06 ± 0.12nN (F). The adhesion forces of all trypsin-EDTA treated cells were significantly lower than each corresponding control group ($p<0.05$). When the cells were treated with atrypsin-EDTA solution, the most dominant peaks were located less than 50 pN.

Log-normal fitting average; HUC-BC control has an average with astandard deviation of 0.180 ± 0.008 nN (A) and HUC-PC control has 0.145 ± 0.005 nN (D). The trypsin-EDTA treated groups showed smaller adhesion forces; HUC-BC with 6 min trypsin-EDTA treatment has an average with standard deviation of 0.001 ± 0.02 nN (B), HUC-BC with 8 min trypsin-EDTA treatment has 0.03 ± 0.16 nN (C), HUC-PC with 6 min trypsin-EDTA treatment has 0.02 ± 0.04 nN (E), and HUC-PC with 8 min trypsin-EDTA treatment has 0.02 ± 1 nN (F).

Morphology of cells is not changed by a trypsin-EDTA treatment or cytospin

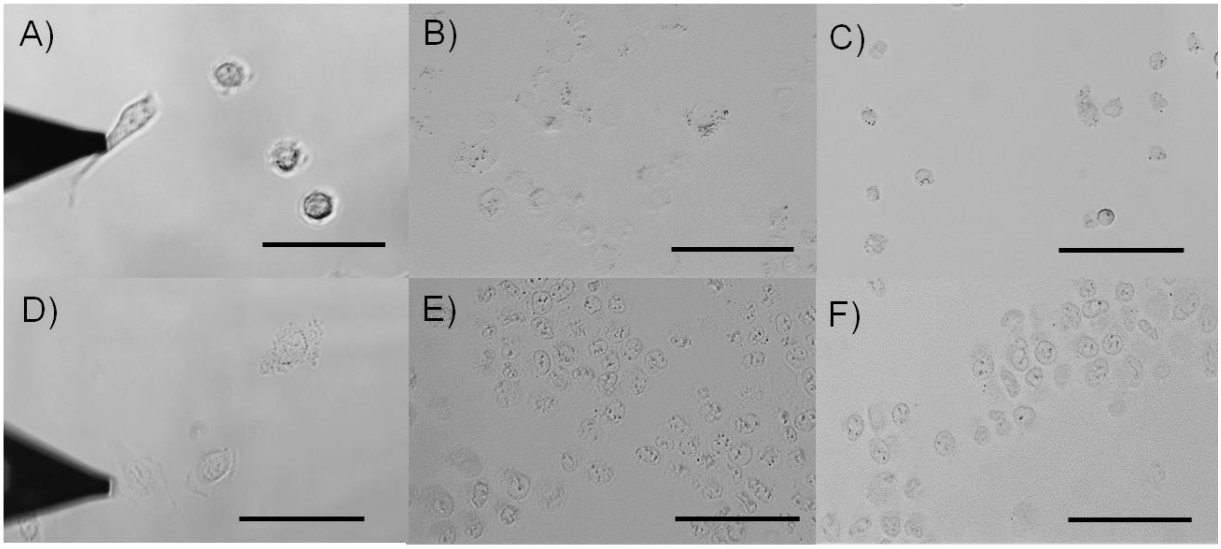

Figure 6. The bright field images of cells show no apparent differences by trypsin-EDTA treatment. Upper panel shows HUC-BC cells with (A) no treatment, (B) 6 min treatment, and (C) 8 min treatment and lower panel shows HUC-PC cells with (D) no treatment, (E) 6 min treatment, and (F) 8 min treatment (scale bar 100 um). The black triangle in (A) and (D) is AFM MLCT cantilever.

We confirmed that the morphology of cell nucleus regions is not changed by either a trypsin-EDTA treatment or cytospin. The population of cells are increasing as we cytospun cells in a confined area. The filophodia of cells are retracted after a typsin-EDTA treatment and cytospin. The region of interest, cell nucleus, remains the same.

4.5 Conclusions

We have investigated the stiffness of cells with different metastatic potentials. The benign cells, HUC-BC and HUC-PC were stiffer than the malignant cell, MC-T11.HUC-BC and HUC-PC have different susceptibility to 4-ABP, a carcinogen. We could observe HUC-BC, an untranformable cell line, is stiffer than HUC-PC, a transformable cell line, even before transformation by 4-ABP. We tested the effects of a trypsin-EDTA to HUC-BC and HUC-PC. Both cell lines were softer when treated with trypsin-EDTA and HUC-BC cells showed treatment time dependent changes in Young's modulus values. In addition, both cell lines conveyed lower adhesion forces after a trypsin-EDTA treatment. This would provide the basic mechanical information of cells. It is notable that the mechanics of cells are altered while the morphology of the cells are not.

4.6 References

1. Carvalho, F.A. and N.C. Santos, *Atomic force microscopy-based force spectroscopy--biological and biomedical applications.* IUBMB Life, 2012. **64**(6): p. 465-72.
2. Dufrene, Y.F., *Recent progress in the application of atomic force microscopy imaging and force spectroscopy to microbiology.* Curr Opin Microbiol, 2003. **6**(3): p. 317-23.
3. Clausen-Schaumann, H., et al., *Force spectroscopy with single bio-molecules.* Current Opinion in Chemical Biology, 2000. **4**(5): p. 524-530.
4. Lekka, M., et al., *Cancer cell detection in tissue sections using AFM.* Archives of Biochemistry and Biophysics, 2012. **518**(2): p. 151-156.
5. Lekka, M., et al., *Cancer cell recognition - Mechanical phenotype.* Micron, 2012. **43**(12): p. 1259-1266.
6. Cross, S.E., et al., *AFM-based analysis of human metastatic cancer cells.* Nanotechnology, 2008. **19**(38).
7. Cross, S.E., et al., *Nanomechanical analysis of cells from cancer patients.* Nature Nanotechnology, 2007. **2**(12): p. 780-783.
8. Ghoneum, A., et al., *Biophysical and morphological effects of nanodiamond/nanoplatinum solution (DPV576) on metastatic murine breast cancer cells in vitro.* Nanotechnology, 2014. **25**(46): p. 465101.
9. Sharma, S., et al., *Correlative nanomechanical profiling with super-resolution F-actin imaging reveals novel insights into mechanisms of cisplatin resistance in ovarian cancer cells.* Nanomedicine-Nanotechnology Biology and Medicine, 2012. **8**(5): p. 757-766.
10. Sharma, S., et al., *The role of Rho GTPase in cell stiffness and cisplatin resistance in ovarian cancer cells.* Integr Biol (Camb), 2014. **6**(6): p. 611-7.

11. Leckband, D. and A. Prakasam, *Mechanism and dynamics of cadherin adhesion.* Annu Rev Biomed Eng, 2006. **8**: p. 259-87.

12. Oberleithner, H., et al., *Potassium softens vascular endothelium and increases nitric oxide release.* Proceedings of the National Academy of Sciences of the United States of America, 2009. **106**(8): p. 2829-2834.

13. Rao, J.Y., G.P. Hemstreet, and R.E. Hurst, *Molecular Pathology and Biomarkers of Bladder Cancer*. Molecular Pathology of Early Cancer, ed. S. Srivastava, D.E. Henson, and A.F. Gazdar. 1999, Amsterdam: IOS Press.

14. Rao, J.Y., et al., *Quantitative changes in cytoskeletal and nuclear actins during cellular transformation.* Int J Cancer, 1997. **70**(4): p. 423-9.

15. Bookland, E.A., et al., *Tumorigenic transformation and neoplastic progression of human uroepithelial cells after exposure in vitro to 4-aminobiphenyl or its metabolites.* Cancer Research, 1992. **52**(6): p. 1606-14.

Chapter 5.

Nanoscale Characterization of Effect of L-Arginine on *Streptococcus Mutans* Biofilm Adhesion by Atomic Force Microscopy

5.1 Abstract

A major etiological factor of dental caries is the pathology of the dental plaque biofilms. The amino acid L-arginine is found naturally in saliva as a free molecule or as a part of salivary peptides and proteins. Plaque bacteria metabolize L-arginine to produce alkali and neutralize glycolytic acids, promoting a less cariogenous oral microbiome. Here, we explored an alternative and complementary mechanism of action of L-arginine using atomic force microscopy (AFM). The nanomechanical property of *S. mutans* biofilm extracellular matrix was characterized under physiological buffer conditions. We report the effect of the ingredient L-arginine (Arg) on the adhesive behavior and structural properties of extracellular polysaccharides in *S. mutans* biofilms. High resolution imaging of biofilm surfaces, reveal additional structural information on bacterial cells embedded within the surrounding extracellular matrix. A dense extracellular matrix was observed in biofilms without Arg compared to those grown in presence of Arg. *S. mutans* biofilms grown in the presence of Arg could influence the production and/or composition of extracellular membrane glucans and thereby affect their adhesion properties. Our results suggest that the presence of Arg in the oral cavity could influence the adhesion properties of *S. mutans* to the tooth surface.

5.2 Introduction

Dental caries is the most prevalent and costly oral infectious disease worldwide [1]. One of the main etiological factors of caries is the pathology of the dental plaque biofilm [2]. The bacterial biofilm consists of both acidogenic and arginolytic strains [3]. Microbial species in the acidogenic genera, specifically *S. mutans* [4], have been proposed as specific agents of the acid production that is principal to the dental caries process. These cariogenic organisms metabolize dietary fermentable carbohydrates to form organic acids as end products [4]. Acid production causes a local drop in pH and it is the proximity of these acidogenic bacteria to the tooth surface and the contact of the acid with the surface that eventually causes the breakdown of enamel or demineralization.

Enamel, the outer layer of the tooth, is composed of calcium and phosphate mainly in the form of hydroxyapaptite [3]. Dental caries is a dynamic process. The cariogenic organisms generate acids that diffuse into enamel, dissolving mineral crystals in their path. As the pH of the plaque increases (as a result of the saliva's buffering capacity or ammonia production from arginolytic and/or ureolytic plaque bacteria), the environment becomes supersaturated in calcium and phosphate leading to tooth remineralization. This process of demineralization and remineralization occurs frequently throughout the day. Cavities form when the tooth environment stays longer under demineralizing (net mineral loss) versus remineralizing (net mineral gain) conditions [3].

Therefore the etiology of this disease is very dependent on the ecology of the plaque microbiome, salivary composition and flow rate, and frequency of carbohydrates consumed [5].

Plaque is derived from salivary planktonic bacteria that form multi-cellular communities via cell–cell and cell–surface interactions. These bacteria colonize on oral surfaces, by binding to surface specific binding sites on proteins.There have been over 1000 bacteria species detected within the oral environment many of which remain un-culturable [6]. Of these species, both healthy and potentially pathogenic strains exist. When the microbiome is balanced, the oral environment can maintain its healthy existence. However, when conditions change to favor the growth of cariogenic organisms, there is an increased risk of cavity formation [7].

Like other cariogenic bacteria, *S. mutans*, not only metabolizes carbohydrates, but it has evolved multiple mechanisms to survive under acidic, low pH conditions [8]. *Streptococcus mutans*, also has the ability to synthesize extracellular glucans from sucrose using glucosyltransferases (Gtfs) which is a major virulence factor [9]. The insoluble glucans synthesized by Gtfs provide specific binding sites for bacterial colonization on the tooth surface and to each other, modulating the formation of tightly adherent biofilms [10-11]. In addition, the secreted extracellular polysaccharides (EPS) provide stability, structural integrity, and resistance to bacteria from antimicrobials and other chemicals [12].

Several technologies have been developed that specifically target and minimize the acid producing effects of *S. mutans* [13-15]. These approaches have been proven to enhance the remineralization process resulting in the arrest and reversal of caries lesions. Other anti-cavity approaches to arrest caries initiation and progression by promoting a more alkaline generating microbiome, have also been suggested recently [16-17]. When plaque pH is elevated above the pH, which maintains the supersaturated conditions of calcium and phosphate, remineralization

will be favored. In fact, populations who are able to generate higher ammonia concentrations have been shown to be at lower risk of cavity formation [18]. Thus, shifting the oral microbiome to a healthier, less cariogenic population is an evolving concept being studied to manage the caries process [16-17].

One such approach to promote a less cariogenous microbiome is through the use of the amino acid L-arginine (Arg), which is known for its anti-caries effect [19]. In fact, a recent publication has demonstrated that the use of a dentifrice containing L-arginine and an insoluble calcium compound and fluoride provides superior efficacy in preventing enamel demineralization, enhancing remineralization and producing a more basic plaque biofilm vs a placebo control containing no Arg [20]. Arginolytic organisms in the oral cavity catabolize Arg through an internal cellular pathway called the Arginine Deiminase System [21]. When Arg is utilized, the pathway yields ammonia as an end product. Ammonia, the final metabolic product, neutralizes organic acids produced within the oral cavity [21].

Although the biochemical characteristics of *S. mutans* have been studied [8], the biofilm extracellular matrix (EM) organization has not been investigated quantitatively under physiological conditions at high resolution in the presence and absence of Arg. In this study, we used atomic force microscopy (AFM) [22] based nanomechanical characterization of *S. mutans* biofilm extracellular matrix under physiological buffer conditions. *S. mutans* bacterial biofilms grown in growth media containing Arg and sucrose were studied. The findings provide nanomechanical evidence for the effect of Arg on the adhesive behavior and structural properties of extracellular polysaccharides in *S. mutans* biofilms. Our results suggest that *S. mutans*

biofilms grown in the presence of Arg could influence the production and/or composition of extracellular membrane glucans and thereby affect their adhesion properties. High resolution imaging of biofilm surfaces reveal structural information on bacterial cells embedded within the surrounding extracellular matrix. A dense extracellular matrix was observed in biofilms without Arg compared to those grown in presence of Arg. Our results suggest that the presence of Arg in the oral cavity could influence the adhesion properties of *S. mutans* to the tooth surface.

5.3 Materials and Methods

Growth of *In Vitro* Biofilms: Overnight cultures (OD 600nm=1) of *S. mutans* strain UA140 [23] grown at 37°C in 5% CO_2 atmosphere were diluted 1:100 in fresh Todd-Hewitt (TH, Difco) medium containing 1% (wt/vol) sucrose, 1% mannose and 1% glucose as the supplementary carbon and energy source. Additionally, Arg or glycine (both purchased from Sigma-Aldrich) was added at different concentrations to the media. No Arg or glycine was added to control samples. Five hundred microliters (500 μL) of diluted culture was added to each well of six-well polystyrene microtiter plates in which sterile coverslips had been placed. After overnight *S. mutans* biofilm formation, the plates were rinsed with Phosphate Buffered Saline (PBS) three times to remove planktonic and loosely bound cells. Biofilm adhesion was measured via AFM under PBS, pH 7.2 at room temperature (20°C). The pH in the different biofilms was determined by using standard pH microelectrodes (Fischer Scientific) following previously described methods [24].

AFM: All force measurements in fluid were conducted using a Nanoscope V Catalyst (Bruker Corp.) mounted on an inverted optical Zeiss Microscope. AFM measurements were collected in contact mode using sharpened silicon nitride cantilevers (MLCT, Bruker Corp.) with experimentally determined spring constants of 0.01 N/m and a nominal tip radius of 20 nm as defined by the manufacturer (Bruker Corp.). Before obtaining force measurements, the surface attachment and stability of bacterial biofilm was tested by imaging the surfaces at low forces (~ 200pN). Force–distance measurements were collected on *S. mutans* biofilms by lowering the cantilever tip toward the cell, pressing against the cell surface and retracting the tip from the cell as shown schematically in Figure 1. The resulting curves, generated from the cantilever

displacement, were analyzed to reveal the force magnitude and relative cell surface adhesion by monitoring the rupture events revealed in the associated tip retraction traces from the cell surface as shown in Figure 1 (c-d). About 100 force-distance curves were obtained at ten different biofilm regions for each growth condition using z ramp size of 18 μm and 1 Hz at 1024 x 1024 samples/line. The adhesion forces and rupture lengths were calculated from force-distance curves using SPIP™ software.

AFM Imaging: Biofilm samples were briefly rinsed with PBS and water and imaged under ambient conditions using tapping mode AFM imaging. To obtain structural characteristics of biofilm surfaces, the height, deflection and phase images were simultaneously acquired as they yield complementary information. Images were recorded at 1024 samples per line at 1Hz using TESP (Bruker Corp.) probes. Image processing was done using SPIP™ software.

5.4 Results

Influence of L-Arginine on Adhesive Properties of *S. Mutans* Biofilms Measured By AFM

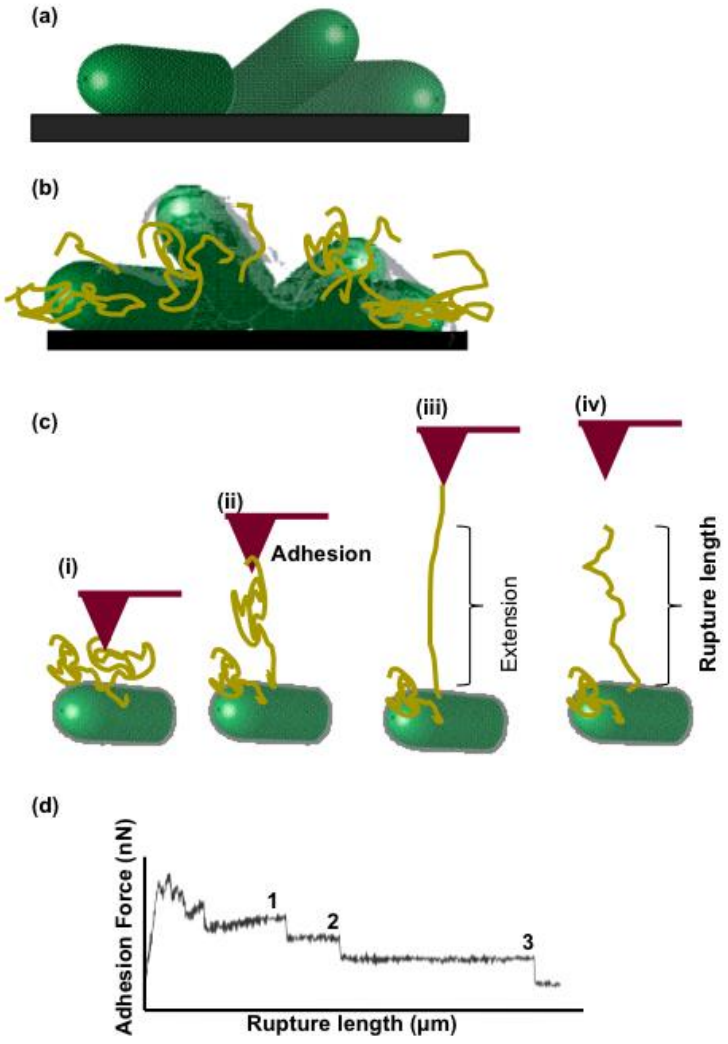

Figure 1. Schematics of AFM based *S. mutans* biofilm adhesion and rupture length analysis. (a) *S. mutans* biofilm grown over glass substrates (b) *S. mutans* biofilm with bacterial cells and secreted extracellular matrix and polysaccharides (c) A typical force-distance cycle over biofilm surface (i) AFM tip pushing on biofilm bacteria surrounded by polysaccharide matrix (ii) Polysaccharides (potentially of different lengths) attach to the tip and are pulled upwards (iii) long polymeric chains that bind to the AFM tip, extend as they are pulled away from bacterial surface (iv) As the tip moves further away from the surface, the bonds break, resulting in rupture events of varying lengths (d) Illustration of AFM tip and bacterial biofilm adhesion forces and rupture events (1-3) at different lengths away from the bacterial biofilm surface.

We used AFM to measure the adhesion properties of the *S. mutans* biofilm surfaces at the nano-scale. *S. mutans* biofilms were immobilized by growing them on glass cover slips as described above. The force–displacement curves were measured on the bacterial biofilm by lowering the tip and pressing it against the cell surface with a maximum force of ~5nN. Upon tip retraction, a sequence of rupture events occurred at distances of up to 18 μm, presumably arising from the breakage of multiple adhesions between the AFM tip and the biofilm surface (Figure 1). A typical cycle of bond formation and subsequent rupture at varying distances away from the biofilm surface is shown in Figure 1.

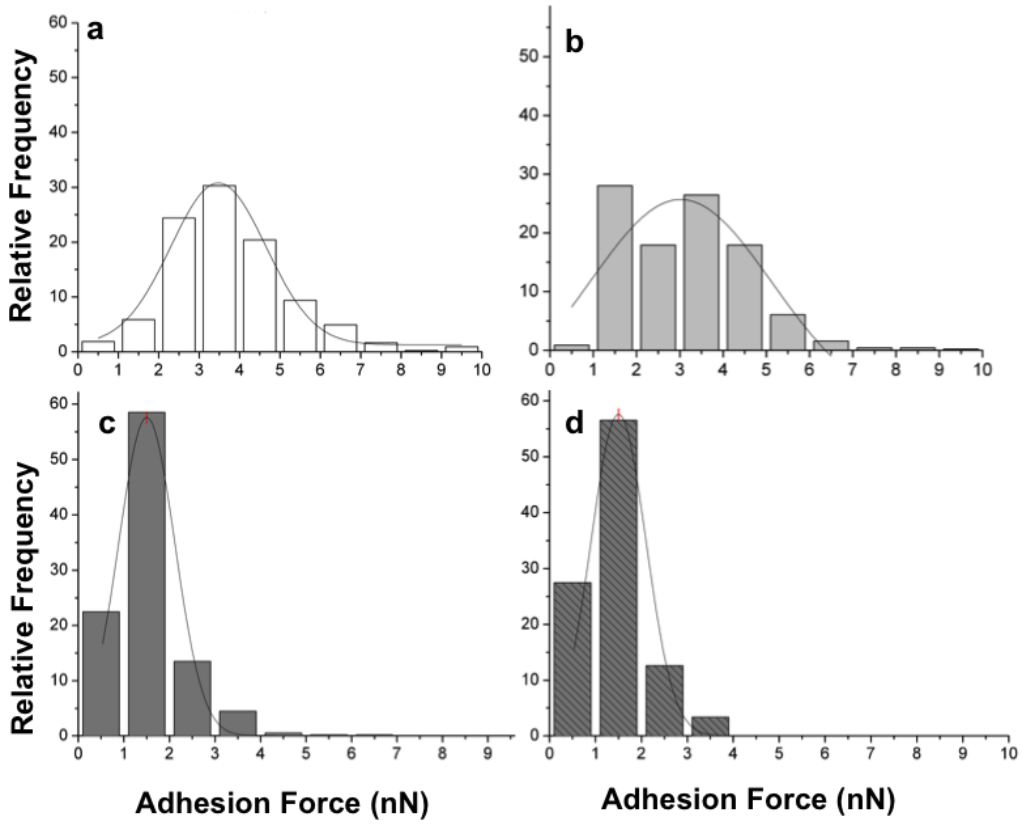

Figure 2. Adhesion force characteristics of 24 hrs *S. Mutans* biofilm without and with L-arginine (Arg) measured by AFM force spectroscopy. (a) In absence of Arg (b) with 0.5 mg/ml Arg (c) with 1 mg/ml Arg and (d) 5 mg/ml Arg. The data presented here are representative of three independent experiments. All AFM measurements were obtained under PBS (pH 7.2).

The observed adhesion forces of *S. mutans* biofilm grown in media containing different concentrations of Arg are shown in Figure 2. In the absence of Arg, the adhesion forces were broadly dispersed with a mean adhesion force of 3.5 ± 0.6 nN (Figure 2(a)). As the amount of Arg was increased, the frequency of rupture events shifted to lower adhesion forces. Adhesion forces (Mean ± s.d.) for *S. mutans* biofilms grown under 0.5 mg/ml, 1 mg/ml, and 5 mg/ml of Arg were measured to be 3.1 ± 2.4 nN, 1. 4± 0.7 nN, and 1.3 ± 0.6 nN, respectively. In the presence of 1 mg/ml Arg and above, the adhesion forces were significantly reduced (Student's T-Test; $P<0.05$) and principally clustered at less than 2 nN.

Changes in Rupture Tip-Cell Retraction Lengths of *S. Mutans* Biofilms in The Presence of L-Arginine

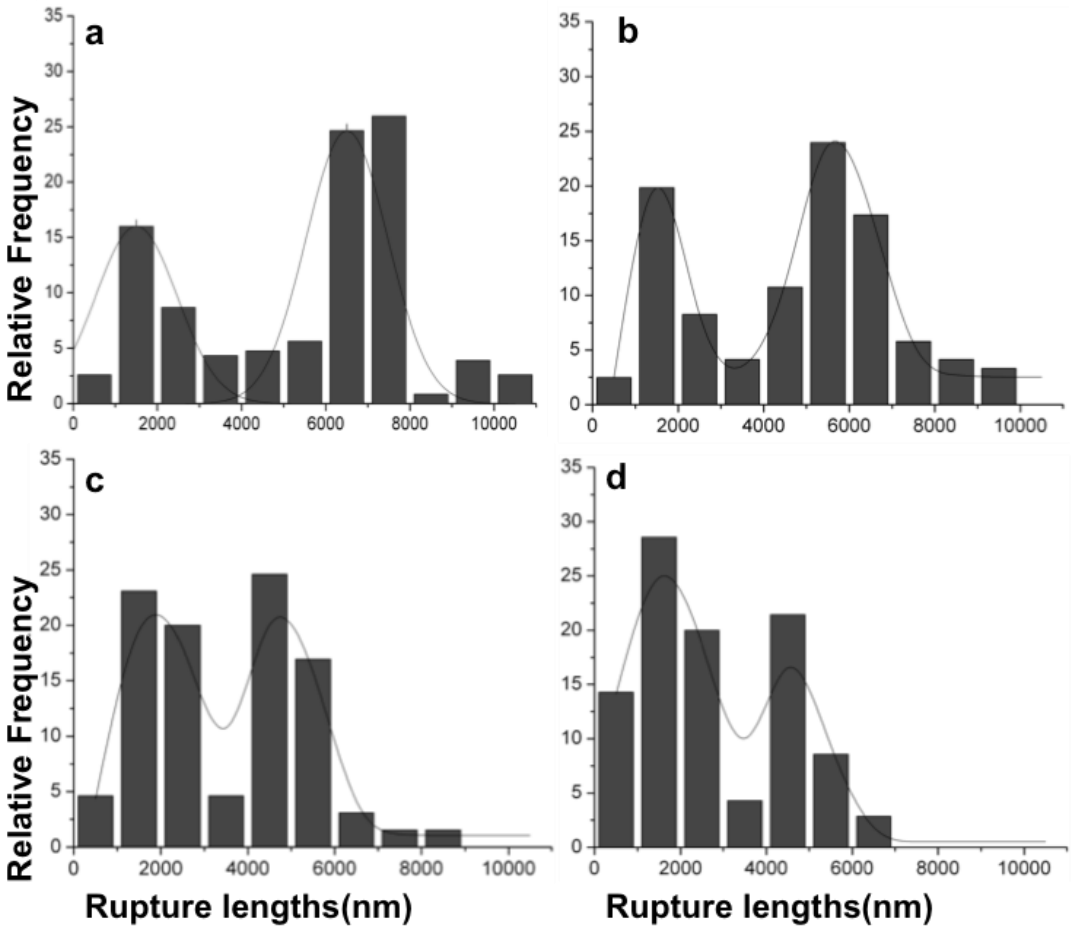

Figure 3. Rupture lengths (in nm) for biofilms grown under culture media containing (a) No Arg (b) 0.5 mg/ml Arg (c) 1 mg/ml Arg and (d) 5 mg/ml of Arg were measured from AFM force-separation curves. Histograms show reduction in the rupture lengths, with bimodal peaks shifting towards shorter events with increasing concentrations of Arg.

The corresponding tip-cell distance before rupture for biofilms grown under varying Arg conditions, measured from the AFM force-separation curves are shown in Figure 3. As the concentration of Arg increased in the growth media, the distance that the tip retracts before contact is lost (i.e., "rupture lengths") is decreased. Rupture lengths (Mean ± s.d.) for *S. mutans* biofilms grown under 0 mg/ml, 0.5mg/ml, 1mg/ml and 5mg/ml of L-arginine were measured. The histogram of rupture lengths displayed a bimodal population (Figure 3) with two main peaks. When no Arg is present, about 50% of the ruptures occur at distances 6000 to 8000 nm away from the biofilm surfaces (peak 2) while another shorter population (peak 1) (15%) is observed closer (<2000 nm) to the biofilm surface. The average mean rupture length values for peak 1 and peak 2 for control biofilms were measured to be 1400 ± 800 nm and 6500 ± 100 nm respectively. However, longer rupture length populations (peak 2) show a gradual and significant reduction upon treatment with Arg. The average rupture lengths for 0.5 mg/ml Arg obtained were 1500 ± 100 nm (peak 1) and 5900 ± 100 nm (peak 2). In case of 1 mg/ml and 5 mg/ml the rupture lengths were measured to be 1600 ± 100 nm (peak 1) and 4800 ± 200 nm (peak 2) and 1500 ± 100 nm (peak 1) and 4500 ± 200 nm (peak 2) respectively. (* $P<0.05$, ** $P<0.005$ compared to control biofilms).

To test whether the reduced adhesion forces are influenced by the presence of another amino acid, we grew the biofilm in the presence of glycine. Glycine did not impede the adhesive interactions and rupture lengths of biofilms. *S. mutans* biofilms cultured in growth media containing glycine showed both the adhesion forces and rupture lengths comparable to control (no Arg). The mean adhesion force for 1 mg/ml and 5 mg/ml of glycine were observed to be 3.7 ± 1.4 nN and 3.8 ± 1.8 nN (Mean ± s.d.) respectively, similar to control biofilms. Additionally,

in case of 1 mg/ml and 5 mg/ml glycine, the rupture lengths were measured to be 1900 ± 100 nm (peak 1) and 5800 ± 200 nm (peak 2) and 1500 ± 500 nm (peak 1) and 5700 ± 200 nm (peak 2) respectively ($P>0.05$ compared to control biofilms).

Biofilm Viability

The topography of the biofilms was similar under both conditions. Experiments were also conducted to determine if there was any reduction in colony forming units as a result of arginine being present in the growth media. No evidence of growth inhibition was observed. (Figure S1)

Ultra-structure of *S. Mutans* Biofilms Imaged Using AFM

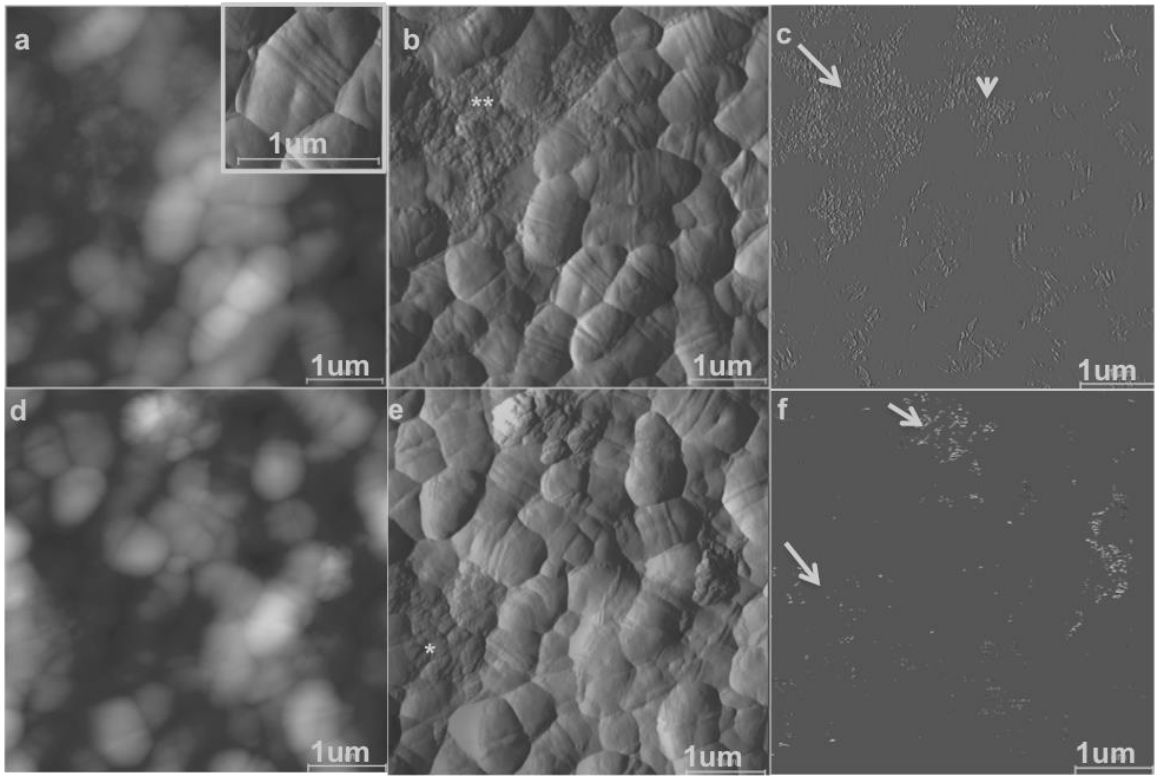

Figure 4. AFM images showing differences in ultra-structure of *S. mutans* untreated (a, b, c) and 1mg/ml arginine treated (d, e, f) biofilms. (a,d) Topography, (b,e) amplitude and (c,f) phase images of biofilms grown in absence and presence of L-arginine (Arg) respectively. The structure of individual bacterial cell is shown in inset in (a). The secreted EPS around the bacterial cells is marked with asterisks (*) in amplitude images. The corresponding phase images (c,f) show enhanced contrast in regions of extracellular matrix marked with arrows. In the presence of Arg, the extracellular matrix is less abundant compared to control biofilms.

To further evaluate the quantitative changes in surface adhesion forces and rupture lengths for *S. mutans* biofilms observed in the presence of Arg, we used AFM tapping mode imaging under ambient conditions to observe the ultrastructure and distribution of the EPS materials of these biofilms. Individual *S mutans* cells showed characteristic elongated shapes with length, width, and height dimensions approximately 1 μm, 0.5 μm, and 0.4 μm respectively as reported previously [25]. *S. mutans* strain UA140 cells showed two parallel bands typical in their nanoscale surface topology (Figure 4). Figure 4(a) shows a topographical image of *S. mutans* control biofilms. AFM images reveal the presence of EPS materials around the bacterial cells that form a mesh-like network of surrounding extracellular matrix (Figure 5 (a)(b)). Interestingly, AFM images obtained for *S. mutans* biofilms grown in the presence and absence of Arg showed differences in the abundance and localization of the extracellular matrix, as shown in representative AFM amplitude images (Figure 4 (b)(e) and Figure S2). There was also a notable decrease in the surface roughness of biofilms grown in presence of Arg. In the presence of Arg, the extracellular matrix is less dense compared to control biofilms. The observed changes in the biofilm matrix were more clearly visualized in the phase images (Figure 4 (c)(f)). The biofilm EPS shows characteristic phase contrast (Figure 4 (c)(f)), suggesting the role of heterogeneous density and/or viscoelastic properties of the matrix compared to bacterial structures.

5.5 Discussion

AFM has rapidly evolved into a tool that can quantitatively probe bio-molecules as well as bacterial and biofilm surface interactions [25-28]. The composition and structure of the *S. mutans* extracellular matrix varies as a function of environmental conditions [29]. It mainly consists of polysaccharides, proteins, lipids, and nucleic acids [30]. It has been suggested that the EPS materials may play a major role in the organization and cohesion of bacterial biofilm [31]. AFM based force spectroscopy has been used successfully to measure and quantify other biopolymers such as DNA, proteins and polysaccharides [32-33]. Bacterial adhesion is of interest to understand the bacterial infection mechanisms including dental caries, AFM force spectroscopy allowed measuring the adhesive forces between the tip and the bacteria. One of the early studies showed the adhesive forces between the cantilever tip and *E. coli* mutants using AFM [34]. Various efforts were made to measure adhesive forces of bacteria [35-38]. The adhesion forces of *S. mutans* were measured to reveal the role of *S. mutans* in dental caries [39-42]. In this study, we used AFM to characterize the adhesive properties of *S. mutans* biofilms by probing the adhesive forces between the biofilm and AFM tip as well as the lengths of the rupture events that occur at varying distances away from the biofilm surface as the AFM tip is pulled away from the surface.

The significant reduction in biofilm adhesion forces observed in the presence of Arg suggests potential changes in the *S. mutans* biofilm surface resulting in reduced hydrogen bonding interactions. Such an effect may occur due to less glucan being produced, as was shown to affect the adherence properties of *S. mutans* [8]. Since Arg is not metabolized by non-arginolytic bacteria strains, it may itself inhibit the interactions between glucan sites. The biofilms showed

no significant change in pH values at time zero and after 24 hours of incubation (Table S1) for the cultures grown in 1 mg/ml arginine or less. Hence, the pH effect is unlikely to result in the observed reduction in adhesion forces of the arginine treated biofilms. Additionally, we found no evidence of a reduction in *S. mutans* biofilm viability due to the presence of Arg (Figure S1). Robust biofilms were observed up to 5 mg/ml Arg concentrations.

Additionally, the reduction in the measured rupture lengths of the unbinding events from AFM force-separation curves, possibly result from changes in the density and adhesiveness of the extracellular matrix surrounding the bacterial cells with the biofilm. All of these results are again consistent with less glucans being produced or less hydrogen bond interactions formed within the biofilm extracellular matrix. Furthermore, no significant changes in the biofilm properties were observed in the presence of glycine. The effect of glycine was not specific to *S. mutans* biofilms. Studies were also conducted on *S. sanguinis* biofilms grown in the presence and absence of Arg (data not shown). Although the bacterial extracellular surface was not as adhesive as *S. mutans* biofilms, in the presence of Arg, there was a significant reduction in biofilm adhesion forces. *S. sanguinis* is an arginolytic bacteria that metabolizes Arg to produce ammonia. No such pathway exists utilizing arginine for *S. mutan*s [41].

AFM is also a powerful technique to probe biological surface structure and properties at the nanometer resolution [8, 28, 43-44] and can be used for high-resolution studies of EPS and biofilm surfaces. By employing high-resolution AFM images, we were able to detect the density variations in *S mutans* biofilm EPS. Our results indicate a change in the characteristics of the extracellular matrix of *S. mutans* biofilm formed in the presence of Arg and provide structural

evidence to the changes in nanomechanical profiles (adhesion and EPS unbinding events) of the biofilms reported in this study.

Within the human oral environment, the fate of any bacterium/biofilm is complex and depends on several associated factors. The physical properties, net charge, and hydrophobicity of the substrate surface can influence the composition of adherent bacteria and the efficiency of adsorption [40, 45]. Within the oral environment, the tooth surface is spontaneously covered by salivary secretion, which influences the maturation/conditioning of tooth enamel. The presence of saliva results in the deposition and incorporation of calcium, phosphates and fluoride into the maturing hydroxylapatite, due to the saturation of saliva with these ions. Additionally, the tooth is coated with the acquired enamel pellicle [46] which comprises glycoproteins and mucins, and can include cystatins, histatins, lysozyme, amylase, lactoferrin, lactoperoxidase, sialic acid, albumin, carbonic anhydrate, secretory IgA and bacteria-derived glucosyltransferases and fructosyltransferases from the surrounding saliva [47-48]. The pellicle protects the porous HA from demineralization of calcium and phosphates by plaque-generated acids. Many of the proteins, as well as water-insoluble glucan, adsorb to the tooth surface via primary colonizing bacteria that initiate plaque development. The results of this pilot study on *S. mutans* biofilms grown on unconditioned glass substrates, while encouraging, should be considered preliminary. Further studies are necessary to assess the extent and influence of Arg in preventing or reducing *S. mutans* biofilm adhesiveness on more physiologically relevant substrates such as HA and saliva-treated HA surfaces that better mimic oral microenvironments. Such an approach would use HA functionalized AFM probes with or without saliva coating to test the effectiveness of Arg in reducing changes in nanomechanical profiles (adhesion and EPS unbinding events) of

the initial-stage *S. mutans* biofilms.

In summary, our study provides continued evidence that AFM can be used to measure and quantify the interactions between cell surface materials present on bacteria membranes. Specifically, this report highlights the ability to measure adhesive interactions of membrane bound species from *S. mutans* biofilm. The interactions are thought to originate between glucan polymers and membrane bound proteins. Our results suggest that the presence of Arg in the oral cavity could modulate the adhesion properties of *S. mutans* to the tooth surface and may possess anti-cariogenic potential.

5.6 An Extension to Clinical Studies

To extend these promising results to a clinical stage, we are in collaboration with Colgate (Colgate-Palmolive, NY, USA) to test human plaque samples. Unlike biofilms generated from bacterial cells, human plaque samples are more heterogeneous. Thus, the sample preparation with a standardized protocol is a key for successful clinical trials. To optimize the sample preparation, two types of human plaque samples were tested for four patients; one is in fluid form where the plaques were collected with a cotton swab then dissolved in PBS (form A) and the other is in solid form that plaques collected in a micro-centrifuge tube directly from a plaque scrapper (form B). In case of biofilms, they were anchored to surfaces while bacterial cells are growing. However, plaque samples were needed to be attached to a surface before measuring their adhesion forces or rupture lengths. We prepared poly-lysine coated cover slides to immobilize the plaque sample and both samples were incubated on poly-lysine coated cover slides. For form A, the plaque samples in PBS were incubated for 10 min then gently washed with PBS to remove unbound plaques and 100 μL of PBS is added before the AFM measurement. The solid plaques (form B) were taken from each micro-centrifuge tube, smeared on to the dry poly-lysine coated cover slides, and incubated for 10 min, and then 100 μL of PBS is added before the AFM measurement. We have tested both wet and dry plaques to test the differences in adhesion forces and rupture lengths depending on the sample preparation method if exist. Figure 5 and 6 summarize the initial result with human plaque samples.

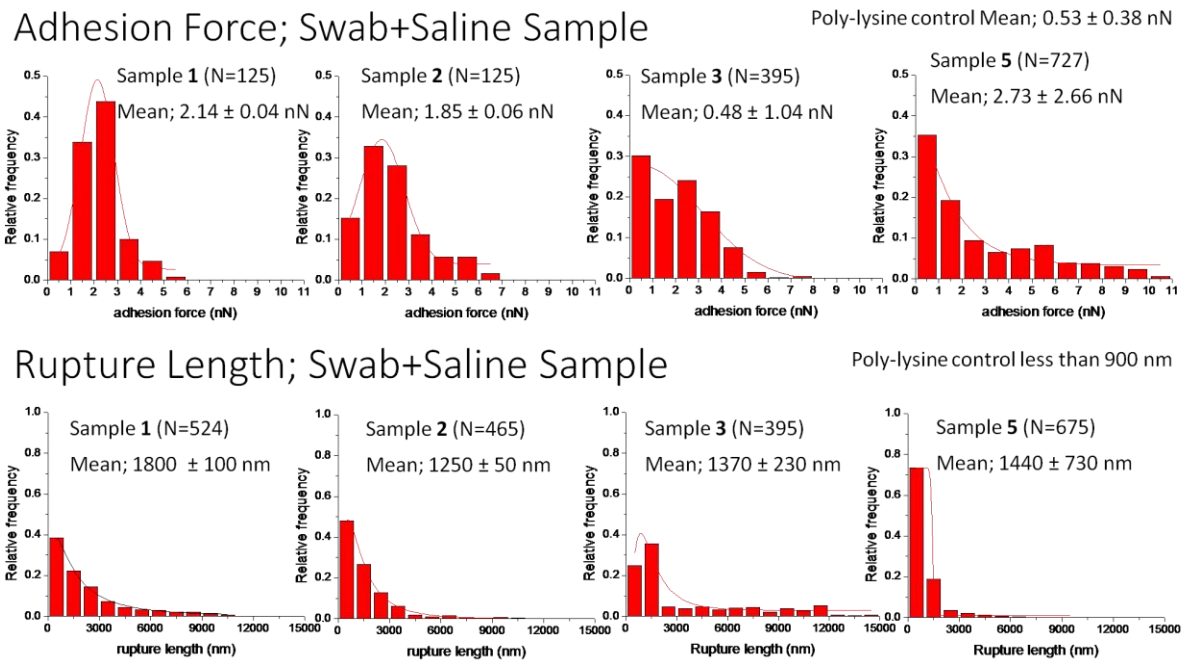

Figure 5. The adhesion force and rupture length from the plaque samples dissolved in PBS.

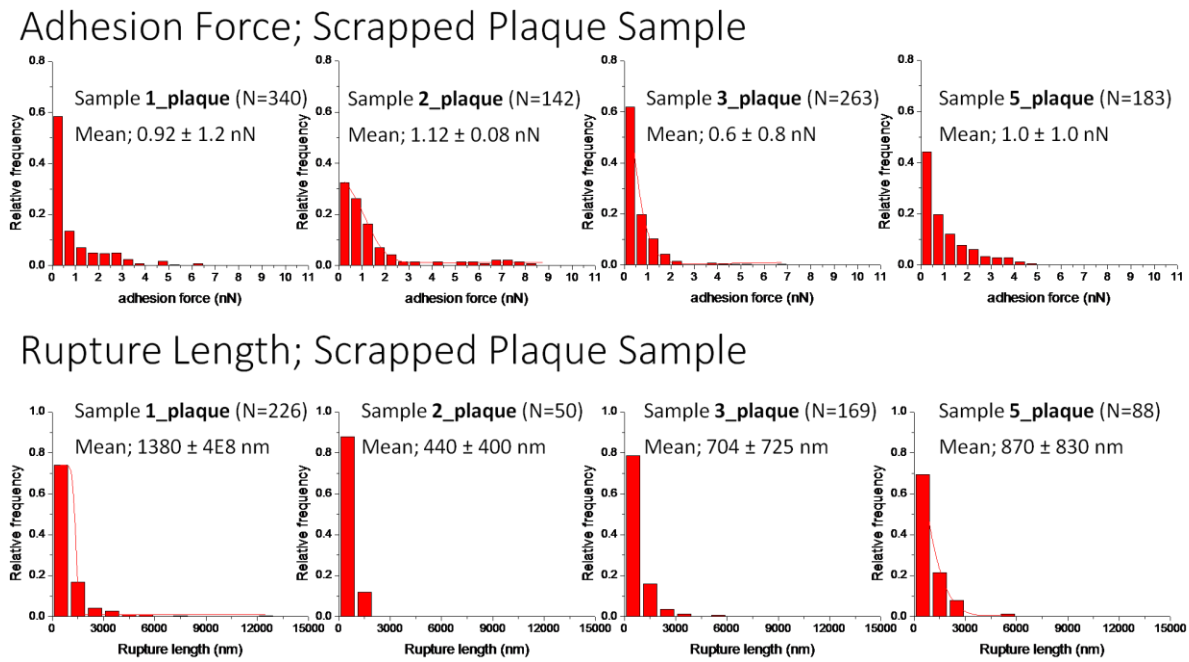

Figure 6. The adhesion force and rupture length from the smeared dry plaque samples.

We have measured the adhesion force and rupture length from human plaque samples and tested two sample forms. Sample form A was selected as we can control plaque quantitatively. Based on this initial result, we will conduct experiments to observe changes in adhesion force and rupture length after 3 month treatment of Arg containing toothpaste.

5.7 Supplementary Information

	pH at 0 hrs	pH at 24 hrs
No Arginine	7.68	4.87
0.5 mg/ml Arginine	7.92	4.96
1 mg/ml Arginine	8.17	5.07

Table S1. Bacterial growth media pH changes measured after 24 hr growth. Data shows no significant changes in the pH of 24 hr biofilm for control, and 0.5 and 1mg/ml Arg presence in media.

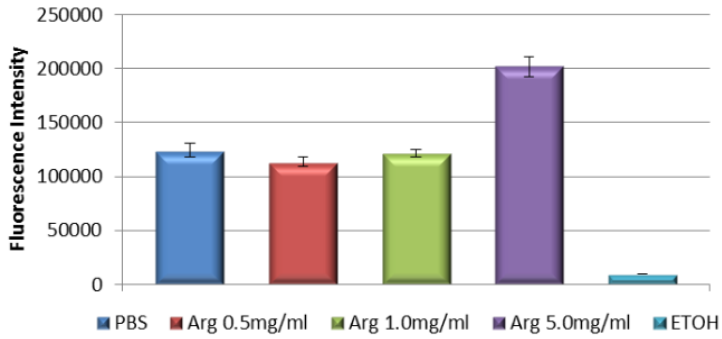

Figure S1. Bacterial cell viability assays with different Arg concentrations. Resazurin (7-Hydroxy-3H-phenoxazin-3-one 10-oxide) is a pH sensitive dye used as an oxidation-reduction indicator in cell viability assays for bacteria. Resazurin assay on *S. mutans* biofilm confirms that Arg does not kill *S. mutans*, thereby causing the reduction of adhesion via reduced glucan production (N=three different measurements).

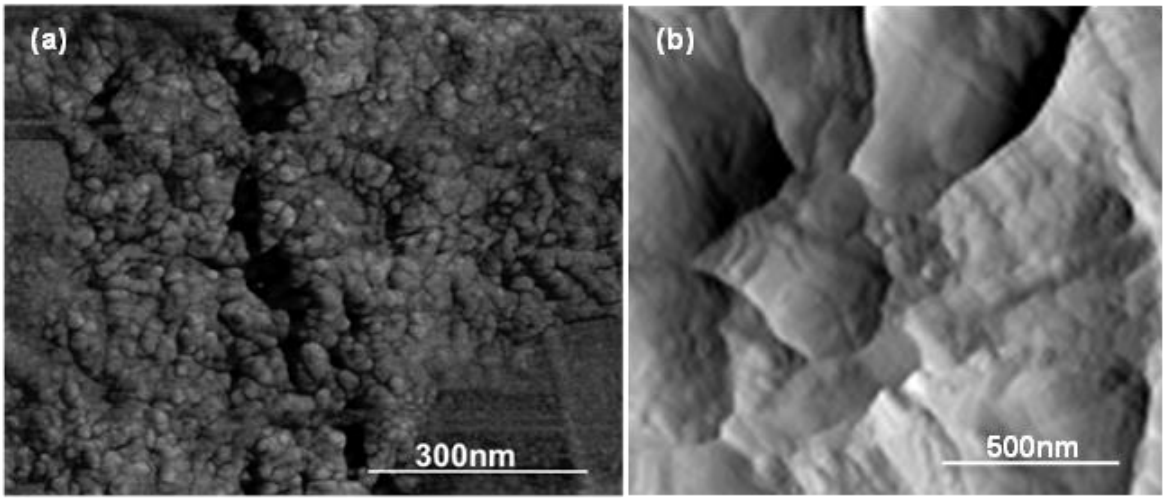

Figure S2. High resolution AFM amplitude images of *S. mutans* biofilm extracellular matrix (a) without any Arg, showing formation of mesh-like network between the bacterial cells, and (b) with 1 mg/ml Arg,

5.8 References

1. Jeon, J.G., et al., *Natural products in caries research: current (limited) knowledge, challenges and future perspective.* Caries Res, 2011. **45**(3): p. 243-63.
2. Marsh, P.D., *Dental plaque as a microbial biofilm.* Caries Res, 2004. **38**(3): p. 204-11.
3. Hicks, J., F. Garcia-Godoy, and C. Flaitz, *Biological factors in dental caries: role of saliva and dental plaque in the dynamic process of demineralization and remineralization (part 1).* J Clin Pediatr Dent, 2003. **28**(1): p. 47-52.
4. Loesche, W.J., *Role of Streptococcus mutans in human dental decay.* Microbiol Rev, 1986. **50**(4): p. 353-80.
5. Zero, D.T., et al., *The biology, prevention, diagnosis and treatment of dental caries: scientific advances in the United States.* J Am Dent Assoc, 2009. **140 Suppl 1**: p. 25S-34S.
6. Paster, B.J., et al., *Bacterial diversity in human subgingival plaque.* J Bacteriol, 2001. **183**(12): p. 3770-83.
7. Marsh, P.D., *Microbial ecology of dental plaque and its significance in health and disease.* Adv Dent Res, 1994. **8**(2): p. 263-71.
8. Cross, S.E., et al., *Nanomechanical properties of glucans and associated cell-surface adhesion of Streptococcus mutans probed by atomic force microscopy under in situ conditions.* Microbiology, 2007. **153**(Pt 9): p. 3124-32.
9. Yamashita, Y., et al., *Role of the Streptococcus mutans gtf genes in caries induction in the specific-pathogen-free rat model.* Infect Immun, 1993. **61**(9): p. 3811-7.

10. Xiao, J. and H. Koo, *Structural organization and dynamics of exopolysaccharide matrix and microcolonies formation by Streptococcus mutans in biofilms.* J Appl Microbiol, 2010. **108**(6): p. 2103-13.

11. Schilling, K.M. and W.H. Bowen, *Glucans synthesized in situ in experimental salivary pellicle function as specific binding sites for Streptococcus mutans.* Infect Immun, 1992. **60**(1): p. 284-95.

12. Paes Leme, A.F., et al., *The role of sucrose in cariogenic dental biofilm formation--new insight.* J Dent Res, 2006. **85**(10): p. 878-87.

13. Lang, C., et al., *Specific Lactobacillus/Mutans Streptococcus co-aggregation.* J Dent Res, 2010. **89**(2): p. 175-9.

14. Sullivan, R., et al., *Clinical efficacy of a specifically targeted antimicrobial peptide mouth rinse: targeted elimination of Streptococcus mutans and prevention of demineralization.* Caries Res, 2011. **45**(5): p. 415-28.

15. He, J., et al., *Systematic approach to optimizing specifically targeted antimicrobial peptides against Streptococcus mutans.* Antimicrob Agents Chemother, 2010. **54**(5): p. 2143-51.

16. Nascimento, M.M., et al., *Correlations of oral bacterial arginine and urea catabolism with caries experience.* Oral Microbiol Immunol, 2009. **24**(2): p. 89-95.

17. Morou-Bermudez, E., et al., *Urease activity in dental plaque and saliva of children during a three-year study period and its relationship with other caries risk factors.* Arch Oral Biol, 2011. **56**(11): p. 1282-9.

18. Nascimento, M.M., et al., *Oral Arginine Metabolism May Decrease the Risk for Dental Caries in Children.* Journal of Dental Research, 2013. **92**(7): p. 604-608.

19. Van Wuyckhuyse, B.C., et al., *Association of free arginine and lysine concentrations in human parotid saliva with caries experience.* J Dent Res, 1995. **74**(2): p. 686-90.

20. Cantore, R., et al., *In situ clinical effects of new dentifrices containing 1.5% arginine and fluoride on enamel de- and remineralization and plaque metabolism.* J Clin Dent, 2013. **24 Spec no A**: p. A32-44.

21. Burne, R.A. and R.E. Marquis, *Alkali production by oral bacteria and protection against dental caries.* FEMS Microbiol Lett, 2000. **193**(1): p. 1-6.

22. Binnig, G., C.F. Quate, and C. Gerber, *Atomic force microscope.* Phys Rev Lett, 1986. **56**(9): p. 930-933.

23. Qi, F., P. Chen, and P.W. Caufield, *The group I strain of Streptococcus mutans, UA140, produces both the lantibiotic mutacin I and a nonlantibiotic bacteriocin, mutacin IV.* Appl Environ Microbiol, 2001. **67**(1): p. 15-21.

24. Revsbech, N.P., *Analysis of microbial communities with electrochemical microsensors and microscale biosensors.* Methods Enzymol, 2005. **397**: p. 147-66.

25. Cross, S.E., et al., *Atomic force microscopy study of the structure-function relationships of the biofilm-forming bacterium Streptococcus mutans.* Nanotechnology, 2006. **17**(4): p. S1-7.

26. Sharma, S., et al., *Nanocharacterization in dentistry.* Int J Mol Sci, 2010. **11**(6): p. 2523-45.

27. Pelling, A.E., et al., *Nanoscale visualization and characterization of Myxococcus xanthus cells with atomic force microscopy.* Proc Natl Acad Sci U S A, 2005. **102**(18): p. 6484-9.

28. Dufrene, Y.F., *Towards nanomicrobiology using atomic force microscopy.* Nature Reviews Microbiology, 2008. **6**(9): p. 674-680.

29. Thurnheer, T., et al., *Effects of Streptococcus mutans gtfC deficiency on mixed oral biofilms in vitro.* Caries Res, 2006. **40**(2): p. 163-71.

30. Vu, B., et al., *Bacterial extracellular polysaccharides involved in biofilm formation.* Molecules, 2009. **14**(7): p. 2535-54.

31. Jorand, F., et al., *Hydrophobic/hydrophilic properties of activated sludge exopolymeric substances.* Water Science and Technology, 1998. **37**(4-5): p. 307-315.

32. Marszalek, P.E., et al., *Mechanical unfolding intermediates in titin modules.* Nature, 1999. **402**(6757): p. 100-3.

33. Yakovenko, O., et al., *FimH forms catch bonds that are enhanced by mechanical force due to allosteric regulation.* J Biol Chem, 2008. **283**(17): p. 11596-605.

34. Razatos, A., et al., *Molecular determinants of bacterial adhesion monitored by atomic force microscopy.* Proc Natl Acad Sci U S A, 1998. **95**(19): p. 11059-64.

35. Dufrene, Y.F., *Recent progress in the application of atomic force microscopy imaging and force spectroscopy to microbiology.* Curr Opin Microbiol, 2003. **6**(3): p. 317-23.

36. Dupres, V., et al., *Nanoscale mapping and functional analysis of individual adhesins on living bacteria.* Nat Methods, 2005. **2**(7): p. 515-20.

37. Harimawan, A., A. Rajasekar, and Y.P. Ting, *Bacteria attachment to surfaces--AFM force spectroscopy and physicochemical analyses.* J Colloid Interface Sci, 2011. **364**(1): p. 213-8.

38. Arce, F.T., et al., *Nanoscale structural and mechanical properties of nontypeable Haemophilus influenzae biofilms.* J Bacteriol, 2009. **191**(8): p. 2512-20.

39. Busscher, H.J., et al., *Intermolecular forces and enthalpies in the adhesion of Streptococcus mutans and an antigen I/II-deficient mutant to laminin films.* J Bacteriol, 2007. **189**(8): p. 2988-95.

40. Mei, L., et al., *Influence of surface roughness on streptococcal adhesion forces to composite resins.* Dent Mater, 2011. **27**(8): p. 770-8.

41. Liu, B.H., et al., *In situ biosensing of the nanomechanical property and electrochemical spectroscopy of Streptococcus mutans-containing biofilms.* Journal of Physics D-Applied Physics, 2013. **46**(27).

42. Loskill, P., et al., *Reduced adhesion of oral bacteria on hydroxyapatite by fluoride treatment.* Langmuir, 2013. **29**(18): p. 5528-33.

43. Sharma, S., et al., *Atomic force microscopy reveals drebrin induced remodeling of f-actin with subnanometer resolution.* Nano Lett, 2011. **11**(2): p. 825-7.

44. Sharma, S., et al., *Microbicidal male contraceptive - Risug induced morpho structural damage in E-coli.* Colloids and Surfaces B-Biointerfaces, 2003. **32**(1): p. 43-50.

45. Li, L., et al., *In vitro study of biofilm formation and effectiveness of antimicrobial treatment on various dental material surfaces.* Molecular Oral Microbiology, 2010. **25**(6): p. 384-390.

46. Lee, Y.H., et al., *Proteomic Evaluation of Acquired Enamel Pellicle during In Vivo Formation.* Plos One, 2013. **8**(7).

47. Garcia-Godoy, F. and M.J. Hicks, *Maintaining the integrity of the enamel surface - The role of dental biofilm, saliva and preventive agents in enamel demineralization and remineralization.* Journal of the American Dental Association, 2008. **139**: p. 25s-34s.

48. Tabak, L.A., *In Defense of the oral cavity: The protective role of the salivary secretions.* Pediatric Dentistry, 2006. **28**(2): p. 110-117.

Chapter 6.

Nanofilaments on Glioblastoma Exosomes Revealed by Peak Force Microscopy

6.1 Abstract

Exosomes are sub-100nm extracellular vesicles secreted by normal and cancer cells. We present high-resolution structure of previously unidentified nanofilaments on glioblastoma derived exosomes, using nanoscale Peak Force imaging. These stiff, adhesive, trypsin and RNAse resistant surface nanofilaments add new dimension to the current structural knowledge of exosome-mediated intercellular communication.

6.2 Introduction

The ability of cells to communicate with each other is essential for multi-cellular organisms. A number of mechanisms, including small nano-sized, cell-derived extracellular vesicles called exosomes [1] have been investigated, as mediators of cellular interactions. In particular, the surfaces of exosomes form fascinating interfaces that may mediate their transport between cells, e.g., both as autocrine and paracrine factors in tumor microenvironments, as well as effectors for distant cellular targets, analogous to endocrine signaling. Exosomes are known to play an important role in intercellular communication by extracellular signaling [2] and horizontal mRNA/microRNA transfer [3]. Their roles in tumor proliferation [4, 5], pre-metastatic niches [6] and tumor microenvironment modulation, including glioblastoma as a model disease system, have also been proposed [7].

The quantity, surface molecular composition and dynamics of exosomes released vary depending on the cellular origin and physiological state of the cell [8]. Understanding exosome structure at nanometer resolution can provide detailed insights into the mechanisms of exosome-mediated cell-surface interactions including transport, binding to, and uptake by target cells. Electron microscopy has been the gold-standard method [9] to characterize exosomes, but is limited by potential artifacts [10]. No structural details can be resolved with optical imaging as exosomes are smaller than the diffraction limit (200-300 nm) [11]. Recently, Atomic Force Microscopy (AFM) [12] has emerged as a powerful biophysical nanoscale characterization technique that offers 3D imaging of unlabeled single exosomes, and provides additional information about the structure, mechanical properties and their specific bio-molecular composition [13, 14]. So far,

detailed surface characteristics of glioblastoma exosomes at the nanoscale level have not been reported to date.

Here, we provide first evidence of the presence of surface nanofilaments on glioblastoma derived exosomes and analyze their biophysical characteristics at the nanoscale using AFM Peak Force imaging [15]. Compared to normal exosomes, glioblastoma exosomes displayed abundant nanofilaments and the nanofilaments were trypsin and RNase resistant. We quantified the distinct structural, biophysical and biochemical properties of the exosomes and surface nanofilaments. Based on *in vitro* uptake assays, glioblastoma exosomes showed a significant higher uptake in cells compared to normal exosomes. We discuss how these newly recognized nanofilaments may help in modulating, tethering and transport of exosomes for intercellular communication.

6.3 Materials and Methods

Peak-Force Microscopy imaging: Samples were imaged in Peak Force mode using ICON AFM (Bruker Corp.). ScanAsyst Air HR cantilevers (Bruker) with spring constants of 0.4 N/m were used. Purified exosome samples were diluted 1:3 in water, incubated on freshly cleaved mica for 5 min, rinsed three times with water, and then air-dried overnight. Topographic height images and simultaneous phase, modulus and adhesion maps were recorded at 1024x1024 pixels at 2KHz. Images were flattened and plane-fitted by using the image analysis software (SPIP 5.8.2). It is likely that more exosomes with nanofilaments may remain bound to the mica (compared to exosomes without nanofilaments) after the washing step. However, we utilized non-specific adsorption of exosomes on un-functionalized mica substrates to achieve high signal-to-background ratio in PFM images. It allowed resolving the structural and biophysical properties of exosomes at the nanoscale level, which was the objective of the current study. For estimating the number of exosomes, we used 5ul drop of exosome solution, which was air dried and directly used for tapping mode AFM imaging without any washing (See Supplemental Figure S3). This allowed all the particles irrespective of the presence of surface nanofilaments to be imaged and analyzed. The results obtained from solution drop method were consistent with the BCA protein assay values and were used for normalizing the number of exosomes for incubation in cell binding assays.

Exosome Isolation: Exosome isolation was carried out by following protocols as published previously [32]. Normal human astrocytes and U251 cell lines were grown in Dulbecco's Modified Eagles Medium/F12 (CellGro) supplemented with 10% fetal bovine serum, penicillin

(50 IU/ml), and streptomycin (50 IU/ml), in 75cm^2 tissue-culture treated flasks at 37 ºC, in a humidified atmosphere and 5% CO_2 to 75-80% confluence. Cells were then cultured in exosome production medium (see Support Protocol 2) for 48hrs to produce exosome-conditioned medium; and this medium was used for isolation of exosomes by differential ultracentrifugation, with and without further purification by sucrose cushion (see Basic Protocol 1 steps 1-11a, and Support Protocol 3 for sucrose cushion details32. Resulting exosome suspensions were quantified for total exosomal protein by Pierce/Thermo Scientific bicinchoninic acid (BCA) protein assay, according to manufacturer's recommendations.

Trypsin digestion: Exosome samples purified from glioblastoma or normal cell lines were diluted 1:3 in water and treated with 0.25% trypsin (2.21 mM EDTA in HBSS without sodium bicarbonate, calcium and magnesium) for 15 min at RT. Control samples were untreated (buffer only). Samples were incubated on mica for 5 min, washed with water, and then air-dried at room temperature overnight.

Labeling of exosomes: The exosomes were labeled using CM-DiI (Life Technologies, V-22888). Briefly, purified exosome suspension was labeled with CM-DiI by adding 1 µL stock CM-DiI solution per mL suspension (adhering to manufacturer's recommendations), followed by incubation at 37 ºC for 5 minutes. Unincorporated CM-DiI was removed by dialysis against PBS, and labeled exosome solution was stored at 4 ºC, protected from light, until use.

Cell adhesion assays: Normal human astrocytes and U251 cell lines were grown in Dulbecco's Modified Eagles Medium/F12 (CellGro) supplemented with 10% fetal bovine serum, penicillin (50 IU/ml), and streptomycin (50 IU/ml), on 20 mm-diameter coverslips at 37 ºC, in a humidified atmosphere and 5% CO_2 to 80% confluence. Growth medium was removed, and replaced with exosome-free medium supplemented with labeled exosomes (final exosome concentration was 5 µg/mL exosome protein, as determined by BCA assay). Cells were incubated with labeled exosomes for 3 hours at 37 ºC, in a humidified atmosphere and 5% CO_2. Labeling medium was removed, and cells were washed three times with PBS, and then fixed with 4% neutral buffered formalin for 10 minutes at room temperature. Fixative was rinsed by removal, followed by washing 3 times with PBS. Cells were then mounted onto glass cover slips with Vectashield mounting medium (w/ DAPI counterstain, Vector Labs). Images were recorded using a combined optical/confocal microscope (Zeiss, Corp, Thornwood, NY). For imaging DAPI, the intensity of Ar laser line through a BP 420– 480nm emission filter was used. For imaging CM-Dil, we used HeNe laser line (543 nm) and LP 560nm emission filter.

6.4 Results and Discussion

Glioblastoma cell line-derived exosomes show abundant networks of surface nanofilaments

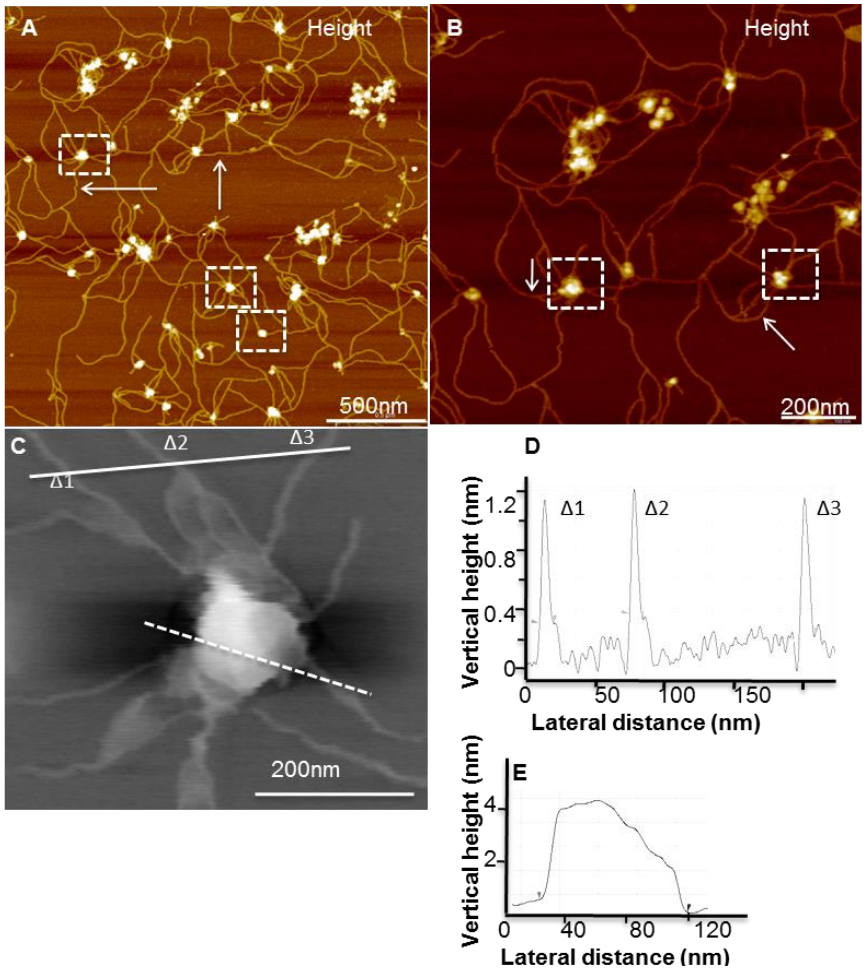

Figure 1. PFM reveals glioblastoma exosomes with abundant nanofilamentous surface extensions (a) Topographic image (z=10nm) of glioblastoma U87-derived exosomes showing round bulging vesicles (some shown in dashed boxes) surrounded by a network of nanofilaments. The nanofilaments are shown at a higher resolution (z=6nm) in (b). Size of U87 exosomes measured from typical high resolution PFM topographic image (c) are 89.3 nm in diameter and 4nm in height (e) (dashed white line). (d) Cross section profiles show ~1.2 nm high and 10 nm wide nanofilaments (marked Δ1-3, solid line line). Fewer nanofilaments were seen in U251 exosomes, but not in NHA-derived exosomes (see Figure S1). The results were confirmed by imaging samples obtained from two independent and commonly used isolations, with and without sucrose gradient purification. Size distributions show average vesicle sizes of 89 ± 3.2 nm, 80.8 ± 2.2 nm, and 70.9 ± 2.2 nm for U87, U251, and NHA respectively (n~100 individual exosomes).

Exosomes derived from several human cell lines were studied, including glioblastoma (U87 and U251), melanoma (SKMEL), and normal human astrocytes (NHA). U87 and U251 are human primary glioblastoma cell lines from grade IV tumors [16]. SKMEL28 is a malignant melanoma cell line. Normal control exosomes were isolated from a primary human astrocyte cell line (NHA). Key structural features not previously reported for exosomes, were observed at nanoscale resolution, using the recently developed variation of AFM called Peak Force Microscopy (PFM) [15]. This imaging mode is non-destructive to both tip and sample since it directly controls the peak normal force. PFM operates at low imaging forces (<100pN) permitting sub-nm imaging of soft biological structures (See supplemental). The most striking feature of the recorded PF images was the ultra-structural details of exosome surfaces (Figure 1). Whereas "Micro-scale" cellular extensions [17] and nanotubes are known to exist between cells [18], their functional mechanisms in intercellular communication remains obscure. However, PF images reveal new and distinct nanofilaments extending from the surface of glioblastoma exosomes (Figure 1). Our current work shows that the surface extensions of glioblastoma exosomes form a branched network of nanoscale inter-exosomal connections (Figure 1a-b, marked by white arrows). Individual nanofilaments within the network were measured to be 10-20 nm in diameter and up to several microns in length (Figure 1c-d). Similar, though fewer, nanofilaments were also observed in U251 exosomes. Interestingly, the nanofilaments were rarely observed in the case of normal control NHA exosomes (Figure S1). Sequential ultracentrifugation, both with and without sucrose gradient purification, yielded exosomes with indistinguishable nanofilaments under PFM. Additionally, we found that trypsin-EDTA treatment did not disrupt the network of nanofilaments or exosomes (data not shown), indicating either their non-protein nature, or inherent resistance to trypsin digestion.

Exosome morphology was measured using PF topographic images. The findings revealed 3D spherical vesicles, 80-90 nm in diameter for all three cancer cell lines (U87, U251, and SKMEL) and slightly smaller NHA exosomes (Table S1). PF images provide support to our previous findings showing exosomes as round spherical structures without cup-shaped indentations [19]. As might be expected for the low force of imaging in PF microscopy, the vesicles were measured to be higher (~4 nm) compared to those measured under standard tapping mode imaging due to minimal compression of the vesicle lipid bilayers [19].

Mapping of biophysical characteristics (Young's modulus and adhesion strength) of nanofilaments

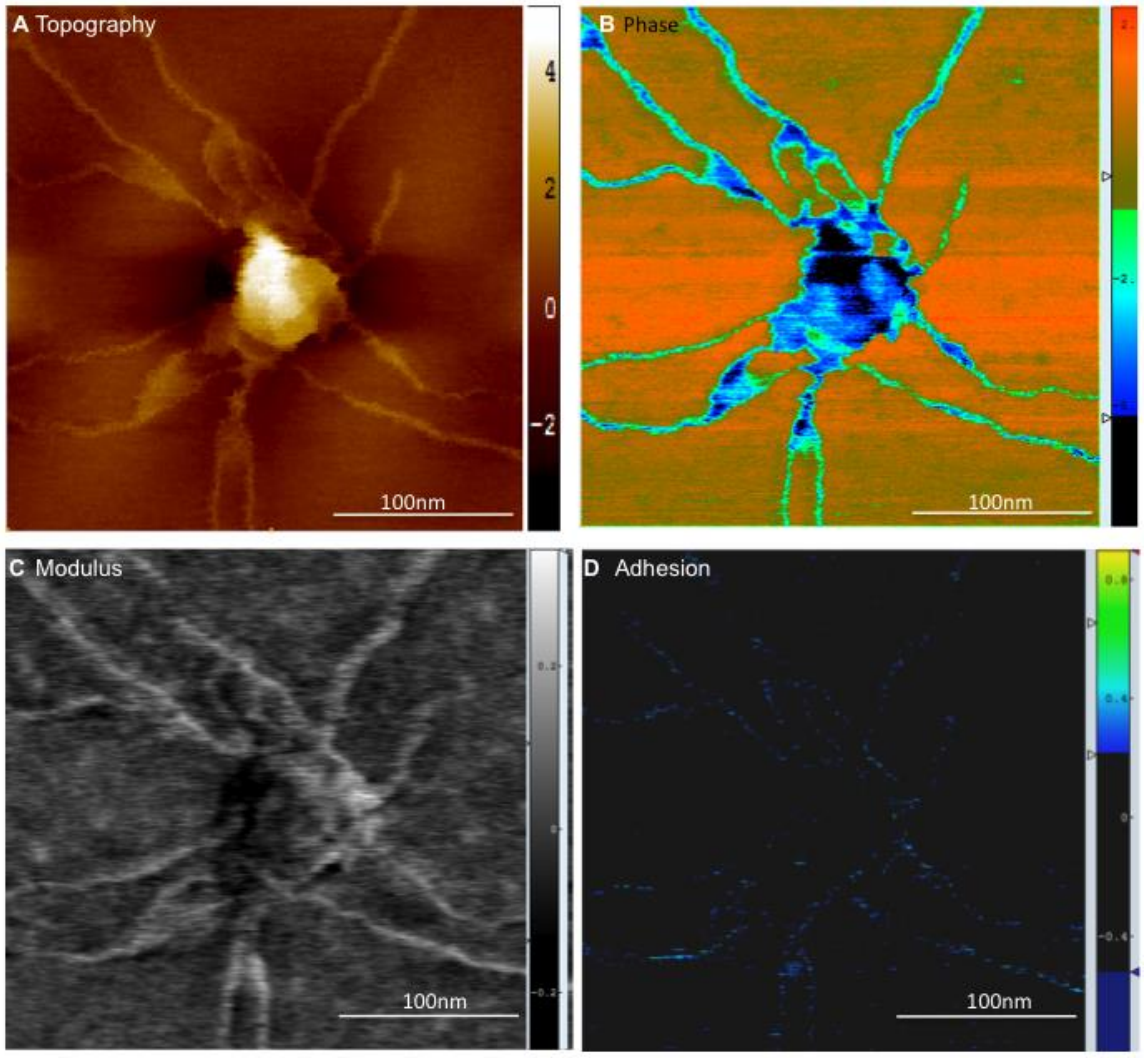

Figure 2. PFM imaging enabled independent extraction and mapping of biophysical parameters at less than 5nm lateral resolution, revealing relatively stiffer and more adhesive nanofilaments, in comparison to parent vesicle region. Quantitative mapping of biophysical parameters such as (a) topography (range z=5nm), (b) phase (z=10.6mV), (c) modulus (z=2GPa) and (d) adhesion (z=1.6nN) were simultaneously mapped, as represented by U87 exosomes with extending surface nanofilaments.

Next, we explored the biophysical properties of glioblastoma exosomes, including their surface nanofilaments. AFM tapping mode height and phase imaging has been widely used to study the structure and morphology of biomolecules [20-22]. Additionally, quantitative mechanical information on surface modulus can be obtained by nanoindentation and force volume AFM imaging [23, 24], using appropriate mechanical contact models. However, nanoindentation and force volume imaging are limited in lateral resolution and time extensive. Using PFM, <5 nm lateral-resolution maps were typically obtained to determine quantitative information about the topography, change in phase, stiffness (elastic modulus) and adhesion strength (stickiness) of the vesicles (See supplemental) as represented in Figure 2.

Figure 2a shows nanoscale topographic image of a single isolated exosome and extending surface nanofilaments at nanoscale resolution. Complementary to the 3D topography, the phase images can detect inhomogeneous chemical, structural or mechanical properties [25] of the sample. Here, local phase heterogeneities in exosomes (Figure 2b) indicated a dense exosomal core relative to surface filaments. Furthermore, the prominent differences in nanofilaments and vesicle regions were revealed in simultaneously recorded elastic modulus and adhesion maps (Figure 2c-d). Figure 2c-d corresponds to variations in the elastic modulus and adhesion forces, respectively, both showing significant mechanical heterogeneity between the exosomes and nanofilaments. In PeakForce mode, the Young's modulus is calculated using a DMT model that is applied to the unloading portion of the force-separation curve, which takes into account the adhesive forces between the tip and the surface [15]. The elastic modulus map obtained by PF imaging (Figure 2c) revealed stiffer (bright) nanofilaments (up to 2 GPa) compared to the exosomal core regions (dark). While surface effects can be expected to affect the obtained

modulus values, the contrast between the modulus was also clearly distinct in regions were the stiffer filaments are observed on top of the vesicle regions. Additionally, we performed single force-indentation curve testing over various regions using sharper tips (~1 nm) and thin film Hertz model [26], which also indicated stiffer nanofilaments. The measured stiffness of exosome nanofilaments were comparable in range to other filamentous biomolecules (See Supplemental Table 2) including Peak Force measurements to identify stiffness profiles of nanoscale fibrils such as Tau and alpha-synuclein. Additionally, the non-specific adhesion of the exosomes to bare AFM probes was quantified across the topography. The nanofilaments were found to be significantly more adhesive ($P<0.05$) than vesicular regions (Figure 2d) with adhesion forces up to 1.6 nN (blue).

Glioblastoma exosomes show greater cellular uptake compared to normal control exosomes

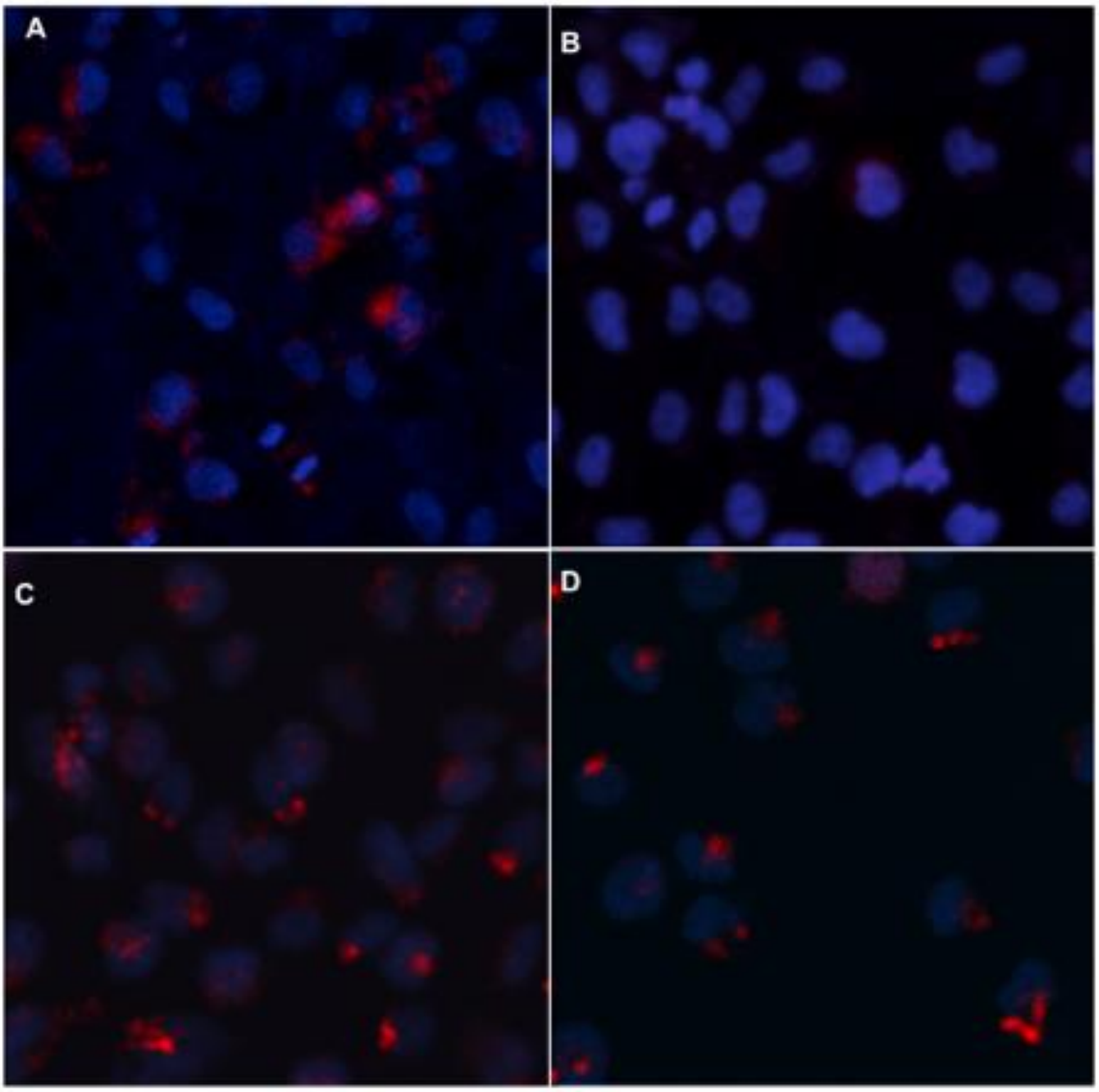

Figure 3. *In vitro* cell assays shows greater binding of glioblastoma derived U251 exosomes compared to normal NHA exosomes (images taken at 200X magnification). (A) NHA cells + U251 exosomes (B) NHA cells + NHA exosomes (C) U251 cells + U251 exosomes and (D) U251 cells + NHA exosomes. Cell nuclei are stained with DAPI (blue) and exosomes stained with CM-DiI (red).

One intriguing question is the functional consequence of exosome nanofilaments, in patho-physiological states such as glioblastoma. Our structural data highlights that nanofilaments appear on the surface of glioblastoma exosomes. Consequently, we investigated their potential strength in binding to target cells by assaying the cellular binding and uptake of glioblastoma-derived exosomes compared to normal exosomes. To achieve this, we incubated purified exosomes derived from U251 and NHA cells (labeled with membrane dye CM-DiI) with U251 or NHA cells, respectively (Figure 3). We found that *in vitro* cellular uptake of glioblastoma (U251) exosomes, was significantly higher than that of normal control NHA exosomes. Although the exact mechanism of increased uptake of glioblastoma exosomes, which express many fold more surface nanofilaments (with respect to NHA exosomes) still need to be identified, these preliminary results support our hypothesis that increasing numbers of nanofilaments could play a functional role in cellular binding and uptake of exosomes and may be relevant in intercellular interactions in glioblastoma exosomes.

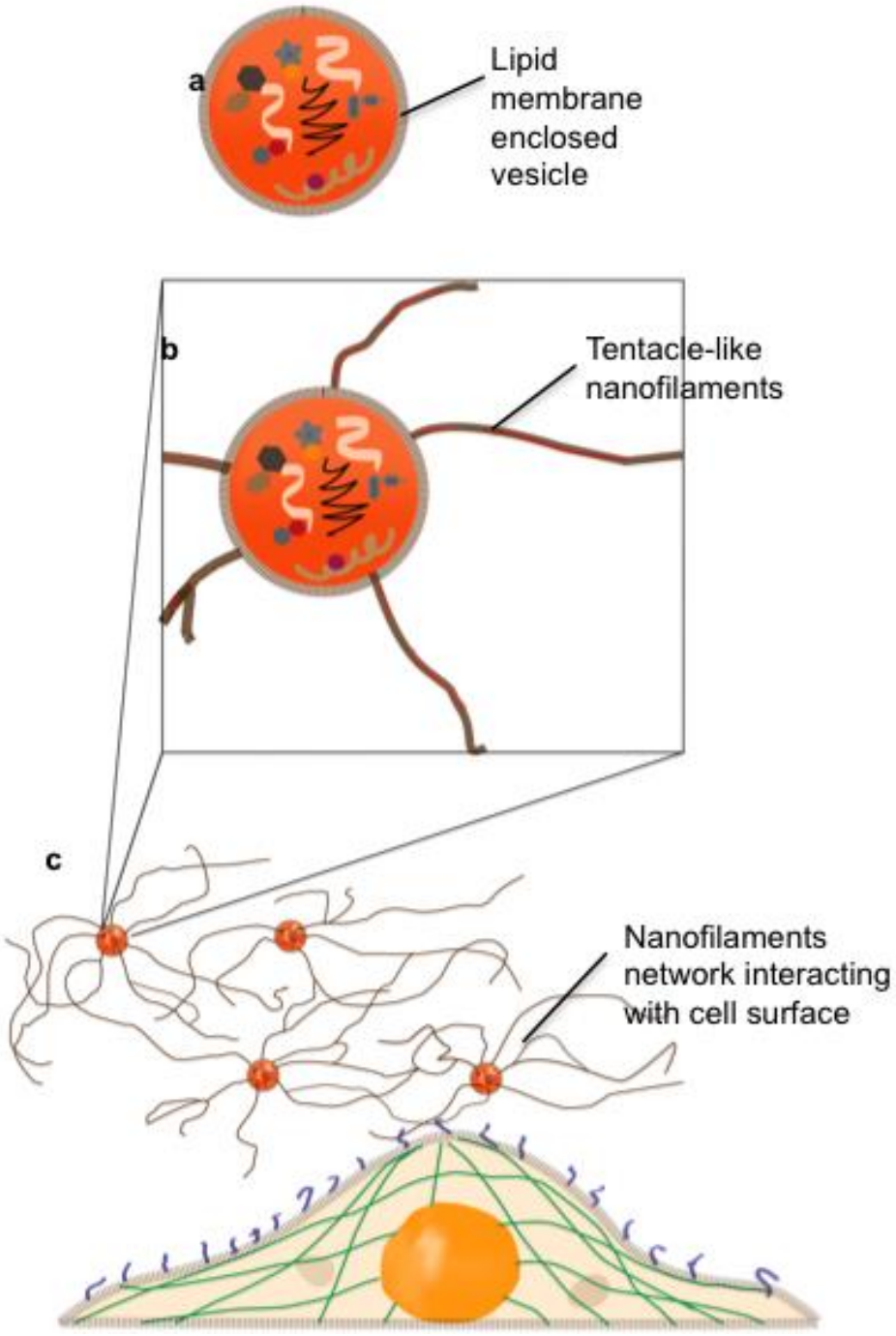

Figure 4. Proposed hypothetical schematic model for exosomes with nanofilaments mediating intercellular transport and communication (A) Current model of exosomes with membrane enclosed proteomic and genomic content (B) Glioblastoma exosomes with surface nanofilaments (C) Nanofilaments of glioblastoma exosomes interacting with target cell.

Filamentous connections between cells that allow intercellular communications are typical of multicellular organisms. Recent reports demonstrate the existence of a network of intercellular membrane nanotubes enabling long-distance communication in mammalian cells [17, 18]. These tunneling nanotubes have been shown to facilitate intercellular transfer of cytoplasmic molecules and even organelles and viruses [27, 28]. Using correlative FESEM (Field Emission Scanning Electron Microscopy) and AFM, we previously demonstrated the structure of saliva-derived exosomes and oral cancer exosomes [19, 29]. Evidence of associated inter-vesicular structures was observed under FESEM and AFM but not resolved in detail. Our current findings on structural, nanomechanical and cellular uptake of exosomes provide the first high-resolution nanoscale characteristics of exosome nanofilaments. The adhesive characteristics and cell binding assays suggest their likely role in direct physical-contact with target cells for intercellular communication (Figure 4b-c). The nature and function of these observed nanofilaments needs to be further investigated, but could well provide a significant advance over existing models of exosome-cell interactions, which are largely based on exosomes being "distinct membrane enclosed vesicles" (Figure 4a) capable of intercellular communication and transport of proteomic and genomic content among distant cells [30].

We found a positive correlation between abundance of nanofilament extensions and glioblastoma cell line-derived exosomes. These nanofilaments were measured to be 10-20 nm wide, compared to the exosome vesicular diameters around 100nm. It is known that tip convolution likely results in broadening effect on measured exosome dimensions yet the images provide good estimates of upper limits of exosome diameters and nanofilaments height and widths. The lengths of nanofilaments extend up to several microns, comparable to dimensions of target cells

themselves. We tentatively suggest that these structures are composed of lipids and nucleic acids (based on filamentous shape, close to 1.2nm height in AFM images and similar elastic modulus values ranging from MPa to few GPa). It is noteworthy that the general physical characteristics and appearance of exosomes, their nucleic acid contents (noted to contain microRNA, mRNA, and even potential retro-transposable elements) [3, 31], and even their subcellular biological underpinnings suggest their strong relationship to viruses [32]. Within this context, we suggest that the biophysical and potential functional characteristics of these nanofilaments may be analogous to virulence factors for microbes, such as gp120/gp41 for Human Immunodeficiency Virus (HIV) [33], or hemagglutinin and neuraminidase for influenza virus infection [34, 35]. Further exploration of nanofilaments may not only hold significance for exosome biology and their role in intercellular communication, but also for their role as virulence factors in exosome associated diseases such as cancer, autoimmune diseases, and infectious diseases. Further experimental investigations are needed to establish the occurrence and relevance of nanofilaments in a diverse population of exosomes imaged under physiological buffer conditions.

Nanofilaments may serve as long tethers for anchorage, increasing the probability of exosome binding to target cells. They may provide enhanced rigidity or structural integrity to parent exosomes. These rigid and adhesive nanofilaments may also harbor specific recognition motifs for cognate receptors on target cells, perhaps thereby further modulating exosome targeting, uptake, and effector functions. Therefore we propose a tentative model (Figure 4) of nanofilament augmented exosome interactions with target cells.

6.5 Conclusions

In conclusion, we have shown quantitative differences between the structure and biophysical properties of cancer cell line-derived and normal control cell line-derived exosomes, imaged *in vitro* using PF Microscopy. Our results demonstrate that in addition to commonly accepted exosome models of membrane-enclosed vesicles carrying proteomic and genomic cargo, glioblastoma- and malignant melanoma-derived exosomes (and likely other malignant cell-derived exosomes) also possess surface nanofilaments that have not been identified previously. The PFM method employed in these studies allowed the necessary resolution for revealing nanofilaments on exosome surfaces. To the best of our knowledge, this is the first report showing nanofilaments extending from the surface of exosomes, and demonstrates direct physical connections between exosomes. We believe that exosomes with their long tentacle-like nanofilaments may be a fascinating new route for cell-cell communication that warrants further investigations.

6.6 Supplementary Information

Peak Force Microscopy:

PFM is a new quantitative AFM-based imaging technique that allows simultaneous imaging of the structure and the physical properties (e.g., elasticity and adhesion) of the sample at high speed and high resolution in an unprecedented manner [36]. In PFM, the probe is oscillated in the vertical direction with amplitude of 100–300 nm and at frequencies up to 2kHz. The z piezo is driven with a sinusoidal rather than a triangular waveform in conventional force–distance (F-d) curves. This oscillating system allows direct force control of damaging lateral forces, which is very useful for the structural imaging of soft samples such as exosomes. In addition, individual force curves can be analyzed to generate adhesion and mechanical maps to a much better resolution (up to 2048 pixels × 2048 pixels) than in conventional Force Volume (FV) imaging (at best 64 pixels × 64 pixels). The advantage of PFM is that F-d curves are recorded at frequencies that are 3 orders of magnitude higher than in FV imaging [37]. As a result, the imaging speed is similar to that of topographic imaging (8 min for a 512 pixel × 512 pixel image recorded at 0.25 kHz), which is much faster than conventional FV imaging (80 min for a 64 pixel × 64 pixel image recorded at 1 Hz). The adhesion force is calculated as in regular force mode and is the maximum step height between the baseline and the minimum value of the F-d curve. The elastic modulus is calculated by extrapolating the retraction curve close to the contact point and using a Derjaguin–Mueller–Toporov (DMT) [38] model. So far, PFM has been used to explore the structural and physical properties of a variety of biological samples including amyloid [39], membrane proteins [40] and cells [41].

Modulus determination:

When indenting nanoscale scale filaments with a relatively large tip radius (5 nm) the finite sample thickness effects need to be considered. The force curve displays distinct regimes: from being free in air above the sample to the initial filament indenting section where the tip 'only' feels the filament, to where the mica underneath starts to play a role, and finally to the last section where only the hard surface is felt by the probe. The initial 20% of the total height of a feature is thought to be unaffected by these final sample thickness effects for large objects relative to the tip radius [42]. However, at the typical size scales of these nanofilaments, a correction for these effects is necessary [43,44]. In the PFM software these effects are accounted. Thus, while PFM force modulus image shows distinction between softer vesicular region of the exosome (lighter) and the stiffer nanofilaments (dark regions), we further confirmed our observations by testing the reduced Young modulus of the exosomes using single indentation measurements and correcting for the substrates effects. The results from the point indentations using corrected thin film modified Hertz model [45,46] were consistent with the DMT modulus obtained from Peak Force mapping.

	U87	U251	SKMEL	NHA
Size (Mean± s.d.) nm	89.0 ± 3.2	80.8 ± 2.5	78.5 ± 1.85	70.9 ± 2.2
Shape	Spherical	Spherical	Spherical	Spherical
Vesicle height (nm)	~4	~4	~4	~4
Nanofilament counts	4-8 per exosome	1-6 per exosome	1-4 per exosome	-
Nanofilament lengths	up to few μms	up to few μms	up to 1μm	-
Nanofilament height (nm)	**1.2 ± 0.3nm**	**1.2± 0.3nm**	**1.2± 0.2nm**	-
	(n=11)	**(n=10)**	**(n=11)**	
Nanofilament after trypsin	+++	+	+	-

Table S1. Morphology of human glioblastoma cell line derived exosomes obtained from PF imaging.

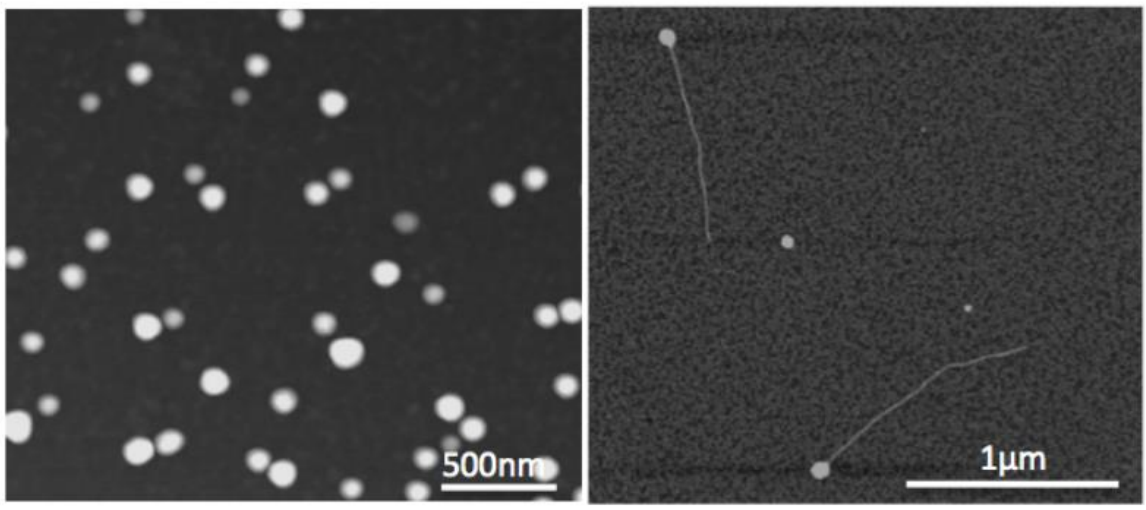

Figure S1. (Left) Normal control astrocyte derived exosomes showing round vesicular structures without any nanofilaments (Right) U251 cell derived exosomes showing single nanofilaments.

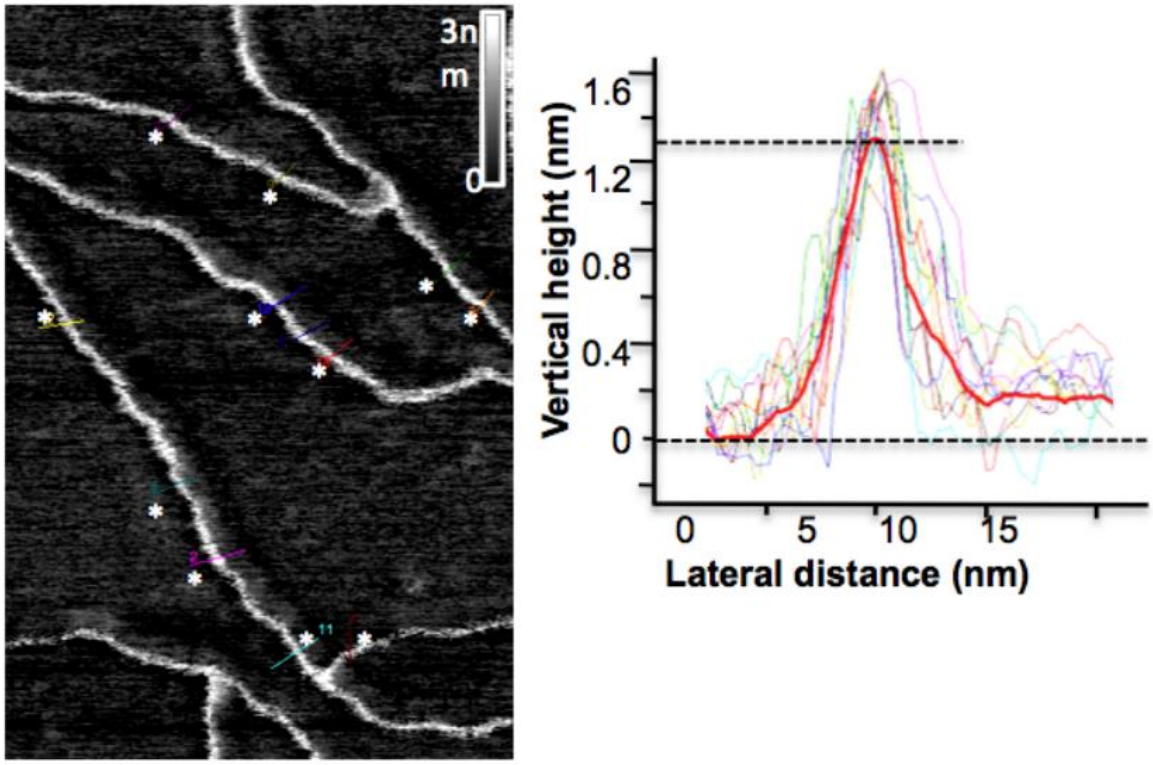

Figure S2. Topographic image of nanofilaments (right) and cross section profiles (left) showing height of the filaments in different regions. Line profile shows the mean curve (average height 1.2 ± 0.3nm) obtained from 11 different nanofilament sections (marked with asterisk * on the image in right).

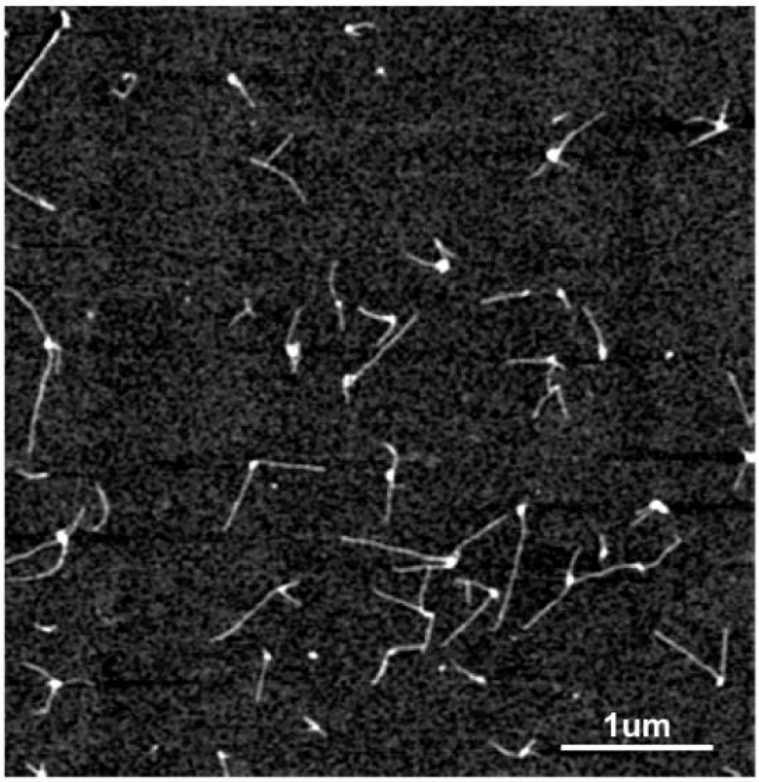

Figure S3. Representative image from AFM topographic scan of non-washed samples for exosome enumeration using 5 µL solution (1: 3 exosome dilution in water) dropped on freshly cleaved mica surface, air dried and imaged.

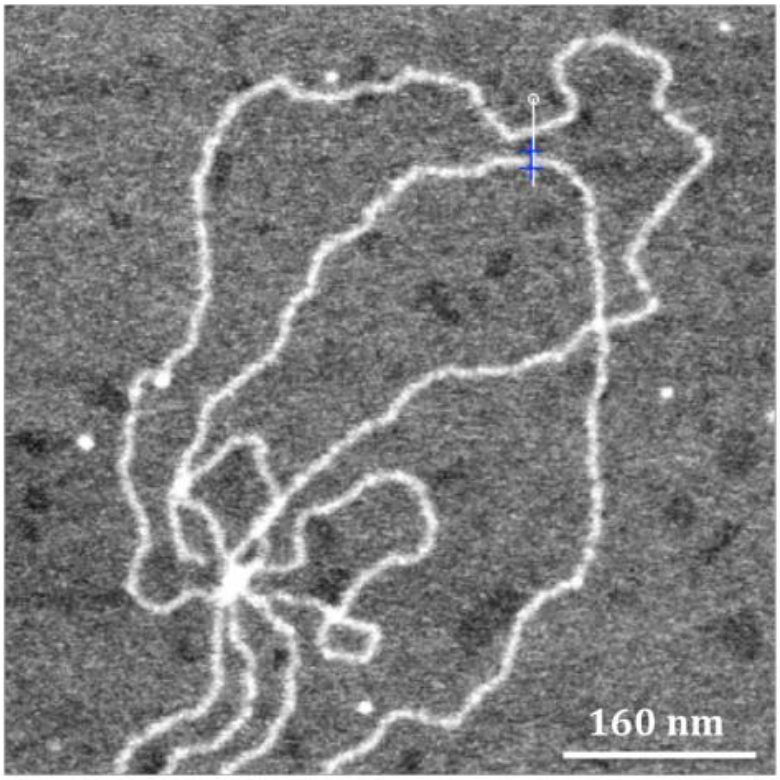

Figure S4. Peak Force image of lambda-phage DNA on mica surface for estimation of tip induced width increase. DNA was measured to have a half-maximum-height–width of 12 ± 0.8 nm and a height of 0.7 ± 0.2 nm. Considering that the theoretical DNA width is around 2 nm, this result suggests that there is an about 10nm tip-induced width increase.

Biopolymer	Modulus Range	Reference
Beta Lactoglobulin amyloid fibrils	3.3-4 GPa (Peak Force)	Adamciket al. [40]
Alpha Synuclein (10 nm wide, 100 nm length)	1.3-2.1 GPa (Peak Force)	Sweers et al. [42]
	2.2 ±0.6 GPa (Peak Force)	Adamciket al. [47]
Collagen	14-20 MPa (Persistence length measurement)	Lovelady et al. [48]
Polyurethane	1.5-2.7 GPa (AFM indent and Peak Force)	Dokukin et al. [49]
Tau fibril polypeptide	3.4 ±0.7 GPa (Peak Force)	Adamciket al. [47]
DNA	~300 MPa (Laser tweezers)	Smith et al. [50]
Exosome nanofilament	1.5 ± 0.6 GPa (Peak Force)	Current study

Table S2. Comparison of range of Young's modulus for different polymers from previous studies including amyloid fibrils, collagen and polyurethanes.

6.7References

1. Théry C. 2011 Exosomes: secreted vesicles and intercellular communications. *F1000 Biol. Rep*. **3**, 15.DOI 10.3410/B3-15.

2. Calzolari A, Raggi C, Deaglio S, Sposi NM, Stafsnes M, Fecchi K, Parolini I, Malavasi F, Peschle C, Sargiacomo M, Testa U. 2006 TfR2 localizes in lipid raft domains and is released in exosomes to activate signal transduction along the MAPK pathway. *J. Cell. Sci*.**119,** 4486-4498. DOI 10.1242/jcs.03228

3. Valadi H, Ekstrom K, Bossios A, Sjostrand M, Lee JJ, Lotvall JO. 2007 Exosome-mediated transfer of mRNAs and microRNAs is a novel mechanism of genetic exchange between cells. *Nat. Cell. Biol.* **9,** 654-659. DOI 10.1038/ncb1596.

4. Taylor DD, Gercel-Taylor C. 2008 MicroRNA signatures of tumor-derived exosomes as diagnostic biomarkers of ovarian cancer. *Gynecol. Oncol*. **110**, 13-21. DOI 10.1016/j.ygyno.2008.04.033.

5. Skog J, Würdinger T, van Rijn S, Meijer DH, Gainche L, Sena-Esteves M, Curry WT Jr, Carter BS, Krichevsky AM, Breakefield XO. 2008 Glioblastoma microvesicles transport RNA and proteins that promote tumour growth and provide diagnostic biomarkers. *Nat. Cell Biol.* **10**,1470-1476. DOI 10.1038/ncb1800.

6. Jung T, Castellana D, Klingbeil P, Cuesta Hernández I, Vitacolonna M, Orlicky DJ, Roffler SR, Brodt P, Zöller M. 2009 CD44v6 dependence of premetastatic niche preparation by exosomes. *Neoplasia*.**11**,1093-1105.

7. Peinado H, Alečković M, Lavotshkin S, Matei I, Costa-Silva B, Moreno-Bueno G, Hergueta-Redondo M, Williams C, García-Santos G, Ghajar C, Nitadori-Hoshino A, Hoffman C, Badal K, Garcia BA, Callahan MK, Yuan J, Martins VR, Skog J, Kaplan RN, Brady MS, Wolchok JD, Chapman PB, Kang Y, Bromberg J, Lyden D. 2012 Melanoma exosomes educate bone marrow progenitor cells toward a pro-metastatic phenotype through MET. *Nat. Med.***18**, 883-891. DOI 10.1038/nm.2753.

8. Théry C, Ostrowski M, Segura E. 2009 Membrane vesicles as conveyors of immune responses. *Nat. Rev. Immunol*. **9**, 581-593. DOI 10.1038/nri2567.

9. Pan BT, Teng K, Wu C, Adam M, Johnstone RM. 1985 Electron microscopic evidence for externalization of the transferrin receptor in vesicular form in sheep reticulocytes. *J. Cell Biol*. **101**, 942-948.

10. Raposo G, Stoorvogel W. 2013 Extracellular vesicles: exosomes, microvesicles, and friends. *J. Cell Biol*. **200**, 373-383. DOI 10.1083/jcb.201211138.

11. Müller G. 2012 Novel Tools for the Study of Cell Type-Specific Exosomes and Microvesicles. *J. Bioanal. Biomed.***4**, 046-060. DOI 10.4172/1948-593X.1000063

12. Binnig G, Quate CF, Gerber C. 1986 Atomic force microscope. *Phys. Rev. Lett*. **56**, 930-933.

13. Sharma S, Gimzewski JK. 2012 The Quest for Characterizing Exosomes: Circulating Nano-Sized Vesicles. *J. Nanomed. Nanotechol.***3**, e115.DOI http://dx.doi.org/10.4172/2157-7439.1000e115.

14. Müller DJ, Dufrêne YF. 2011 Atomic force microscopy: a nanoscopic window on the cell surface. *Trends Cell Biol.***8**, 461-469. DOI 10.1016/j.tcb.2011.04.008.

15. Adamcik J, Berquand A, Mezzenga R. 2011 Single-step direct measurement of amyloid fibrils stiffness by peak force quantitative nanomechanical atomic force microscopy. *Appl. Phys. Lett.* **98**, 193701. DOI 10.1063/1.3589369

16. Clark MJ, Homer N, O'Connor BD, Chen Z, Eskin A, Lee H, Merriman B, Nelson SF. 2010 U87MG decoded: the genomic sequence of a cytogenetically aberrant human cancer cell line. *PLoS Genet.***6**, e1000832.DOI 10.1371/journal.pgen.1000832.

17. Rustom A, Saffrich R, Markovic I, Walther P, Gerdes HH. 2004 Nanotubular highways for intercellular organelle transport. *Science***303**, 1007-1010. DOI 10.1126/Science.1093133.

18. Gerdes HH, Bukoreshtliev NV, Barroso JF. 2007 Tunneling nanotubes: a new route for the exchange of components between animal cells. *FEBS Lett.***581**, 2194-2201. DOI 10.1016/j.febslet.2007.03.071.

19. Sharma S, Rasool HI, Palanisamy V, Mathisen C, Schmidt M, Wong DT, Gimzewski JK. 2010 Structural-mechanical characterization of nanoparticle exosomes in human saliva, using correlative AFM, FESEM, and force spectroscopy.*ACS Nano* **4**, 1921-1926. DOI 10.1021/nn901824n

20. Sharma S, Zhu H, Grintsevich EE, Reisler E, Gimzewski JK. 2013 Correlative nanoscale imaging of actin filaments and their complexes.*Nanoscale***5**, 5692-5702.DOI 10.1039/c3nr01039b.

21. Lal R, John SA. 1994 Biological applications of atomic force microscopy.*Am. J. Physiol.* **266**, C1-C21.

22. Brown BP, Picco L, Miles MJ, Faul CF. 2013 Opportunities in high-speed atomic force microscopy. *Small***9**, 3201-3211. DOI 10.1002/smll.201203223.

23. A-Hassan E, Heinz WF, Antonik MD, D'Costa NP, Nageswaran S, Schoenenberger CA, Hoh JH. 1998 Relative microelastic mapping of living cells by atomic force microscopy. *Biophys. J.***74**, 1564-1578. DOI 10.1016/S0006-3495(98)77868-3.

24. Dufrêne YF, Pelling AE. 2013 Force nanoscopy of cell mechanics and cell adhesion.*Nanoscale***5**, 4094-4104.DOI 10.1039/c3nr00340j.

25. García R, Magerle R, Perez R. 2007 Nanoscale compositional mapping with gentle forces. *Nat. Mater.***6**, 405-411. DOI 10.1038/Nmat1925.

26. Chadwick RS. 2002 Axisymmetric Indentation of a Thin Incompressible Elastic Layer

SIAM. J. Appl. Math. **62**, 1520-1530. DOI 10.1137/S0036139901388222.

27. Schara K, Jansa V, Sustar V, Dolinar D, Pavlic JI, Lokar M, Kralj-Iglic V, Veranic P, Iglic A. 2009 Mechanisms for the formation of membranous nanostructures in cell-to-cell communication. *Cell Mol. Biol. Lett*. **14**, 636-656. DOI 10.2478/s11658-009-0018-0.

28. Belting M, Wittrup A. 2008 Nanotubes, exosomes, and nucleic acid-binding peptides provide novel mechanisms of intercellular communication in eukaryotic cells: implications in health and disease. *J. Cell Biol*. **183**, 1187-1191. DOI 10.1083/jcb.200810038.

29. Sharma S, Gillespie BM, Palanisamy V, Gimzewski JK. 2011 Quantitative nanostructural and single-molecule force spectroscopy biomolecular analysis of human-saliva-derived exosomes. *Langmuir* **27**, 14394-14400. DOI 10.1021/la2038763.

30. Ratajczak J, Miekus K, Kucia M, Zhang J, Reca R, Dvorak P, Ratajczak MZ. 2006 Embryonic stem cell-derived microvesicles reprogram hematopoietic progenitors: evidence for horizontal transfer of mRNA and protein delivery. *Leukemia***20**, 847-856. DOI 10.1038/Sj.Leu.2404132.

31. Pegtel DM, Cosmopoulos K, Thorley-Lawson DA, van Eijndhoven MA, Hopmans ES, Lindenberg JL, de Gruijl TD, Würdinger T, Middeldorp JM. 2010 Functional delivery of viral miRNAs via exosomes.*Proc. Natl. A*

*cad. Sci. USA***107**, 6328-6333.DOI 10.1073/pnas.0914843107.

32. Gould SJ, Booth AM, Hildreth JE. 2013 The Trojan exosome hypothesis. *Proc. Natl. Acad. Sci. USA* **100**, 10592-10597. DOI 10.1073/pnas.1831413100.

33. Pierson TC, Doms RW. 2003 HIV-1 entry and its inhibition.*Curr Top MicrobiolImmunol*.**281**, 1-27. DOI 10.1007/978-3-642-19012-4_1

34. Gerlach T, Kühling L, Uhlendorff J, Laukemper V, Matrosovich T, Czudai-Matwich V, Schwalm F, Klenk HD, Matrosovich M. 2012 Characterization of the neuraminidase of the H1N1/09 pandemic influenza virus. *Vaccine***30**, 7348-7352.DOI 10.1016/j.vaccine.2012.09.078.

35. Kang SM, Song JM, Compans RW. 2011 Novel vaccines against influenza viruses.*Virus Res*. **162**, 31-38. DOI 10.1016/j.virusres.2011.09.037.

36. Garcia R, Perez R. 2002. Dynamic atomic force microscopy methods. Surf Sci Rep. 47(6-8), 197-301.

37. Derjaguin BV, Muller VM, Toporov YP. 1994. Effect of Contact Deformations on the Adhesion of Particles. Prog Surf Sci. 45(1-4), 131-143.

38. Derjaguin BV, Muller VM, Toporov YP. 1975. Effect of Contact Deformations on Adhesion of Particles. J Colloid Interf Sci. 53(2), 314-326.

39. Rico F, Su C, Scheuring S. 2011. Mechanical mapping of single membrane proteins at submolecular resolution. Nano Lett. 11(9), 3983-3986.

40. Adamcik J, Berquand A, Mezzenga R. 2011. Single-step direct measurement of amyloid fibrils stiffness by peak force quantitative nanomechanical atomic force microscopy.ApplPhysLett.98(19).

41. Heu C, Berquand A, Elie-Caille C, Nicod L. 2012. Glyphosate-induced stiffening of HaCaT keratinocytes, a Peak Force Tapping study on living cells.Journal of structural biology. 178(1), 1-7.

42. Sweers, K.; van der Werf, K.; Bennink, M.; Subramaniam, V. 2011. Nanomechanicalproperties of α-synuclein amyloid fibrils: a comparative study by nanoindentation, harmonic force microscopy, and Peakforce QNM. Nanoscale Res Lett.6 (1), 270.DOI 10.1186/1556-276X-6-270.

43. Guo S, Akhremitchev BB. 2006. Packing density and structural heterogeneity of insulin amyloid fibrils measured by AFM nanoindentation. Biomacromolecules.7 (5), 1630-6.DOI 10.1021/bm0600724.

44. Akhremitchev BB, Walker GC. 1999. Finite Sample Thickness Effects on Elasticity Determination Using Atomic Force Microscopy. Langmuir. 15 (17), 5630-5634. DOI Doi 10.1021/La980585z.

45. Sharma S, Cross SE, French S, Gonzalez O, Petzold O, Baker W, Walczak W, Yongsunthon R, Baker D, Gimzewski JK. 2009. Influence of Substrates on Hepatocytes: A Nanomechanical Study. Journal of Scanning Probe Microscopy. 4(1), 7-16. DOI doi.org/10.1166/jspm.2009.1002

46. Chadwick RS. 2002. Axisymmetric Indentation of a Thin Incompressible Elastic Layer. SIAM J. Appl. Math. 62, 1520-1530.

47. Adamcik J, Lara C, Usov I, Jeong JS, Ruggeri FS, Dietler G, Lashuel HA, Hamley IW, Mezzenga R. 2012. Measurement of intrinsic properties of amyloid fibrils by the peak force QNM method. Nanoscale. 4, 4426-4429.

48. Dokukin ME, Sokolov I. 2012. Quantitative mapping of the elastic modulus of soft materials with HarmoniX and PeakForce QNM AFM modes. Langmuir. 28, 16060- 16071.

49. Lovelady HH, Shashidhara S, Matthews WG. 2013. Solvent specific persistence length of molecular type I collagen. Biopolymers. DOI 10.1002/bip.22365

50. Smith SB, Bustamante C, 1996. Overstretching B-DNA: the elastic response of individual double-stranded and single-stranded DNA molecules.Science. 9(271), 795-799.

Chapter 7.

Nano-scale Characterization of Exosomes

7.1 Abstract

Exosomes are 50-120 nm sized vesicles that are secretedby mammalian cells. As mediators of cell-cell communication, exosomes carry nucleic acids, proteins, and lipids to the recipient cells. The structural properties of exosomes are not well-known due to their small size and the optimization of exosomes isolation and characterization is needed. Here we isolated exosome from two different methods and characterized the high-resolution structure using atomic force microscope (AFM). Exosomes purified from antibody-modified magnetic beads kit showed rougher phase images than exosomes purified from ultracentrifugation while the overall exosomes dimensions remained the same. Also, we found nanofilaments with purified exosomes regardless of purification methods. Finally, we also purified exosomal nucleic acids and obtained high-resolution images.

7.2 Introduction

Cells utilize vesicles for intercellular signaling, transporting, and trafficking of metabolites. Among vesicles, exosomes, 50-120 nm-sized vesicles are of particular interest. Due to their small size, it was once believed that exosomes were random cell debris, but now it is known that exosomes are actively secreted from cells with specific markers [1-4]. Exosomes are generated through the formation of multivesicular bodies (MVBs) and then mature MVBs are fused with the plasma membrane and the contents, including the exosomes, are released into the extracellular matrix. Released exosomes either fuse with the plasma membrane of recipient cells or are delivered via receptor-mediated uptake [1-4].

Exosomes carry nucleic acids, proteins, and lipids and deliver these diverse components to recipient cells. Based on the exosome content database, Exocarta (http://www.exocarta.org), 3,408 mRNAs, 2,838 miRNAs, 9,769 proteins, and 1,116 lipids have been identified in exosomes purified from various cell types. Exosomes transport mRNA and miRNA that affect the recipient cells. Due to the inherent structural instability of RNAs, most of the RNAs in exosomes are degraded but several studies have identified that mRNAs purified from exosomes were able to support protein synthesis *in vitro*. Based on this finding, now exosomes are regarded as cell-cell communicators. Exosomes also carry membrane transport and fusion proteins. For example, CD63, a tetraspanin protein, is a characteristic marker of exosomes. Along with tetraspanins, heat-shock proteins, GTPases, metabolic enzymes, cytoskeletal proteins, and MVB biogenesis proteins are found within and on the surface of exosomes. Besides proteins and nucleic acids, exosomes are mainly composed of lipids such as cholesterol, diglycerides, sphingolipids, phospholipids, glycerophospholipids, and polyglycerophospholipids. Even though

these components derive from the progenitor cells, the ratio of lipids is not the same. Exosome lipids contain an increased proportion of sphingomyelin, phosphpatidylserine, phosphatidylcholine, phosphatidylinositol, and cholesterol, and this may account for the increased rigidity of exosomes [5].

Most mammalian cells secret exosomes actively [2]. As the genetic information in exosomes may influence the recipient cells, the role of exosomes in cancer development and metastasis is of interest. For instance, mRNAs in exosomes can affect the protein expression in the recipient cells [6]. The secretion of exosomes was more active in ovarian cancer cell patients compared to in benign or healthy patients [7-8]. This may indicate that in cases of cancer growth and metastasis, the cross talks between cells may be important in promoting pre-metastatic niche, and that exosomes are the messenger that carries nucleic acids to manipulate the recipient cell.Also, the nucleic acids in exosomes have the potential to be used as a diagnostic marker. RNAs in exosomes are different from the RNA content in the progenitor cells. However, RNAs in exosomes are similar to those of original cells when the cells are tumorous [9-10]. Thus, more research on exosomes may reveal how cancer cells grow and metastasize.

Along with determining the roles of exosomes in cell-cell communications, isolation and characterizationof exosomes are important so that researchers would have a better understanding of the purity, yield, and structural information of exosome samples as well [11].

For isolation of exosomes, it is conventionally utilized the sequential centrifugation and ultracentrifugation to spin down exosomes in cell culture media or body fluids [12]. Sucrose

gradient density ultracentrifugation is used when the exosomes sample is required to be extra pure without protein contaminations [13]. Size exclusion chromatography is also used to purify exosomes based on their physical dimensions [14]. In addition, we could isolate exosomes by the surface marker proteins. The antibodies against exosomes markers such CD9, CD63, CD81, and EpCAM are modified with magnetic beads to capture and purify exosomes [13, 15].

After isolation of exosomes, the characterization of the exosome samples is needed. It is difficult to characterize the exosomes due to their nanometer dimensional scales. The particle size distribution of extracellular vesicles has analyzed with transmission electron microscopy (TEM), flow cytometry, resistive pulse sensing, andnanoparticle tracking analysis [16]. TEM would give a standard size distribution information while it may not show a physiologically relevant state of exosomes. Flow cytometry is not best for exosomes as it has a poor resolution when the particle diameter is less than 100 nm. Resistive pulse sensing and nanoparticle tracking analysis would resolve the particles with the diameter up to 70 nm. In this case, the purity of exosomes would be criticalas these techniques also count protein aggregates in the sample.

Figure 1 shows the structure characterization of biomolecules depending on sizes. Traditionally optical microscope is used to resolve biomolecules with few hundred nanometers. To characterize nanometer sized molecules, TEM is commonly used. Another nanometer sized biomolecules, proteins can be resolved with x-ray crystallography and NMR. However in case of exosomes, we can only use TEM or AFM. The first structural characterization of exosomes was done by TEM with immuno-gold nanoparticle labeling [17]. Based on the EM images exosomes were thought to have 'cup-shaped structures'. However, AFM and field emission scanning

electron microscope (FESEM) images showed that exosomes are globular vesicles, similar to other vesicles in cells [18]. Recently, Gimzewski group was able to obtain high-resolution images of glioblastoma exosomes in the dry conditionmoreover,it showed interesting nanofilaments structure that might be involved in the delivery of exosomes into the recipient cells [19].

To establish the structural characteristics of exosomes, we have purified exosomes with two different method; one is using ultracentrifugation and the other is using magnetic beads that have selectivity to exosomes surface proteins. We have obtained high-resolution images of exosomes and observed the differences in the images depending on the purification method. Also, we have found nanofilaments that are purified with exosomes in both purification methods. Lastly, we have imaged exosomal nucleic acids. We discuss how these differences in exosome surface would affect future exosome studies.

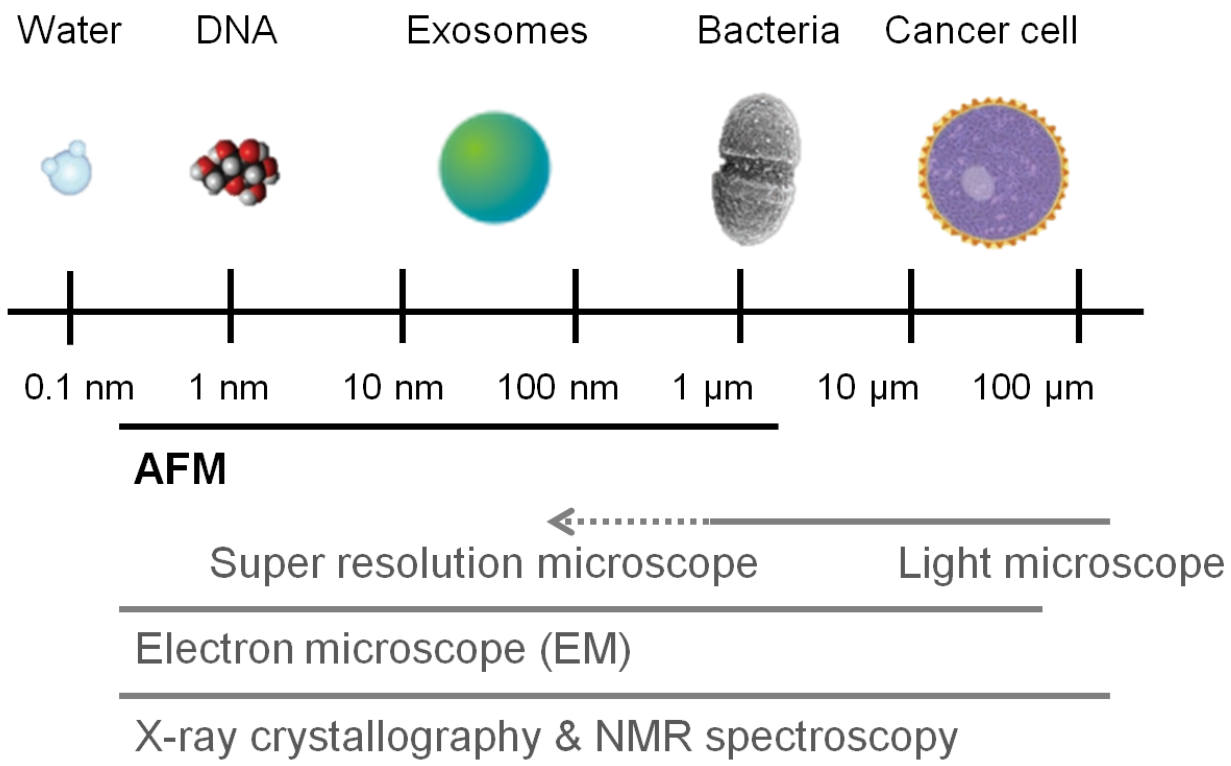

Figure 1. Nano-scale structural characterization of biomolecules. Various microscopy and spectroscopy techniques are utilized to characterize biomolecules. Each technique has a different resolution depending on size scales. AFM is capable of resolving nano-scale structure of exosomes.

7.3 Materials and Methods

U87 Cell Culture: U87 cells were cultured in Dulbecco's Modified Eagle Medium (DMEM) supplemented with 10% heat inactivated fatal bovine serum (FBS), 100 units/mL Penicillin G, and 100 µg/mL Streptomycin.Cells were incubated at 37°C and 5% carbon dioxide. At approximately 80% confluency, cells were washed with PBS and passaged using 0.25% trypsin-EDTA treatment for dissociation.

Exosome Isolation: U87 cells were cultured with FBS-originated-exosomes-free media for 48 hours and after 48 hours the media containing U87 exosomes was isolated.

Isolation of Exosomes using Antibody-Modified Magnetic BeadsKit Method: The procedure is followed by a manufacturer's manual (Figure 2) (JSR Life Science, Tokyo, Japan). 100 µL of media was incubated with 100 µL of capture beads for 60 min at room temperature (RT) on a shaker. Beads were able to be separated from the supernatant by a magnet and thus washed with 0.5mL wash buffer three times. 50 µL of elution buffer was added to the beads, and the beads were resuspended gently then incubated without mixing for 3 min at RT. Beads were separated, and the supernatant was transferred to a Slide-A-Lyzer™ Dialysis Cassette (Thermo Fisher Scientific, MA, USA) then dialyzed against PBS. Purified exosomes were storedat4 °C till AFM imaging.

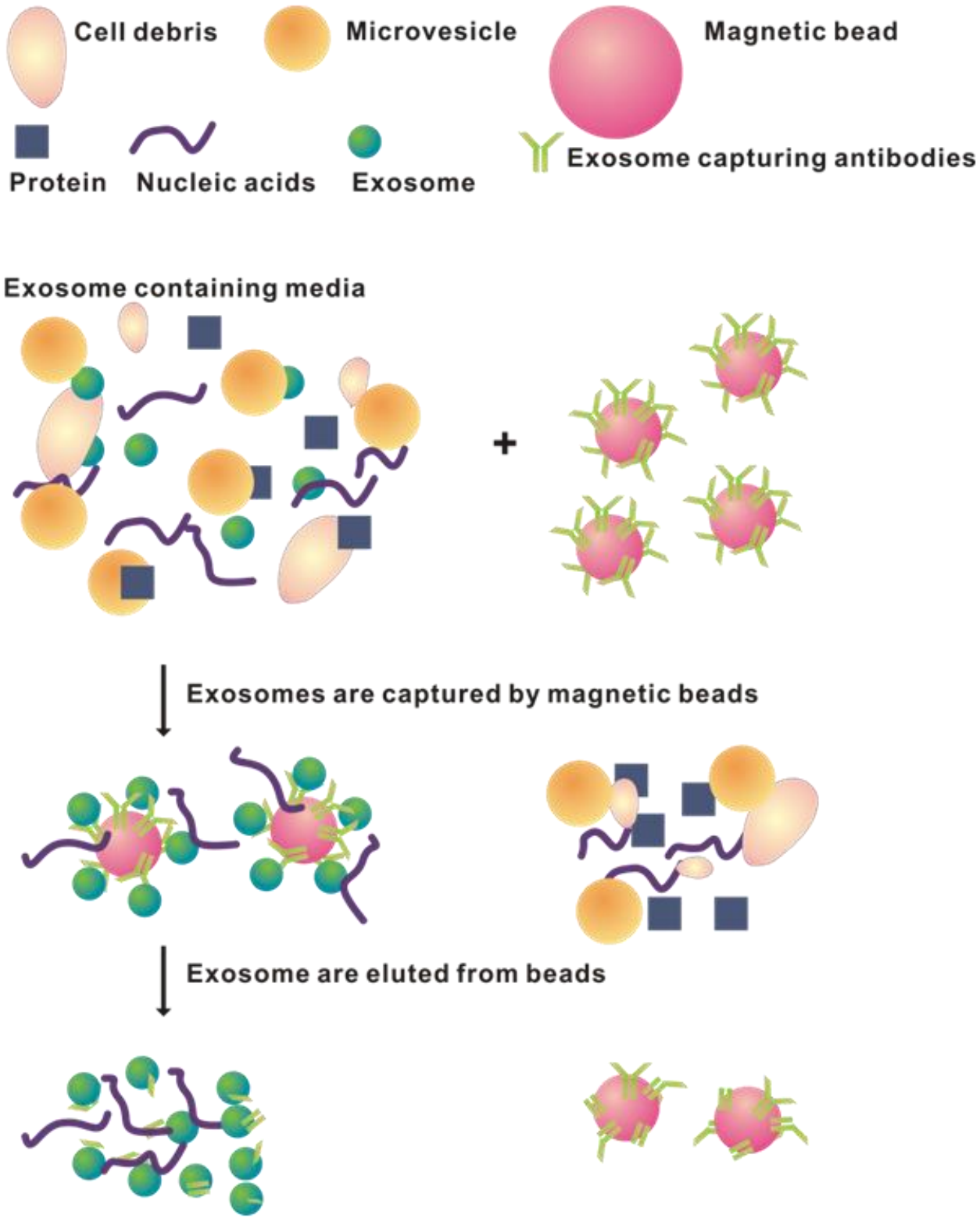

Figure 2. The schematic of exosome isolation by antibody-modified magnetic beads kit method.

Isolation of Exosomes using Ultracentrifugation Method: Exosome isolation using ultracentrifugation was followed by a previously published protocol (Figure 3) [12]. To remove cells/debris, the exosome containing media was centrifuged at 2,000g for 20 min at 4°C, and the supernatant 1 was isolated. Then the supernatant 1 was centrifuged at 10,000g for 30 min at 4°C to remove microvesicles and again the supernatant 2 was isolated carefully. To isolate exosomes, the supernatant 2 was ultracentrifuged at 100,000g for 2hours at4°C, and the supernatant 3 was discarded. To wash exosomes, the pellet was resuspendedin1 mL PBS and the mixture was ultracentrifugedat 100,000g for 1hour at4°C, and the supernatant 4 was discarded. Purified exosomes were resuspendedin100 µL of PBS and stored at 4°C till AFM imaging.

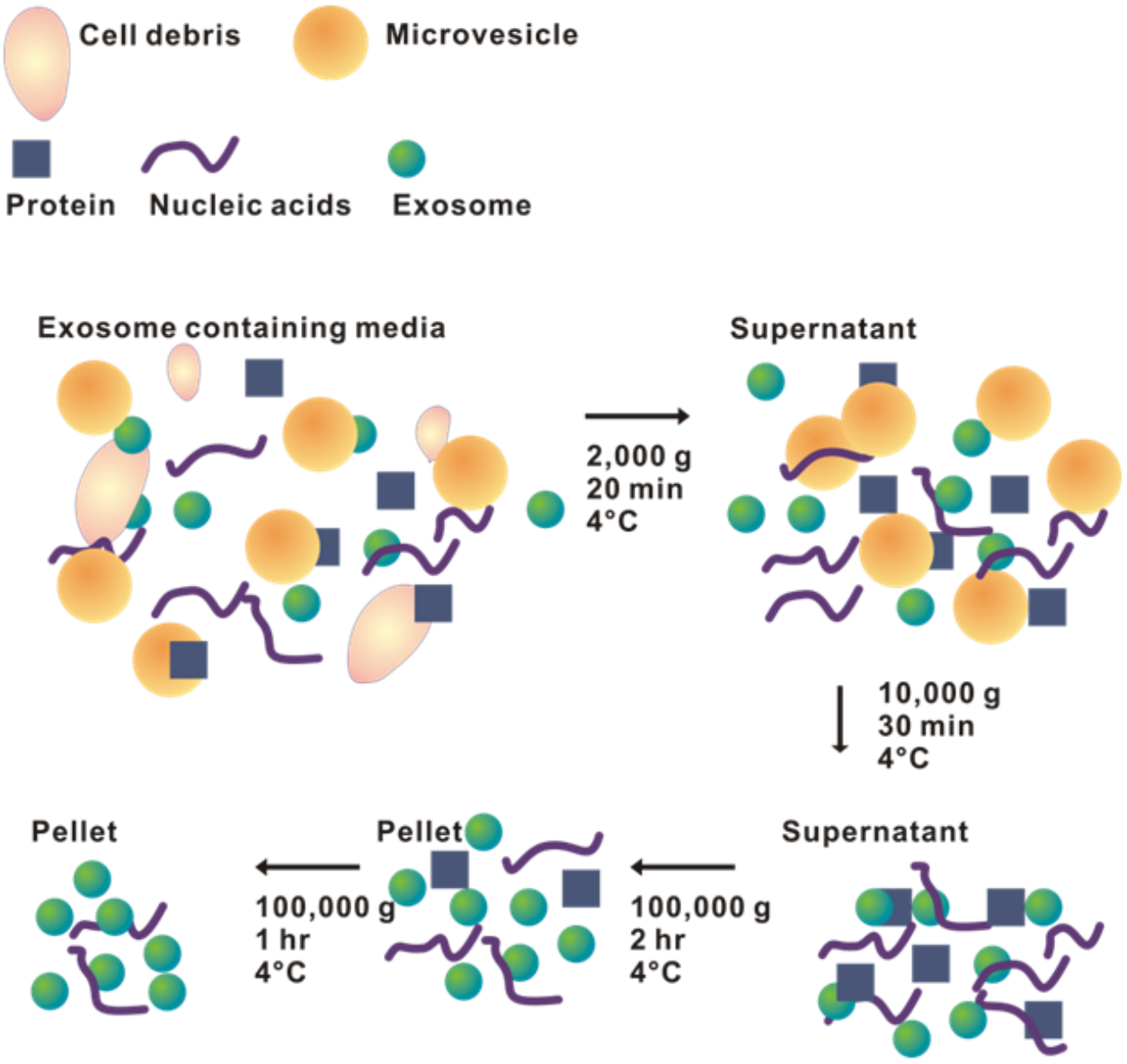

Figure 3.The schematic of exosome isolation by ultracentrifugation method.

Exosomal Nucleic Acid Purification: The procedure is followed by a manufacturer's manual (JSR Life Science, Tokyo, Japan). The manual contains three different purification methods, and (B) 2-step method was chosen. 100 µL of media was incubated with 100 µL of capture beads for 60 min at room temperature (RT) on a shaker. The supernatant was removed while a magnet detains the beads and 10 µL of Nucleic Acid Elution Buffer 1 with 240 µL of Nucleic Acid Elution Buffer 2 was added to the beads, and the mixture was vortexed and spun-down.150 µL of Nucleic Acid Elution Buffer 3 was added to the mixture and then it was vortexed thoroughly and spun-down. 2 µL of Nucleic Acid Elution Buffer 4 was added to each new microcentrifuge tube and the supernatant from the previous mixture was transferred to the tube containing Nucleic Acid Elution Buffer 4. 400 mL of 100% ethanol was added then vortexed and spun-down.The tube was incubatedat -20ºC for 20 min and centrifugedat 12,000 g for 10 min at 4ºC and then2µL of Nucleic Acid Elution Buffer 4 was added. 400 mL of 100% ethanol was additionally addedto the tube followed by vortexing and spinning-down. The tube was incubated at -20ºC for 20 min and centrifuged at 12,000 g for 10 min at 4ºC, and thenthe supernatant was aspirated carefully. The pellet was rinsed with 500 mL of ice-cold 70% ethanol and mixed then centrifugedat 12,000 g for 3 min at 4ºC, and then the supernatant was aspirated carefully. The pelletwas rinsed once again then the ethanol is completely removed. The pellet was resuspended in 10 µL of nuclease-free water.

Sample Preparation: Exosome samples purified from U87 were incubated on freshly cleaved mica for 5 min, washed with deionized water for 4 times to remove any unbound exosomes, and then air-dried overnight. Nucleic acids samples were diluted 1:10 ratio in 50 mM $MgCl_2$ 10 mM

Tris buffer (pH 8) and then incubated on freshly cleaved mica for 5 min, washed with deionized water for 4 times to remove any unbound nucleic acids, and then air-dried overnight.

AFM imaging: Samples were imaged by dimensionICON (Bruker Instruments, CA, USA) using tapping mode by TESP cantilever (Bruker Instruments, CA, USA) and images were recorded at 1024 samples per line at 1 Hz. Image processing was done using SPIP^{TM} software.

7.4 Result

Exosomes show different phase images depending on purification methods

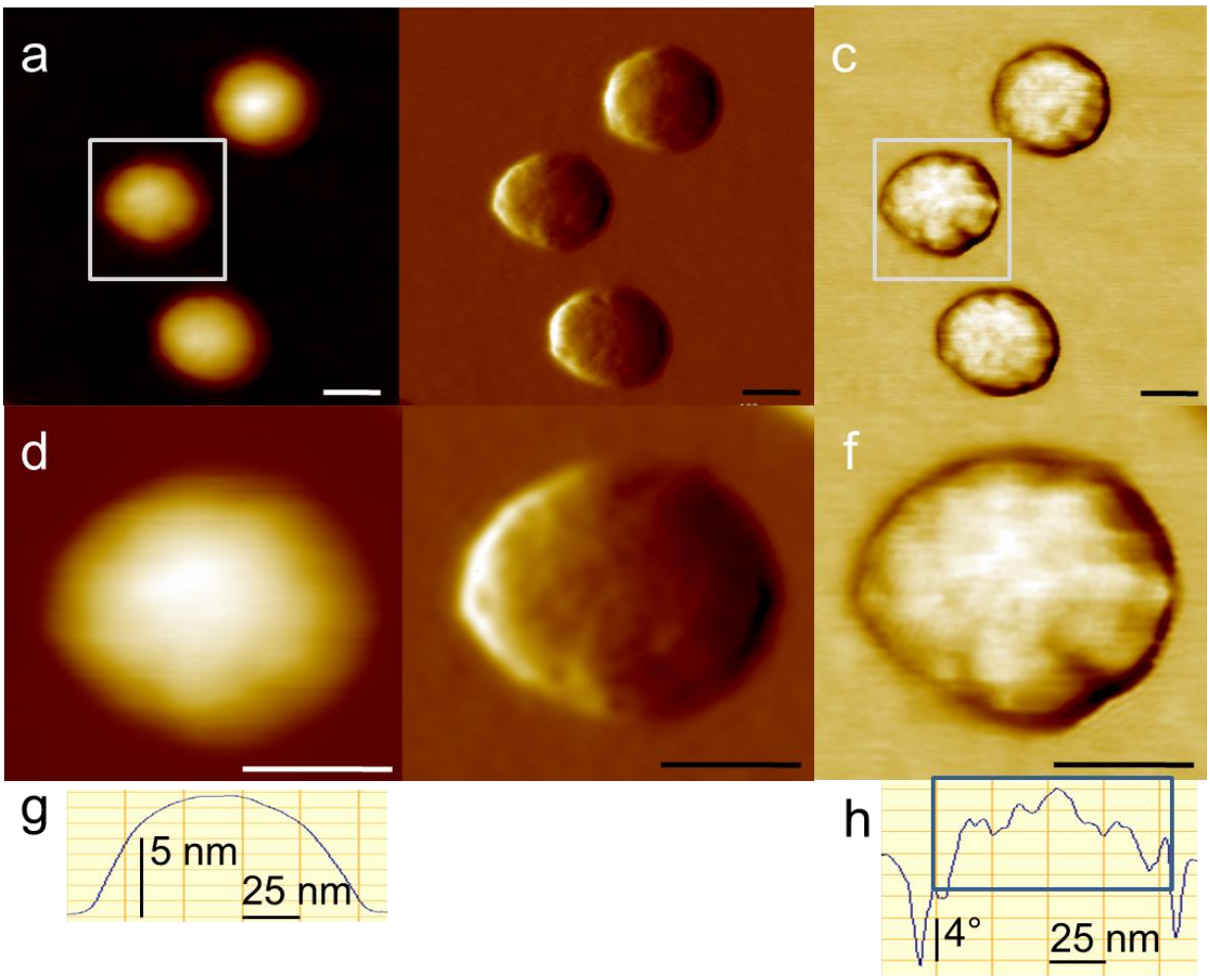

Figure 4. The high-resolution images of exosomes isolated by antibody-modified magnetic beads kit method. (a) Topography, (b) amplitude, and (c) phase images of exosomesare shown while the boxed exosome is magnified in (d) topography, (e) amplitude, and (f) phase images (Scale bar; 50 nm). (g) and (h) The cross-sections of (d) and (f), respectively.

We have isolated exosomes by antibody-modified magnetic beads kit method and resolved the high-resolution structure of exosomes. Figure 1 (a)-(c) shows the detailed image of exosomes. As confirmed in the previous publication [20], exosomes conveys a globular shape and the cross-section of topography agrees with it (Figure 1 (g)). One exosome is zoomed in Figure 1 (d)-(e) showing rough surfaces. We can observe the rough surface through phase image (Figure 1 (e)) most dramatically. In tapping mode AFM, phase image comes from the phage rag between incident resonant oscillations and the output signal oscillations that are altered by surface properties including elasticity, adhesion, and friction. The cross-section of the phage image shows the 1D roughness (see the box in Figure 1 (h)). Thus, the rough images indicate that exosome surfaces may be interrupted while the antibody-mediated isolation processes.

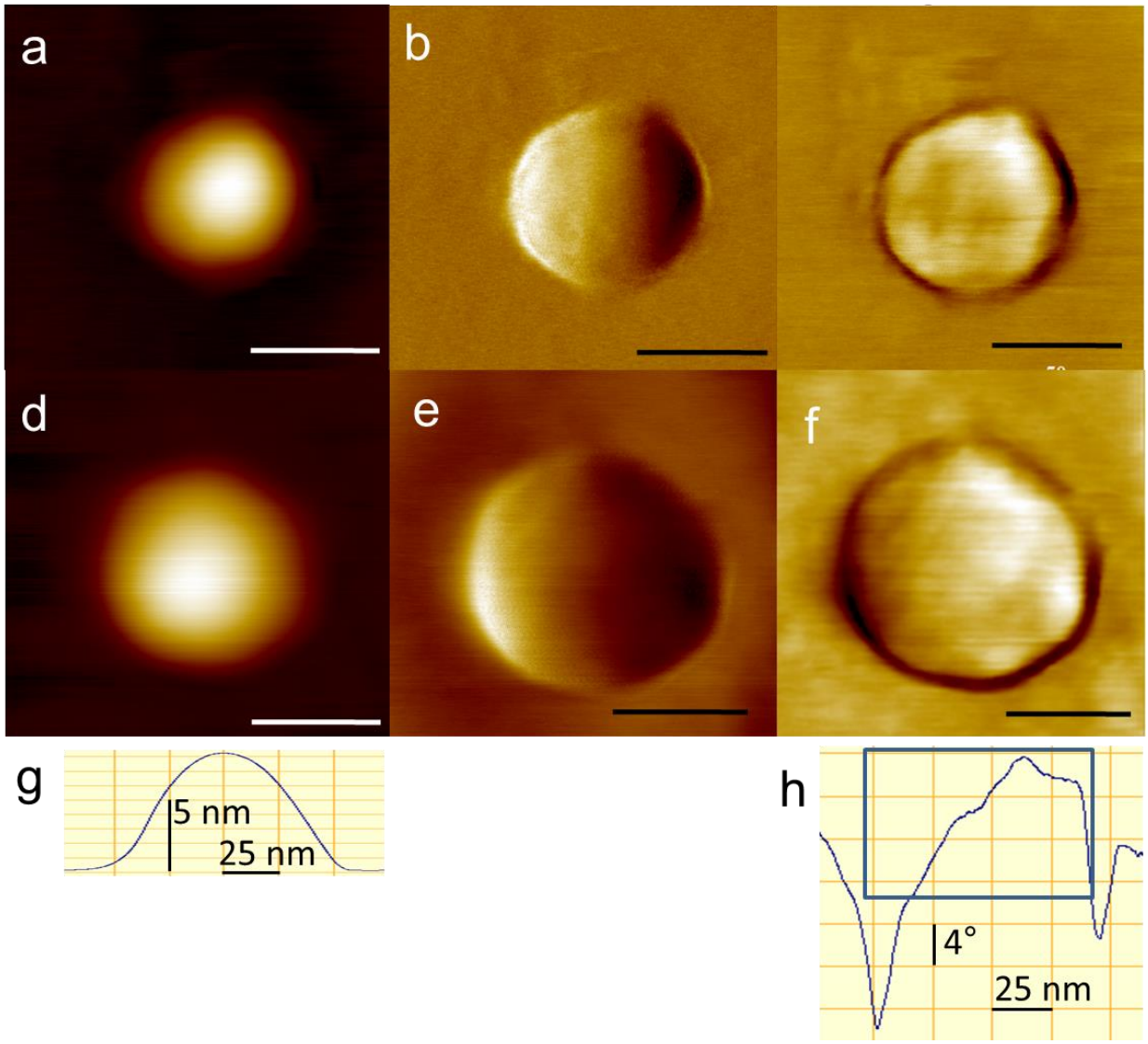

Figure 5. The high-resolution images of exosomes isolated ultracentrifugation method. (a),(d) Topography, (b),(e) amplitude, and (c),(f) phase images of exosomes are shown (scale bar; 50 nm). (g) and (h) The cross-section of (d) and (f), respectively.

We have isolated exosomes by ultracentrifugation method and resolved the high-resolution structure of exosomes as well. Figure 5 (a)-(f) shows the detailed image of two individual exosomes. Exosomes isolated by ultracentrifugation shows the same globular shape as well as the exosomes isolated by magnetic beads kit. We can observe the smooth surface of both exosomes. The phase images in Figure 5 (c) and (f) show the smoother surface compared to Figure 4 (c) and (f). The cross-section of the phage image also shows the smaller roughness (see the box in Figure 5 (h)). We could assume that the surface of exosomes is intact during the isolation.

Exosomes show different size distributions depending on purification methods

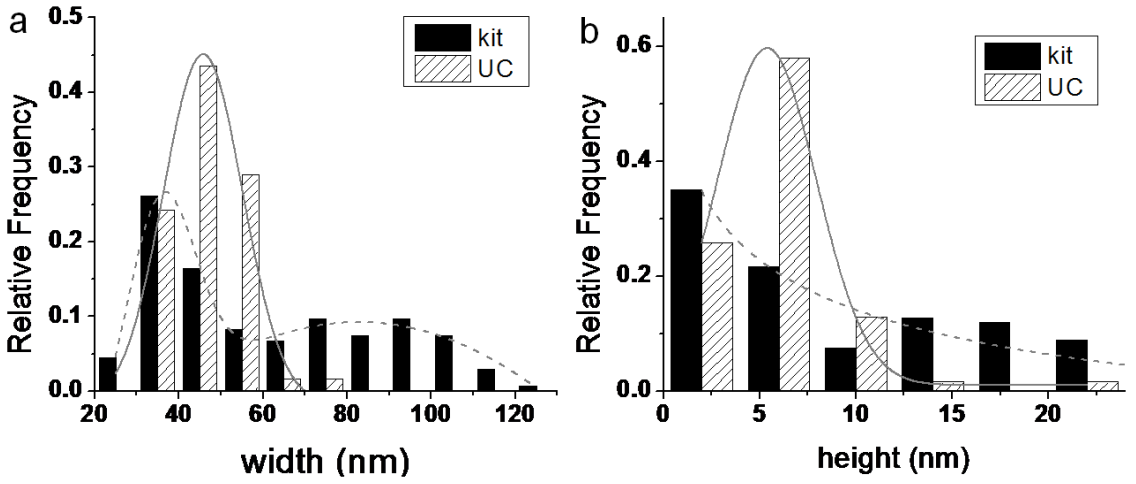

c	Width (nm)	Height (nm)
Exosomes isolated from magnetic beads kit	60.5 ± 26.2	9.55 ± 7.47
Exosomes isolated from ultracentrifugation	46.3 ± 8.4	5.99 ± 3.09

Figure 6. The size distributions of exosomes depending on isolation methods. The width distributions (a) and the height distributions (b) are shown with Gaussian fits. The exosomes isolated by magnetic beads kit show bimodal population while the exosomes isolated by ultracentrifuge show single Gaussian population. (c) The table shows average dimension of exosomes from each isolation method.

We have obtained the dimensions of exosomes (see figure 6) and both are matching with the previous size descriptions of exosomes [4, 13, 16]. More than 50 exosomes were measured in 1 μm x 1 μm images with 512 resolution. The exosomes isolated from the magnetic beads kit shows wider bimodal distributions and higher dimension compared to the exosomes isolated from ultracentrifugation. In case of ultracentrifugation, exosomes are isolated by the density and it shows relatively narrow singular distributions.

Nanofilaments found with purified exosomes

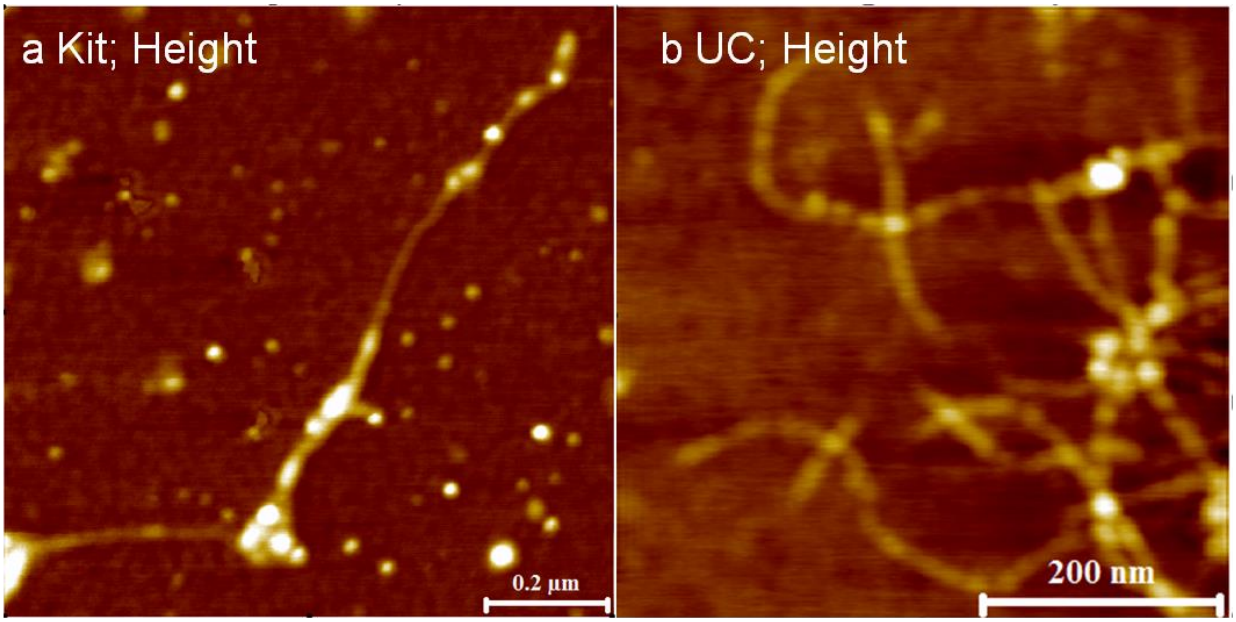

C

Method	Filament Width	Filament Height
Magnetic beads kit	32 ± 3 nm	0.75 ± 0.17 nm
Ultracentrifuge (UC)	23 ± 4 nm	0.66 ± 0.18 nm

Figure 7. Nanofilaments are found with exosomes regardless of purification methods. Topography images of nanofilaments by (a) antibody-modified magnetic beads kit method and (b) ultracentrifuge method. (c) Nanofilaments have similar dimensions.

We could confirm the existence of nanofilaments with exosomes again as described in chapter 6. Figure 7 shows the nanofilaments are found in both purification methods (a) and (b) and the dimensions of nanofilaments are similar to each other (c).

7.5 Discussions and Future Directions

In this chapter, we have revealed that the surface characteristics of exosomes are different depending on the purification methods. Exosomes purified from magnetic beads showed a rougher surface compared to exosomes purified from ultracentrifugation. Since the manufacturer is not disclosing the composition of the exosome elution buffer we cannot identify the components affecting the exosome surface. It is possible that the antibodies are stuck on the exosome surface or surfactants for the magnetic beads are transferred to the exosomes. In either case, we may not select this method when the intact surface is important in studying exosomes. Exosomes purified from ultracentrifugation showed a smoother surface. Also it showed different size distributions depending on the purification methods. In case of the magnetic beads purification method, we observed the wider bimodal distribution of exosome dimensions both width and height. The antibodies on the magnetic beads are against four different antigens CD9, CD63, CD81, and EpCAM. Since the antibodies are selecting the exosomes by the surface proteins, it is possible that exosomes with certain size and surface marker are purified from the whole exosome class. On the other hand, ultracentrifuge utilizes the density difference in the sample to purify exosomes. Exosomes from ultracentrifugation showed single Gaussian fit of width and height distributions.

Characterization of Exosomal Nucleic Acids

We have observed the nanofilaments with exosomes purified from both methods. To identify the nanofilament, we treated the exosomes with trypsin and the nanofilaments are not digested upon a trypsin treatment (see chapter 6) [19]. Table 1 shows the one dimensional filaments present in cells and their heights and widths under AFM imaging. Based on the table 1, the nanofilaments have similar dimensions to the nucleic acids. In the characterization of exosomes, we purified the exosomal nucleic acids and obtained the high-resolution images of them. Figure 8 shows the nucleic acids (b) the long nucleic acids and (c) short nucleic acids. It is notable that the dimensions of nucleic acids (d) are again similar to those of nanofilaments (Figure 7 (c)). Now we have a hypothesis that the nanofilaments are nucleic acids from exosomes. To verify it, we will conduct a DNAse/RNAse treatment on exosome samples. It would be clearer when we have a zinc-finger protein modified with gold nanoparticles. The zinc-finger protein will bind to nanofilaments if they are actually nucleic acids [21].

Table 1. One dimensional filaments found in cells and their dimensions under AFM images.

Filament type	Dimensions under AFM imaging	Reference
dsDNAs	Height; 0.68 ± 0.05 nm Width; 25.2 ± 5.5 nm	Liu et al. [22]
	Height; 0.7 ± 0.1 nm Width; 12 ± 3 nm	Adamcik et al. [23]
ssDNAs	Height; 0.3 ± 0.1 nm Width; 7 ± 2 nm	Adamcik et al. [23]
	Heights; 0.25 to 0.4 nm	Woolley et al. [24]
RNAs	'Kissing-loop' RNAs Height; 1.2 ± 0.2 nm TectoRNAs Height; 0.9 ± 0.1 nm Full width at half maximum (FWHM); 21 ± 4 nm	Hansma et al. [25]
	Heights; 1 to 1.5 nm	Kienberger et al. [26]
Actin filaments	Height; 2 nm Width; 20 nm	Sharma et al. [27]
Microtubules	Height; 11 ±2 nm Width; 80 ± 20 nm	Vinckier et al. [28]
	Height; 25 nm	Wagner et al. [29]
Intermediate filaments	Vimentin IF (2 morphologies) Heights; 0.8 nm and 1.7 nm FWHM; 100 nm and 45 nm	Mucke et al. [30]
Amyloids	Heights; 2, 4 and 6 nm	Adamcik et al. [31]
	Heights; 4 nm	Dahlgren et al. [32]

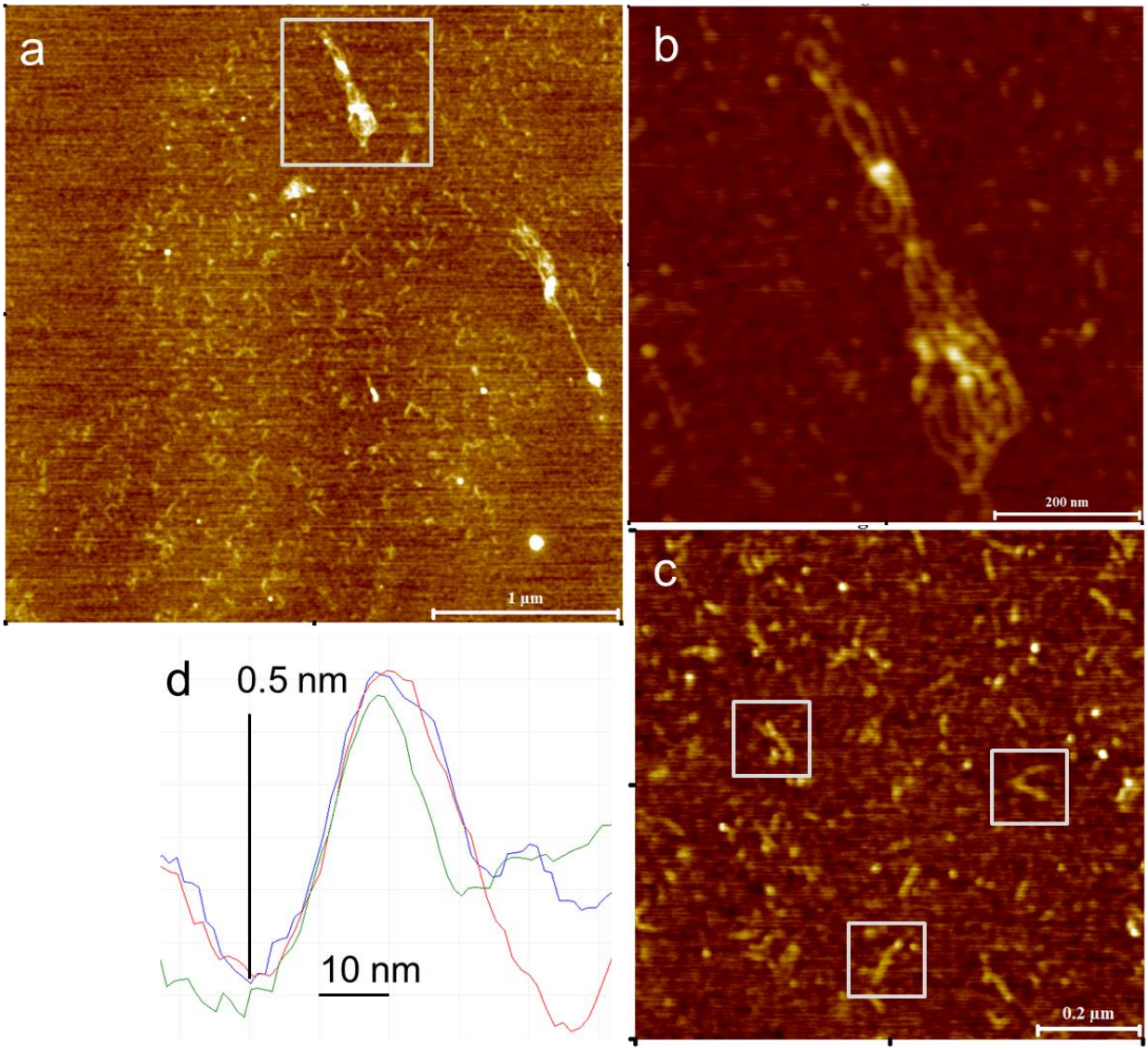

Figure 8. The high-resolution images of purified exosomal nucleic acids. (a) Topography of purified exosomal nucleic acids while a long nucleic acid (a gray box in (a)) is zoomed in (b) and short nucleic acids are zoomed in (c). (d) The cross-section indicates the dimensions of short nucleic acids (boxed in (c)).

7.6 References

1. Bang, C. and T. Thum, *Exosomes: new players in cell-cell communication.*Int J Biochem Cell Biol, 2012. **44**(11): p. 2060-4.
2. Bobrie, A., et al., *Exosome secretion: molecular mechanisms and roles in immune responses.* Traffic, 2011. **12**(12): p. 1659-68.
3. Camussi, G., et al., *Exosomes/microvesicles as a mechanism of cell-to-cell communication.* Kidney Int, 2010. **78**(9): p. 838-48.
4. Ludwig, A.K. and B. Giebel, *Exosomes: small vesicles participating in intercellular communication.*Int J Biochem Cell Biol, 2012. **44**(1): p. 11-5.
5. Laulagnier, K., et al., *Mast cell- and dendritic cell-derived exosomes display a specific lipid composition and an unusual membrane organization.*Biochem J, 2004. **380**(Pt 1): p. 161-71.
6. Azmi, A.S., B. Bao, and F.H. Sarkar, *Exosomes in cancer development, metastasis, and drug resistance: a comprehensive review.* Cancer Metastasis Rev, 2013.
7. Yu, X., S.L. Harris, and A.J. Levine, *The regulation of exosome secretion: a novel function of the p53 protein.* Cancer Res, 2006. **66**(9): p. 4795-801.
8. Safaei, R., et al., *Abnormal lysosomal trafficking and enhanced exosomal export of cisplatin in drug-resistant human ovarian carcinoma cells.*Mol Cancer Ther, 2005. **4**(10): p. 1595-604.
9. Valadi, H., et al., *Exosome-mediated transfer of mRNAs and microRNAs is a novel mechanism of genetic exchange between cells.* Nat Cell Biol, 2007. **9**(6): p. 654-9.
10. Skog, J., et al., *Glioblastoma microvesicles transport RNA and proteins that promote tumour growth and provide diagnostic biomarkers.* Nat Cell Biol, 2008. **10**(12): p. 1470-6.
11. Witwer, K.W., et al., *Standardization of sample collection, isolation and analysis methods in extracellular vesicle research.* J Extracell Vesicles, 2013. **2**.
12. Thery, C., et al., *Isolation and characterization of exosomes from cell culture supernatants and biological fluids.*CurrProtoc Cell Biol, 2006. **Chapter 3**: p. Unit 3 22.

13. Tauro, B.J., et al., *Comparison of ultracentrifugation, density gradient separation, and immunoaffinity capture methods for isolating human colon cancer cell line LIM1863-derived exosomes.* Methods, 2012. **56**(2): p. 293-304.

14. Boing, A.N., et al., *Single-step isolation of extracellular vesicles by size-exclusion chromatography.* J Extracell Vesicles, 2014. **3**.

15. Oksvold, M.P., A. Neurauter, and K.W. Pedersen, *Magnetic bead-based isolation of exosomes.* Methods MolBiol, 2015. **1218**: p. 465-81.

16. van der Pol, E., et al., *Particle size distribution of exosomes and microvesicles determined by transmission electron microscopy, flow cytometry, nanoparticle tracking analysis, and resistive pulse sensing.* Journal of Thrombosis and Haemostasis, 2014. **12**(7): p. 1182-1192.

17. Pan, B.T., et al., *Electron microscopic evidence for externalization of the transferrin receptor in vesicular form in sheep reticulocytes.* J Cell Biol, 1985. **101**(3): p. 942-8.

18. Sharma, S., et al., *Structural-mechanical characterization of nanoparticle exosomes in human saliva, using correlative AFM, FESEM, and force spectroscopy.* ACS Nano, 2010. **4**(4): p. 1921-6.

19. Sharma, S., et al., *Nanofilaments on glioblastoma exosomes revealed by peak force microscopy.* J R Soc Interface, 2014. **11**(92): p. 20131150.

20. Sharma, S., et al., *Nanofilaments on glioblastoma exosomes revealed by peak force microscopy.* Journal of the Royal Society Interface, 2014. **11**(92).

21. Klug, A. and D. Rhodes, *Zinc Fingers - a Novel Protein Motif for Nucleic-Acid Recognition.* Trends BiochemSci, 1987. **12**(12): p. 464-469.

22. Liu, Z., et al., *Imaging DNA molecules on mica surface by atomic force microscopy in air and in liquid.*Microsc Res Tech, 2005. **66**(4): p. 179-85.

23. Adamcik, J., et al., *Observation of single-stranded DNA on mica and highly oriented pyrolytic graphite by atomic force microscopy.* FEBS Lett, 2006. **580**(24): p. 5671-5.

24. Woolley, A.T. and R.T. Kelly, *Deposition and characterization of extended single-stranded DNA molecules on surfaces.* Nano Letters, 2001. **1**(7): p. 345-348.

25. Hansma, H.G., et al., *TectoRNA and 'kissing-loop' RNA: atomic force microscopy of self-assembling RNA structures.* Journal of Microscopy-Oxford, 2003. **212**: p. 273-279.

26. Kienberger, F., et al., *Monitoring RNA release from human rhinovirus by dynamic force microscopy.* J Virol, 2004. **78**(7): p. 3203-3209.

27. Sharma, S., et al., *Atomic force microscopy reveals drebrin induced remodeling of f-actin with subnanometer resolution.* Nano Lett, 2011. **11**(2): p. 825-7.

28. Vinckier, A., et al., *Dynamical and mechanical study of immobilized microtubules with atomic force microscopy.* Journal of Vacuum Science & Technology B, 1996. **14**(2): p. 1427-1431.

29. Wagner, O.I., et al., *The interaction of neurofilaments with the microtubule motor cytoplasmic dynein.* Molecular Biology of the Cell, 2004. **15**(11): p. 5092-5100.

30. Mucke, N., et al., *Assessing the flexibility of intermediate filaments by atomic force microscopy.* J MolBiol, 2004. **335**(5): p. 1241-1250.

31. Adamcik, J., et al., *Understanding amyloid aggregation by statistical analysis of atomic force microscopy images.* Nature Nanotechnology, 2010. **5**(6): p. 423-428.

32. Dahlgren, K.N., et al., *Oligomeric and fibrillar species of amyloid-beta peptides differentially affect neuronal viability.* Journal of Biological Chemistry, 2002. **277**(35): p. 32046-32053.

Chapter 8.

Nanostructured Self-Assembly of Inverted Formin 2 (INF2) and F-Actin–INF2 Complexes Revealed by Atomic Force Microscopy

8.1 Abstract

Self-organization of cytoskeletal proteins such as actin and tubulin into filaments and microtubules is frequently assisted by the proteins binding to them. Formins are actin regulatory proteins, which nucleate the formation of new filaments and are essential for a wide range of cellular functions. The vertebrate Inverted Formin 2 (INF2) has both actin filament nucleating, severing, and depolymerizing activities connected to its ability to encircle actin filaments. Using atomic force microscopy (AFM), we report that an FH2 domain-containing construct of INF2 (INF2-FH1-FH2-C or INF2-FFC) self assembles into nanoscale ring-like oligomeric structures in the absence of actin filaments, demonstrating an inherent ability to re-organize from a dimeric to an oligomeric state. A construct lacking the C-terminal region (INF2-FH1-FH2 or INF2-FF) also oligomerizes, confirming dominant role of FH2-mediated interactions. Moreover, INF2-FFC domains were observed to organize into ring like structures around single actin filaments. This is the first demonstration that formin FH2 domains can self-assemble into oligomers in the absence of filaments, and has important implications for observing un-averaged decoration and/or remodeling of filaments by actin binding proteins.

8.2 Introduction

Self-assembly and regulated assembly of proteins into nanostructures is ubiquitous in biology and disease and is among the most intriguing features of biological systems [1]. Proteins may assemble to form various nanostructures like nanotubes, vesicles, helical ribbons, filaments, and fibrous scaffolds. Some well-known examples of such assembly include cytoskeletal filaments such as actin and tubulin [2] amyloid fibril formation [3-4] chromatin assembly [5] and phospholipid [6] membrane self-assembly. Intriguingly, some of the protein regulators of cytoskeletal filaments can also form higher order assembly structures. The morphology and function of these structures are yet to be elucidated. Some examples of such self-assembly are actin-binding proteins tropomyosin and drebrin that can form oligomeric structures *in vivo*. Oligomers of tropomyosin have been shown to be isoform specific and their level is drastically altered in malignant tumor cells [7]. Drebrin was also shown to form higher order oligomers named drebrosomes [8-9]. It was hypothesized that such structures allowed for maintaining high local concentration of these regulatory proteins in the needed regions in cells.

Focusing on the actin-based elements of cytoskeleton, the *in vitro* studies of self-assembly of purified actin alone - and in complex with actin binding proteins - offer a simple route to understanding how these proteins interact and function under controlled conditions. To this end, complementary experimental methods such as electron microscopy, cryo-electron microscopy (cryo-EM), and fluorescence microscopy have been extensively used to study the assembly and disassembly processes with actin-binding proteins and the structures of the assembled complexes. Total Internal Reflection Fluorescence (TIRF) microscopy has emerged as an important method for visualizing single molecules and single filaments [10]. TIRF has been used

to study actin polymerization time course [10], kinetics of filament barbed end capping [11] and processive growth mediated by formins [12-13]. Yet, it can provide only limited structural information, within the resolution of the TRIF field (<200 nm). In the cryo-EM area there have been recent advances in near atomic resolution analysis of protein structures by single particle electron microscopy, using direct electron sensing cameras [14]. However, large datasets of molecules captured in random orientations are needed for their frequently complex structural analysis. In the case of actin filaments the averaging of data does not shed light on the heterogeneity of individual filaments or their segments, nor on the local changes in their twist [15].

Though still a relatively new application to the study of actin binding proteins and F-actin, Atomic Force Microscopy (AFM) [16] is a powerful technique for nanoscale characterization of biological structures [17-23]. It offers unique capability for direct 3D imaging of single actin filaments without electron dense staining, fixation, or extreme temperatures, and with imaging resolution comparable to that of negatively stained electron microscopy samples. Several proteins and protein conformational changes have been investigated at sub-molecular resolution using AFM. AFM imaging does not suffer from diffraction limits, and allows exceptionally high signal-to-noise sub-nanometer lateral resolution and vertical resolution of up to 1 Å [20, 24-26]. Among biomolecules, membrane proteins in their native state have been imaged most extensively [20, 26]. Besides isolated viruses and phages [27-28], specific substructures like viral capsomeres, bacteriophage connectors and tails [29-30] have been imaged at a resolution comparable to EM. AFM has been used successfully also to image high resolution structures of F-actin [31] and the structure of F-actin complexes with its binding proteins, such as drebrin and

cofilin [32]. This method can reveal the structural heterogeneity of filament populations as well as analyze local changes in segments of individual filaments.

In the present work, we apply AFM imaging to study *in vitro* the self-assembly of formin and its complexes with F-actin. Formins are actin assembly proteins that play essential roles in fundamental cellular processes such as polarity, adhesion, and cytokinesis [33-35]. The actin regulatory activity of formins is mediated through the conserved Formin Homology 2 (FH2) domain [36-38]. Formins exert multiple effects on actin polymerization *in vitro* (nucleation, elongation, and anti-capping) mediated through the activity of FH2 domain [37]. The vertebrate-specific Inverted Formin 2 (INF2) has the additional ability to sever filaments [39-40] which involves both the FH2 domain and an actin monomer-binding motif in its C-terminus.

Structurally, the ~400 amino acid FH2 domain is a donut-shaped head-to-tail dimeric structure consisting of two rigid hemi-spherical halves connected by a flexible linker [36, 41-43]. The FH2 dimer is very stable in some formins, but has the ability to dissociate in others [44-45]. Formin FH2 domains remain bound to actin filament barbed ends during filament elongation, moving processively as new actin monomers add through a "stair-stepping" mechanism, although the exact sequence of steps remains in debate [36, 38, 42, 46]. It is predicted that the donut shaped FH2 dimer (~11 nm diameter) partially encircles the 7 nm diameter barbed end, without the individual domains needing to dissociate and re-associate. In addition to barbed end binding, INF2 has the ability to bind filament sides. Side binding is accomplished by FH2 domain encirclement of the filament, wherein the FH2 adopts similar binding interactions as those used at the barbed end. To accomplish this feat, the FH2 domain presumably must dissociate from its

dimeric state, since the alternative mechanism of sliding along several micrometers of filament is unlikely. However, the ability of any FH2 dimer to dissociate and recombine has not been observed directly.

As an approach to better understand FH2 homodimer actin regulatory function and to overcome the existing limitations of structure determination, we obtained the structure of INF2-FH1-FH2-C (INF2-FFC) (Figure 1) alone and in complex with single actin filaments. We present the first nanoscale structure and self-organization of INF2 alone and the side binding structure of INF2 in complex with actin filaments at the single filament level using tapping mode AFM imaging.

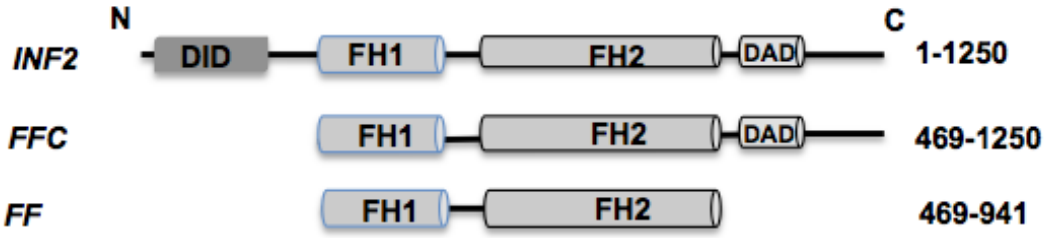

Figure 1. Schematic representation of domain organization of Inverted Formin 2 (INF2) showing regions important for actin binding and protein-protein interactions. Formin constructs used in this study include INF2-FH1-FH2-C, also termed as INF2-FFC, and INF2-FH1-FH2 or INF2-FF. N and C denote the N- or the C-terminus of protein sequences. Other symbols are: DID, the diaphanous inhibitory domain; FH1, formin homology 1; FH2, formin homology 2; and DAD, diaphanous autoregulatory domain.

8.3 Materials and Methods

Protein preparation: Skeletal actin was purified according to Spudich and Watt [47]. Human INF2-FFC (amino acids 469-1249) and INF2-FF (469-941) constructs were expressed and purified as previously described [39]. Rabbit skeletal Ca-ATP-G-actin was converted to Mg-ATP-G-actin by incubating it with 0.4 mM EGTA and 50 μM $MgCl_2$ for 3 min at RT, and then polymerized by addition of 10x KMEH buffer (final concentrations: 50 mM KCl, 1 mM $MgCl_2$, 0.4 mM EGTA, 10 mM HEPES, pH 7). Final F-actin preparation contained also 0.2 mM ATP, 1 mM DTT, and was supplemented with phalloidin (1:1 molar ratio) and 10 – 25 mM phosphate. INF2 constructs were dialyzed overnight into 1x KMEH buffer, pH 7, and then pre-spun at 4°C in TLA100 rotor, for 20 min at 80,000 rpm, to remove any aggregates. Protein concentration was measured by Bradford assay.

AFM imaging of formin and actin-formin complexes: 5.0 μL of different concentrations of formin solutions in buffer were added to freshly cleaved mica, incubated for 1 min and gently rinsed with dilution buffer three times (to remove unbound actins and proteins) and allowed to air dry overnight. In case of formin-actin complexes, formin was allowed to bind F-actin in solution. 5.0 μL of the solution was added to freshly cleaved mica substrates, incubated for 1min and gently rinsed with dilution buffer three times (to remove unbound actin and protein) and allowed to air dry. Dimension 5000 AFM (Bruker Scientific) under tapping mode was used to image formin and actin-formin complexes with OTESP probes (Bruker Scientific). Topographic height images were recorded at 1024x1024 pixels at 1Hz. SPIP was used for image processing which includes zero order flattening and band pass filtering. While sample air-drying and AFM tip may result in flattening of the structures, the dimeric formin rings are consistent with overall

structures of the INF2 molecules measured by other independent techniques reported previously linker [36, 41-43]. Corresponding ring like structures were observed around polymerized actin filaments as well, which adds further evidence of lack of denaturation. Additionally, we previously confirmed [32] that helical pitch of bare F-actin as well as cofilin-decorated filaments measured by AFM (under our conditions) was in excellent agreement with the EM-based measurements, validating our assumption that F-actin filaments under ambient AFM imaging conditions are not denatured.

8.4 Results and Discussion

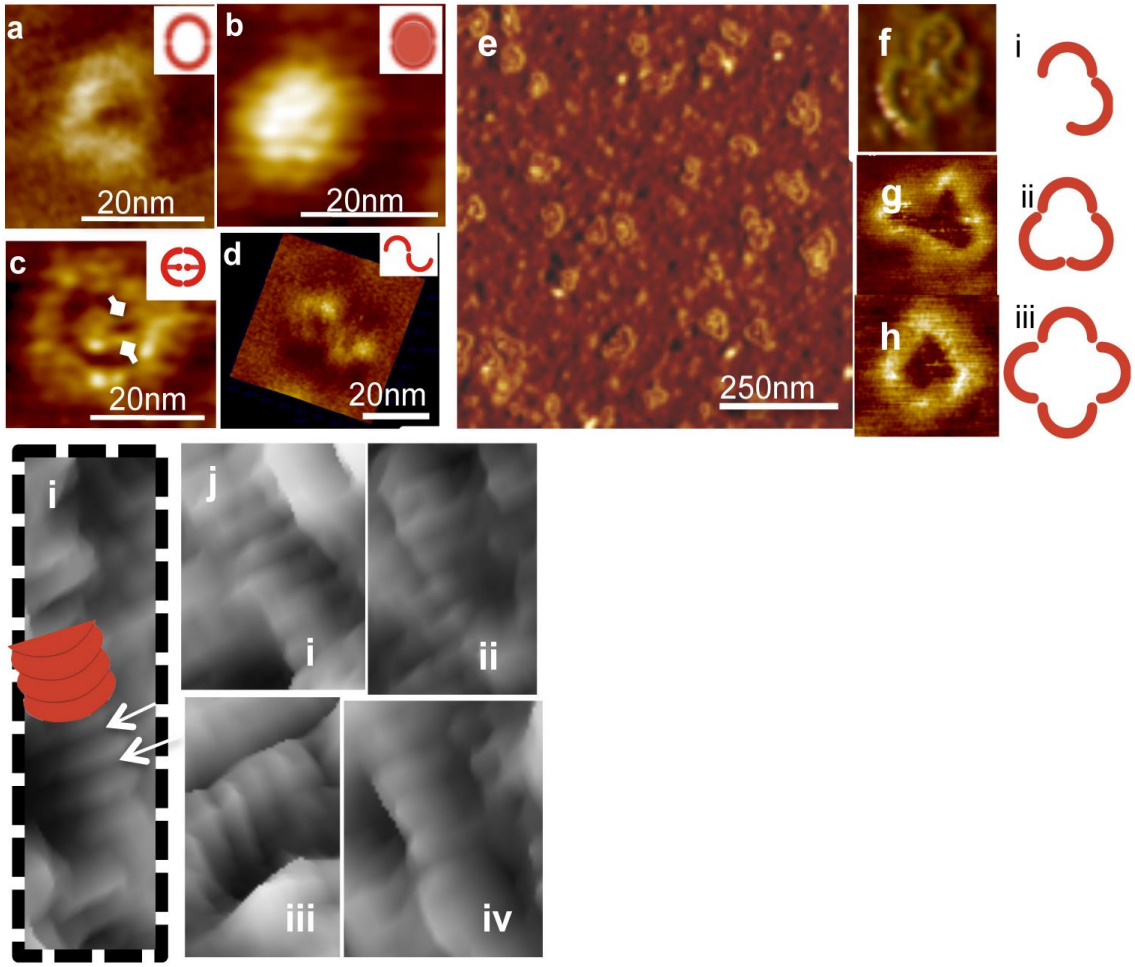

Figure 2. Structural evidence of self-assembly of INF2-FFC at various concentrations. At low concentrations (0.02 μM), INF2-FFC forms ring shaped homodimers. Representative AFM images of free INF2-FFC showing self-assembled round structures likely formed by dimerization of FH2 domains of INF2-FFC. Schematic representations are in the insets. (a) Single INF2-FFC dimer. (b) Compact and closed round dimers were observed also without hollow core. (c) The central core region attached to dimeric ring periphery via two small extensions (diamond arrows), corresponds potentially to the unstructured FH1 domain. (d) An example of INF2-FFC dimer in open configuration. The FH2 domain within INF2-FFC dimer can potentially disassociate (open) and re-associate (close) to form trimers as well as oligomers (at higher surface concentrations (0.2 μM)). (e) AFM image of INF2-FFC in oligomeric configurations (0.2 μM INF2-FFC). Representative images of INF2-FFC dimer, trimers, and tetramer (f-h) and their corresponding schematic representations (i), (ii), and (iii). At higher concentrations (2 μM) INF2-FFC assembles into tubular ring-like structures, as marked with white arrow in (i). Other zoom in views are shown in (j) i to iv.

Structure of free INF2-FFC homodimers and oligomers

FH2 domain dimerization has been proposed to be essential for the actin polymerization activity of formins [41, 44, 48-49]. Yet, there are several gaps in our current understanding of the assembly and actin regulation via FH2 dimerization. Crystal structures of yeast Bni1 FH2 domain [36] and mammalian formin FH2 domains [42-43, 50] indicate that the two monomers are connected by flexible tethers to form a dimeric "ring". Some of these FH2 dimers, such as in FMNL1 and mDia2, appear to be able to dissociate and re-associate [45]. In addition, the apparently stable Bni1p FH2 can also assemble into oligomers [36] around non-helical actin structures. Other formins appear strictly dimeric. For example, despite containing two different dimerization domains (the N-terminal DD and the C-terminal FH2), mDia1-FL does not form higher order oligomers but remains as dimers in the extended/activated and closed/autoinhibited states [51].

INF2's FH2 domain has been shown to bind actin filament sides through a mechanism by which its dimer dissociates [40]. There are two possible modes by which INF2 FH2 domain might bind actin filaments in this manner. The individual FH2 dimers may re-form dimeric "rings" around F-actin but not associate with each other (Figure 6). Alternatively, FH2s may re-bind the filament in a circular pattern, with oligomerization (Figure 6) occurring through the FH2 dimerization sites, similar to the crystal structure of Bni1p FH2 bound to actin [36]. To differentiate between these two topologically distinct binding modes *i.e.*, dimeric rings or circular spirals over F-actin (Figure 6), we explored the structural characteristics of INF2-FFC alone to test if it could assemble into high order oligomers. We obtained AFM 3D images of free INF2-FFC constructs over freshly cleaved mica substrates at varying protein concentrations. At

low concentrations (0.02 μM), isolated donut-shaped dimers were observed, either in hollow "open" or "closed" conformations (Figure 2). The two conformations - either hollow "open" (Figure 2a,c,d) or "closed" (Figure 2b), are consistent with cryo-EM structures of full-length formin mDia1 showing two distinct open and closed structures [51]. Compared to ~10 nm for crystal structure of Bni1p FH2 domain [41], our AFM images showed diameters of 22 ± 0.1 nm (closed ring) and 27 ± 0.4 nm (open ring). The apparent increase in the width of the formin molecules in AFM images is likely the result of AFM tip broadening effect as well as the interactions of the protein with mica surfaces.

Table 1. AFM measurements of free INF2-FFC and INF2-FF self-assembly

Formin assembly	**INF2-FFC**			**INF2-FF**	
Concentration	0.02 μM	0.2 μM	2 μM	0.02 μM	0.2 μM
Organization	dimers	oligomers	oligomers or stacked dimers	dimers	oligomers
Width (nm)	22 ± 0.1 (closed) 27 ± 0.4 (open)	45 ± 2 up to 54.6 ± 0.8	-	22 ± 0.1 (closed) 26 ± 1.6 (open)	44 ± 1 up to 56 ± 2
Cross-section height (nm)	0.2	0.3	0.3 or more	0.2	0.3

At higher protein concentrations (0.2 μM), oligomers were observed that were similar in height to dimers (0.3 nm) but larger in diameters. Representative images in Figure 2e-h display free INF2-FFC forming trimers, tetramers, and larger oligomers. The mean diameters of these oligomers were measured as 45 ± 2 nm (trimers) and 54.6 ± 0.8 nm (tetramers) (Table 1). Similar cross sectional height profiles (0.2 nm) of dimers as well as tetramers preclude possible aggregation. The self-organizing ability of free INF2-FFC construct is further exemplified in case of higher (10-fold) protein concentrations adsorbed over mica substrates. At 2 μM concentrations, large aggregates of INF2-FFC were observed. Most notably, stacked tube-like structures likely formed by stacking of dis-associated and then re-assembled INF2-FFC "rings" were observed even in the absence of F-actin (Figure 2i,j). Previous studies proposed that INF2's FH2 domain was capable of dissociation [46]. Our AFM images provide structural evidence and confirm the ability of INF2-FFC to re-organize and assemble into oligomeric forms at higher protein densities.

Structure of free INF2-FF homodimers and oligomers

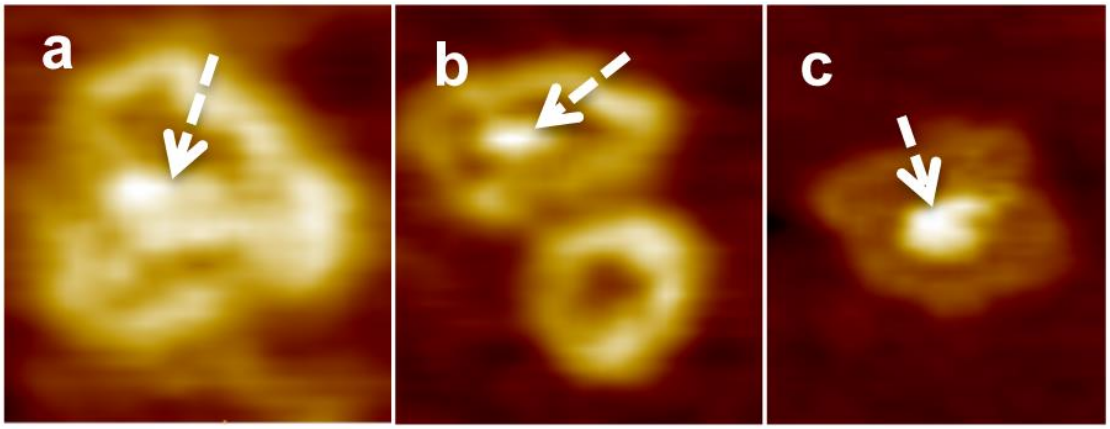

Figure 3. AFM images showing free INF2-FF self-organization configurations. The central core region observed as a dense mass (broken white arrows) within the oligomeric ring periphery in (a-c). The central dense core appears similar to that observed for INF2-FFC dimers and oligomers suggesting that it comes from the unstructured FH1 domain.

The effects on actin of the C-terminus from many formins have been investigated previously [52-54]. A region immediately C-terminal to the FH2 of the formin INF2 is known to strongly affect its activity on actin [39-40, 54]. To test the role of C-terminal region in INF2 self-assembly and oligomerization, we deleted it and probed the structure of free INF2-FF at 0.02 μM and 0.2 μM concentrations. Deletion of the C-terminal region did not inhibit the self-assembly of FH2 into dimers (at 0.02 μM) or oligomers (at 0.2 μM concentration). Figure 3 shows representative images of free INF2-FF self-organization configurations. The central core region observed as a dense mass (broken white arrows) within the oligomeric ring periphery in Figure 3a-c appears similar to that observed for INF2-FFC dimers and oligomers suggesting that it comes from the unstructured FH1 domain. The corresponding sizes for dimers and oligomers measured from AFM images were 22 ± 0.1 nm and 45 ± 2 nm for INF2-FFC and 22± 0.1 nm and 44 ± 1 nm for INF2-FF respectively (Table 1). Furthermore, the central dense region within the donut shaped structure seen in hollow dimer configurations (Figure 2c) presumably represents the flexible FH1 sequences lacking tertiary structure [46]. The fact that this central core is present in INF2-FF images (Figure 3) suggests that it is not the C-terminus.

Structure of F-actin-INF2-FH1-FH2-C (INF2-FFC) complexes

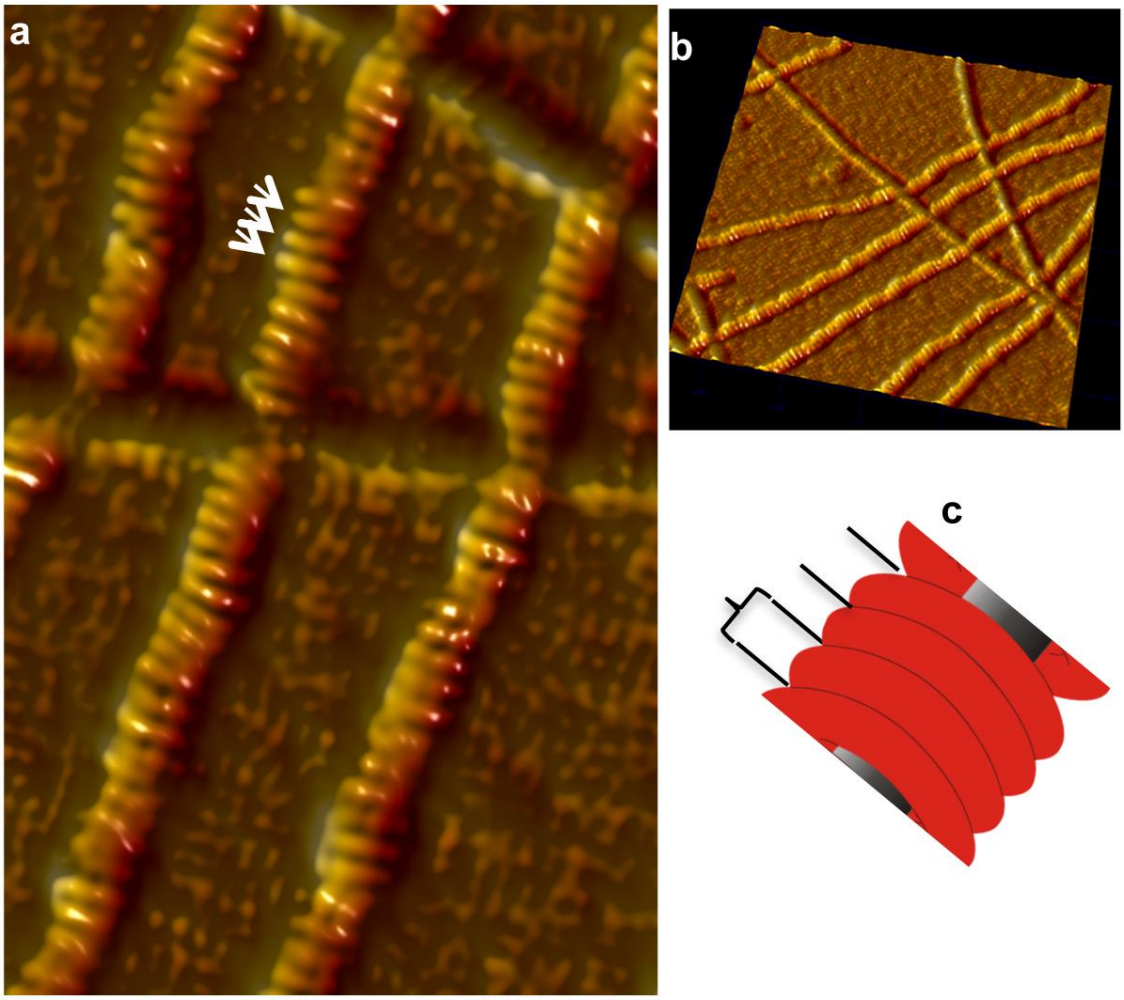

Figure 4. Structure of INF2-FFC and F-actin complexes. AFM image of INF2-FFC and F-actin complexes (at 1:1 mole ratio) revealing "ring-like" binding around actin filaments. (a) Zoomed in section of INF2-FFC-F-actin complex displaying detailed orientations of adjacent INF2-FFC homodimer rings assembled around F-actin. Notably, there is 5-10 degree occasional bending of adjacent units, indicating flexibility or strain across the bound complex. (b) 3D side view (500x 500 nm) showing stack like arrangement of INF2-FFC over F-actin. Tubular structure spacing is shown schematically in (c).

Recently, helical reconstruction of filaments from EM images [40] has revealed details on INF2-FFC bound F-actin architecture at 20 Å resolution, providing "average" structure for the entire F-actin filament population or sub-populations [55]. The previous successes of tapping mode AFM imaging in unraveling structure and mechanics of F-actin-ABP (Actin Binding Protein) complexes [32, 56], prompted us to apply this technique to seek single filament level structure of INF2-FFC and F-actin assembly at the nanoscale level. Figure 4 shows typical AFM tapping mode image of 1:1 ratio of INF2-FFC and F-actin complexes revealing "ring-like" arrangement of formin FH2 homodimers encircled around actin filaments (Figure 4a-b). INF2-FFC bound actin filaments show a mean width of ~30 nm and height of ~2.8 nm. Considering that bare F-actin in AFM images shows 1.8 nm tall and around 18.4 nm wide filaments, there is an estimated 1 nm increase in height and ~10 nm increase in the width of the filaments upon binding with INF2-FFC.

Structure of F-actin-INF2-FH1-FH2 (INF2-FF) complexes

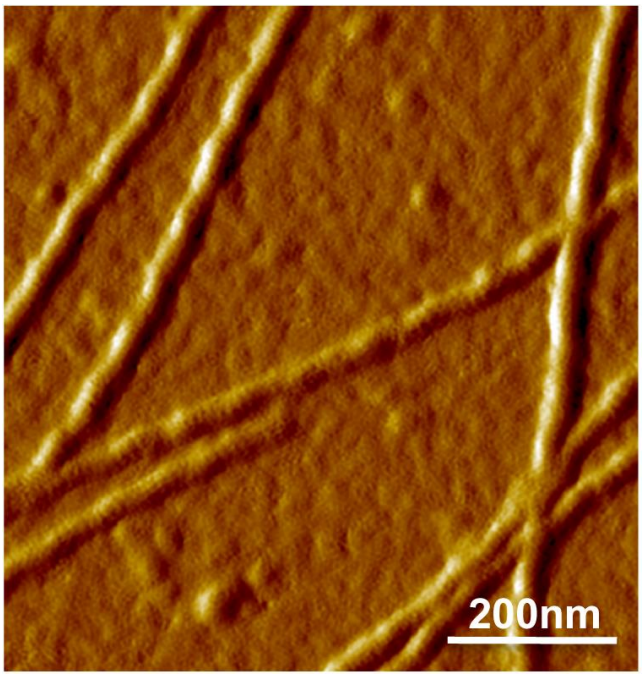

Figure 5. Structure of INF2-FF and F-actin complexes. AFM image of 1:1 ratio of INF2-FF and F-actin complexes revealing ring-like binding around actin filaments similar to INF2-FFC and F-actin complexes.

Further structural details illustrated in zoom-in section of INF2-FFC-F-actin complexes (Figure 4c) show INF2-FFC dimers to be 5.8 to 7 nm tall rings (See Figure 4a, white arrows)**,** with about 4 to 5 dimeric "rings" bound per helical F-actin twist. The INF2-FFC rings bind along the actin filament length (as marked in Figure 4c). Frequently, 5-10 degree deviations in binding orientations of adjacent homodimers were also observed, suggesting a level of flexibility of the dimers, or strain developed along F-actin upon INF2-FFC binding. Since EM images provide averaged structures of the F-actin-INF2 complexes, such details on individual filament level and deviations in binding orientations could not be observed previously [40]. Similar assembly of INF-FF was also observed in complex with F-actin. Figure 5 represents a typical AFM image obtained for INF2-FF and F-actin complexes revealing ring-like binding around actin filaments. The unique INF2-FFC and F-actin assembly reported here represents, to the best of our knowledge, the first three-dimensional AFM nanoscale structure obtained for any formin-F-actin complexes.

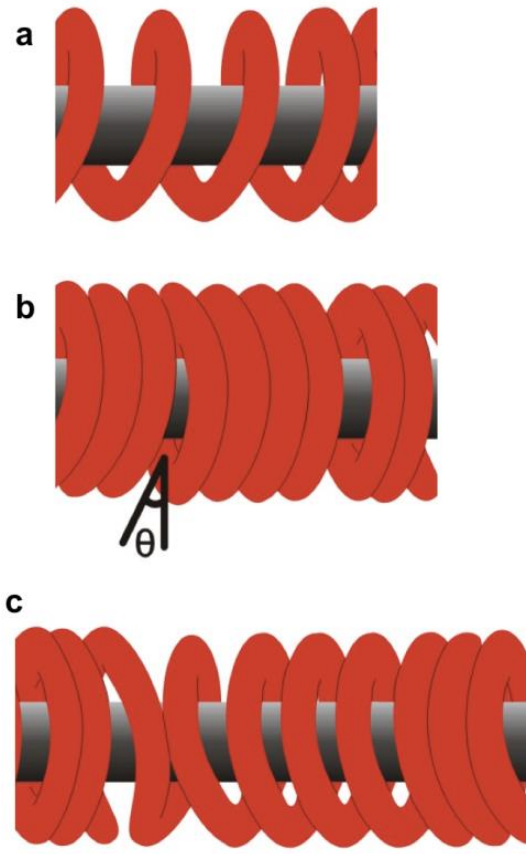

Figure 6. Schematic representation of plausible orientations of INF2-FFC homodimers over F-actin. (a) Adjacent INF2-FFC dimeric rings interact end-to-end to form spiral coil structure (b) Neighboring homodimers make longitudinal contact with adjacent F-actin bound dimers to form continuous structure without any gaps or with small angle gaps/openings (c) Combinations of regions as in (a) and (b), along the length of F-actin. Alternately, dimers may re-associate to form individual dimer rings stacked along the length of the filament with or without gap openings.

In summary, we have presented structural evidence confirming the ability of INF2-FFC to re-organize and assemble into oligomeric forms at higher protein concentrations, unrelated to its C-terminus region. Within the cellular context, higher-order INF2-F-actin structures may enable diverse functional roles in specific cellular conditions. Transitions between different oligomeric states may also be important in cooperative binding properties. Based on the AFM structures obtained for F-actin-INF2-FFC complexes, it is likely that formin undergoes disassociation and re-association of the FH2 domains to allow its encircling of actin filaments (Figure 6). In addition, oligomerization may allow formins to generate higher-order structures that may provide greater stability, while the reduced surface area of the dimer in a complex can offer protection against severing by other actin binding proteins.

8.5 Conclusions

The self-assembly of a formin FH2 domain into oligomeric structures, has been clearly resolved using AFM imaging of INF2-FFC and F-actin complexes. In the presence of actin filaments, INF2 organizes along the filament helix and creates discontinuities that might favor severing. Our data reveals significant structural insights into the possible dissociation and re-association of INF2-FFC to yield circular binding over F-actin. From the nanotechnology perspective, engineering the self-assembly of nanostructures such as formin complexes (hollow formin nanotubes or formin nanotubes over actin core) is likely to provide new opportunities for novel molecular designs and programmed assembly for a variety of bio-nanotechnology applications.

8.6 Supplementary information

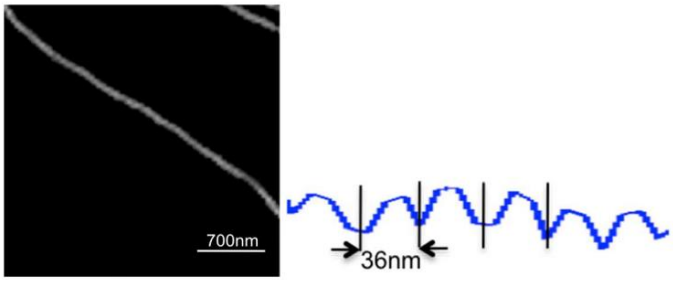

Figure S1. AFM topographic image of bare actin filament (left) and helical pitch (right).

Tip Convolution Effect [57-58]

Apparent width of the formin molecules increases in AFM images. Because an image obtained from AFM represents the convolution of the cantilever tip shape, which is a not infinitely sharp, lateral dimension of objects can be significantly exaggerated. Vertical distances can be precise to less than 0.5 nm, when measured as center-to-center distances of objects in close packed arrays. Thus, formin dimers imaged over mica surface that appear as ~30 nm in diameter may actually be several nanometers smaller. The apparent width measured (W) by tip of radius similar to the dimensions of the sample can be estimated as the distance between the 1st and last tip/sample contact. The smaller the tip (R_{tip}), the smaller the measured width.

When $R_{tip} \sim ¼\ R_{sample,}$ measured width = $2R_{sample}$

$$X^2 = (R_{tip} + R_{sample})^2 - (R_{tip} - R_{sample})^2$$

$$X = 2\sqrt{R_{tip}\ R_{sample}}$$

$$W = 2X = 4\sqrt{R_{tip}\ R_{sample}}$$

Thus, the observed dimensions for formin dimers are within the expected higher range limits for a 10 nm feature (~ formin molecule), imaged with a nominal tip size of 5-7 nm.

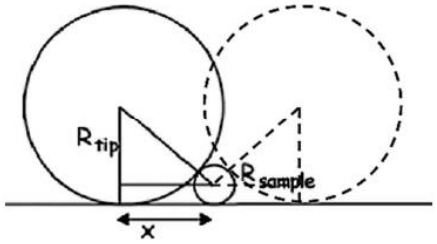

Figure S2. Schematic of the tip convolution effect

8.7 References

1. Whitesides, G.M. and B. Grzybowski, *Self-assembly at all scales.* Science, 2002. **295**(5564): p. 2418-21.
2. Kueh, H.Y. and T.J. Mitchison, *Structural Plasticity in Actin and Tubulin Polymer Dynamics.* Science, 2009. **325**(5943): p. 960-963.
3. Adamcik, J., et al., *Measurement of intrinsic properties of amyloid fibrils by the peak force QNM method.* Nanoscale, 2012. **4**(15): p. 4426-9.
4. Jang, H., et al., *Disordered amyloidogenic peptides may insert into the membrane and assemble into common cyclic structural motifs.* Chem Soc Rev, 2014.
5. Kornberg, R.D., *Chromatin Structure - Repeating Unit of Histones and DNA.* Science, 1974. **184**(4139): p. 868-871.
6. Spector, M.S., et al., *Chiral self-assembly of nanotubules and ribbons from phospholipid mixtures.* Nano Letters, 2001. **1**(7): p. 375-378.
7. Grenklo, S., et al., *Tropomyosin assembly intermediates in the control of microfilament system turnover.* Eur J Cell Biol, 2008. **87**(11): p. 905-20.
8. Peitsch, W.K., et al., *Drebrin particles: components in the ensemble of proteins regulating actin dynamics of lamellipodia and filopodia.* Eur J Cell Biol, 2001. **80**(9): p. 567-79.
9. Peitsch, W.K., et al., *Cell biological and biochemical characterization of drebrin complexes in mesangial cells and podocytes of renal glomeruli.* J Am Soc Nephrol, 2003. **14**(6): p. 1452-63.
10. Kuhn, J.R. and T.D. Pollard, *Real-time measurements of actin filament polymerization by total internal reflection fluorescence microscopy.* Biophys J, 2005. **88**(2): p. 1387-402.

11. Kuhn, J.R. and T.D. Pollard, *Single molecule kinetic analysis of actin filament capping. Polyphosphoinositides do not dissociate capping proteins.* J Biol Chem, 2007. **282**(38): p. 28014-24.

12. Breitsprecher, D., et al., *Rocket launcher mechanism of collaborative actin assembly defined by single-molecule imaging.* Science, 2012. **336**(6085): p. 1164-8.

13. Kovar, D.R. and T.D. Pollard, *Insertional assembly of actin filament barbed ends in association with formins produces piconewton forces.* Proc Natl Acad Sci U S A, 2004. **101**(41): p. 14725-30.

14. Li, X., et al., *Electron counting and beam-induced motion correction enable near-atomic-resolution single-particle cryo-EM.* Nat Methods, 2013. **10**(6): p. 584-90.

15. Spahn, C.M. and P.A. Penczek, *Exploring conformational modes of macromolecular assemblies by multiparticle cryo-EM.* Curr Opin Struct Biol, 2009. **19**(5): p. 623-31.

16. Binnig, G., C.F. Quate, and C. Gerber, *Atomic force microscope.* Phys Rev Lett, 1986. **56**(9): p. 930-933.

17. Radmacher, M., et al., *From molecules to cells: imaging soft samples with the atomic force microscope.* Science, 1992. **257**(5078): p. 1900-5.

18. Bustamante, C., et al., *Circular DNA molecules imaged in air by scanning force microscopy.* Biochemistry, 1992. **31**(1): p. 22-6.

19. Hansma, H.G. and J.H. Hoh, *Biomolecular imaging with the atomic force microscope.* Annu Rev Biophys Biomol Struct, 1994. **23**: p. 115-39.

20. Muller, D.J., et al., *Imaging purple membranes in aqueous solutions at sub-nanometer resolution by atomic force microscopy.* Biophys J, 1995. **68**(5): p. 1681-6.

21. Mueller, D.J. and Y.F. Dufrene, *Atomic force microscopy as a multifunctional molecular toolbox in nanobiotechnology.* Nature Nanotechnology, 2008. **3**(5): p. 261-269.

22. Sharma, S. and G. J.K, *Atomic Force Microscopy for Medicine*, in *Life at the nanoscale: Atomic Force Microscopy of live cells*, Y. Dufrene, Editor. 2011, Pan Stanford Publishing. p. 421-436.

23. Sharma, S., et al., *Quantitative nanostructural and single-molecule force spectroscopy biomolecular analysis of human-saliva-derived exosomes.* Langmuir, 2011. **27**(23): p. 14394-400.

24. Fotiadis, D., et al., *Structural characterization of two aquaporins isolated from native spinach leaf plasma membranes.* Journal of Biological Chemistry, 2001. **276**(3): p. 1707-1714.

25. Schabert, F.A., C. Henn, and A. Engel, *NATIVE ESCHERICHIA-COLI OMPF PORIN SURFACES PROBED BY ATOMIC-FORCE MICROSCOPY.* Science, 1995. **268**(5207): p. 92-94.

26. Scheuring, S., et al., *High resolution AFM topographs of the Escherichia coli water channel aquaporin Z.* Embo Journal, 1999. **18**(18): p. 4981-4987.

27. Kuznetsov, Y., P.D. Gershon, and A. McPherson, *Atomic force microscopy investigation of vaccinia virus structure.* J Virol, 2008. **82**(15): p. 7551-66.

28. Kuznetsov, Y.G., et al., *Atomic force microscopy investigation of human immunodeficiency virus (HIV) and HIV-Infected lymphocytes.* Journal of Virology, 2003. **77**(22): p. 11896-11909.

29. Ikai, A., et al., *ATOMIC-FORCE MICROSCOPY OF BACTERIOPHAGE-T4 AND ITS TUBE-BASEPLATE COMPLEX.* Febs Letters, 1993. **326**(1-3): p. 39-41.

30. McPherson, A. and Y.G. Kuznetsov, *Atomic Force Microscopy Investigation of Viruses*, in *Atomic Force Microscopy in Biomedical Research: Methods and Protocols*, P.C.R.D. Braga, Editor. 2011. p. 171-195.

31. Shao, Z.F., D. Shi, and A.V. Somlyo, *Cryoatomic force microscopy of filamentous actin.* Biophysical Journal, 2000. **78**(2): p. 950-958.

32. Sharma, S., et al., *Atomic force microscopy reveals drebrin induced remodeling of f-actin with subnanometer resolution.* Nano Lett, 2011. **11**(2): p. 825-7.

33. Campellone, K.G. and M.D. Welch, *A nucleator arms race: cellular control of actin assembly.* Nat Rev Mol Cell Biol, 2010. **11**(4): p. 237-51.

34. Chesarone, M.A., A.G. DuPage, and B.L. Goode, *Unleashing formins to remodel the actin and microtubule cytoskeletons.* Nat Rev Mol Cell Biol, 2010. **11**(1): p. 62-74.

35. DeWard, A.D., et al., *The role of formins in human disease.* Biochim Biophys Acta, 2010. **1803**(2): p. 226-33.

36. Otomo, T., et al., *Structural basis of actin filament nucleation and processive capping by a formin homology 2 domain.* Nature, 2005. **433**(7025): p. 488-94.

37. Higgs, H.N., *Formin proteins: a domain-based approach.* Trends Biochem Sci, 2005. **30**(6): p. 342-53.

38. Goode, B.L. and M.J. Eck, *Mechanism and function of formins in the control of actin assembly.* Annu Rev Biochem, 2007. **76**: p. 593-627.

39. Chhabra, E.S. and H.N. Higgs, *INF2 Is a WASP homology 2 motif-containing formin that severs actin filaments and accelerates both polymerization and depolymerization.* J Biol Chem, 2006. **281**(36): p. 26754-67.

40. Gurel, P.S., et al., *INF2-Mediated Severing through Actin Filament Encirclement and Disruption.* Curr Biol, 2014.

41. Xu, Y., et al., *Crystal structures of a Formin Homology-2 domain reveal a tethered dimer architecture.* Cell, 2004. **116**(5): p. 711-23.

42. Thompson, M.E., et al., *FMNL3 FH2-actin structure gives insight into formin-mediated actin nucleation and elongation.* Nat Struct Mol Biol, 2013. **20**(1): p. 111-8.

43. Yamashita, M., et al., *Crystal structure of human DAAM1 formin homology 2 domain.* Genes Cells, 2007. **12**(11): p. 1255-65.

44. Moseley, J.B., et al., *A conserved mechanism for Bni1- and mDia1-induced actin assembly and dual regulation of Bni1 by Bud6 and profilin.* Mol Biol Cell, 2004. **15**(2): p. 896-907.

45. Harris, E.S. and H.N. Higgs, *Biochemical analysis of mammalian formin effects on actin dynamics.* Methods Enzymol, 2006. **406**: p. 190-214.

46. Paul, A.S. and T.D. Pollard, *Review of the mechanism of processive actin filament elongation by formins.* Cell Motil Cytoskeleton, 2009. **66**(8): p. 606-17.

47. Spudich, J.A. and S. Watt, *The regulation of rabbit skeletal muscle contraction. I. Biochemical studies of the interaction of the tropomyosin-troponin complex with actin and the proteolytic fragments of myosin.* J Biol Chem, 1971. **246**(15): p. 4866-71.

48. Harris, E.S., F. Li, and H.N. Higgs, *The mouse formin, FRLalpha, slows actin filament barbed end elongation, competes with capping protein, accelerates polymerization from monomers, and severs filaments.* J Biol Chem, 2004. **279**(19): p. 20076-87.

49. Li, F. and H.N. Higgs, *Dissecting requirements for auto-inhibition of actin nucleation by the formin, mDia1.* J Biol Chem, 2005. **280**(8): p. 6986-92.

50. Lu, J., et al., *Structure of the FH2 domain of Daam1: implications for formin regulation of actin assembly.* J Mol Biol, 2007. **369**(5): p. 1258-69.

51. Maiti, S., et al., *Structure and activity of full-length formin mDia1.* Cytoskeleton (Hoboken), 2012. **69**(6): p. 393-405.

52. Gould, C.J., et al., *The formin DAD domain plays dual roles in autoinhibition and actin nucleation.* Curr Biol, 2011. **21**(5): p. 384-90.

53. Heimsath, E.G., Jr. and H.N. Higgs, *The C terminus of formin FMNL3 accelerates actin polymerization and contains a WH2 domain-like sequence that binds both monomers and filament barbed ends.* J Biol Chem, 2012. **287**(5): p. 3087-98.

54. Ramabhadran, V., P.S. Gurel, and H.N. Higgs, *Mutations to the formin homology 2 domain of INF2 protein have unexpected effects on actin polymerization and severing.* J Biol Chem, 2012. **287**(41): p. 34234-45.

55. Sharma, S., et al., *Correlative nanoscale imaging of actin filaments and their complexes.* Nanoscale, 2013.

56. Sharma, S., et al., *Molecular cooperativity of drebrin(1-300) binding and structural remodeling of f-actin.* Biophys J, 2012. **103**(2): p. 275-83.

57. Grutter, P., W. Zimmermannedling, and D. Brodbeck, *Tip Artifacts of Microfabricated Force Sensors for Atomic Force Microscopy.* Applied Physics Letters, 1992. **60**(22): p. 2741-2743.

58. Villarrubia, J.S., *Morphological Estimation of Tip Geometry for Scanned Probe Microscopy.* Surface Science, 1994. **321**(3): p. 287-300.